

Broadband Radio Frequency Transmitter for Magnetic Resonance Imaging

by

Hai Lu

A dissertation submitted to the Graduate Faculty of
Auburn University
in partial fulfillment of the
requirements for the Degree of
Doctor of Philosophy

Auburn, Alabama
August 1, 2015

Keyword: MRI RF Coil, RF Front-end Circuits, Parallel Plate Waveguide,
Volume Transmission, Receive-only Array

Copyright 2015 by Hai Lu

Approved by

Shuming Wang, Chair, Associate Professor of Electrical and Computer Engineering
Michael Baginski, Associate Professor of Electrical and Computer Engineering
Lloyd Stephen Riggs, Professor of Electrical and Computer Engineering
Fa Foster Dai, Professor of Electrical and Computer Engineering

Abstract

In Magnetic Resonance Imaging (MRI) application, radio frequency (RF) coils play an important role to excite the nuclei inside the imaging subject and receive MR generated signals. To achieve optimal transmit efficiency/receive sensitivity, it is necessary to re-tune the RF coils to its resonant frequency for different scanning samples. And the re-tune procedure is time-consuming. In this study, we proposed a novel RF volume transmission method which takes advantage of parallel plate waveguide (PPW). Due to the frequency-independent nature of the PPW, the designed volume transmit coils are able to work in broadband and are insensitive the loading changes so that the tedious re-tune procedure for different loadings can be avoided. In order to interface the PPW coils with the scanner, RF front-end circuits at both transmit end and receive end are designed, optimized and fabricated as discussed in Chapter 2. In Chapter 3, a linear PPW coil is designed and fabricated for human forearm proton imaging and phosphorous spectroscopy analysis. The calibrated transmit efficiency of PPW coil measured is close to that of the un-shielded Birdcage coil with same coil dimensions. Both high SNR proton images and decent phosphorous signals are obtained from both buffer solution phantom and human forearm. In Chapter 4, to meet with requirements of large volume transmission for MRI, a quadrature PPW coil's design, fabrication and testing procedure is discussed. The transmit efficiencies of linear excitation and quadrature excitation are measured and compared. An approximate 40% increase in transmit efficiency is achieved

by using quadrature excitation. To boost the local SNR of the images, a conformal four-channel “clover” shape detonable receive-only array is designed for MR signal reception. Both overlap and capacitive decoupling methods are employed to eliminate the mutual coupling between neighboring coils. The obtained uncombined images are compared with simulated receive coil profile to demonstrate the effectiveness of the decoupling strategies employed.

Acknowledgments

I would like to thank my advisor Dr. Shumin Wang for his great help and inspiration over the past four years of this project. It was he who helped me overcome several obstacles during the research process. Also, I would like to thank my committee members Dr. Baginski, Dr. Riggs and Dr. Dai for their help on the theoretical problem description and experimental evidence. I would like thank my parents for their great support during my whole life.

Table of Contents

Abstract	ii
Acknowledgments.....	iv
List of Figures	vii
List of Tables	xiv
List of Abbreviations	xv
1. Introduction.....	1
1.1. MRI Basics.....	1
1.2. Radio Frequency (RF) Coils for MRI.....	2
1.2.1. Volume Coil	2
1.2.2. Surface Coil.....	5
1.2.3. Phased Array	7
1.2.4. Receive-only Array	8
1.2.5. Transmit-receive Coil.....	14
2. Radio Frequency Front-End Circuits Design	17
2.1. Wilkinson Power Divider.....	18
2.1.1. Unequal Power Ratio Wilkinson Power Divider	18
2.1.2. Broadband Wilkinson Power Divider.....	27
2.2. T/R Switch.....	33
2.3. Diplexer	37
2.4. Low Noise Preamplifier	41
3. Parallel-Plate Waveguide for Volume Radio Frequency Transmission in MRI.....	52
3.1. Introduction	52
3.2. Broadband Volume Transmitter Design.....	54
3.3. Numerical Simulation.....	57
3.4. Transmit Coil Fabrication.....	62

3.4.1	Tranmsit Coil Matching	62
3.4.2	Front-end Circuits	67
3.4.3	Power Re-entrant.....	68
3.4.4	Transmit Coil Bench-testing.....	69
3.4.5	Receiver Design	76
3.5	MRI Measurements	77
3.5.1	¹ H Images and ³¹ P Spectroscopy.....	77
3.5.2	Transmit Efficiency Comparison with Birdcage Coil.....	81
3.6	Conclusion.....	83
4.	Quadrature Parallel-Plate Waveguide for Larger Volume Transmission in MRI ...	84
4.1	Introduction	84
4.2	Numerical Simulation.....	85
4.3	Transmit Coil Fabrication.....	92
4.4	Bench-testing.....	95
4.5	Receive-only Array Design	102
4.5.1	Numerical Simulations	103
4.5.2	Q-factor Measurement.....	108
4.5.3	Detune Circuit	109
4.5.4	Common Mode Current Suppression	113
4.6	System Interface	114
4.7	MRI Measurements	116
4.7.1	Transmit Efficiency Improvement using Quadrature Structure	116
4.7.2	¹ H Images	119
4.8	Conclusion.....	122
5.	Future recommendations.....	123
	Bibliography	124

List of Figures

1.1	High-pass Birdcage coil and its lumped element equivalent circuit.....	4
1.2	a). Model of un-shielded high-pass Birdcage coil designed at 123.2MHz b). Frequency response of the Birdcage coil c). Simulated B_1^- field in transverse plane d). Simulated B_1^+ field in transverse plane	5
1.3	a). A four-channel receiver array b-e). Uncombined images of the four coil elements in transverse plane f). Combined image in transverse plane	9
1.4	When two adjacent surface coils tuned to the same frequency f_0 , the original resonances split into two resonances.	10
1.5	Schematic of the preamplifier decoupling for the surface coil matched using L-network.	12
1.6	Double-probe and single probe fabricated using semi-rigid coaxial cable. The screw can be twisted and change the overlap area of the double probe precisely to obtain optimal decoupling.	13
1.7	Measured probe gain of isolated coil and preamplifier decoupled coil.	14
1.8	Diagram of a typical transmit and receive coil.	15
1.9	Design example of a four-channel cardiac transmit/receive array. a). Front-end circuit board b). Transmit/receive array c). Phantom image in transverse plane d). Human cardiac image	16
2.1	A Wilkinson power divider in microstrip form having unequal power division ...	19
2.2	Schematic of unequal Wilkinson power divider with additional transmission lines for impedance matching.....	21
2.3	Layout of the unequal Wilkinson power divider used in ADS Momentum simulation.....	23
2.4	Simulation results for 1:5 unequal Wilkinson power divider at 297.2MHz.	24
2.5	Simulation results for 1:2 unequal Wilkinson power divider at 120.3MHz.	24

2.6	Measured S-parameters of the fabricated 1:5 unequal Wilkinson power divider at 297.2MHz. a). Mag(S21) b). Phase(S21) c). Mag(S31) d). Phase(S31) e). Mag(S11).....	25
2.7	Measured S-parameters of the fabricated 1:2 unequal Wilkinson power divider at 120.3MHz. a). Mag(S21) b). Phase(S21)) c). Mag(S31) d). Phase(S31) e). Mag(S11)	26
2.8	Schematic representation of a two-section transformer	27
2.9	Control panel of the ADS circuit performance optimization. For the broadband Wilkinson power divider, the magnitude of the reflection coefficient was optimized over a wide frequency band.....	30
2.10	Layout of the broadband Wilkinson power divider used in ADS Momentum simulation.	30
2.11	Simulation results for broadband Wilkinson power divider from DC to 400MHz.	31
2.12	Measured S-parameters of the fabricated broadband Wilkinson power divider at both 123.2MHz and 297.2MHz. a). Mag(S21) b). Phase(S21) c). Mag(S31) d). Phase(S31) e). Mag(S11)	32
2.13	Schematic of the Transmit/Receive switch.	33
2.14	Measurement results for 297.2MHz T/R switch. a). Insertion loss of receive channel b). Isolation of receive channel c). Insertion loss of transmit channel d). Isolation of transmit channel	35
2.15	Measurement results for 120.3MHz T/R switch. a). Insertion loss of receive channel b). Isolation of receive channel c). Insertion loss of transmit channel d). Isolation of transmit channel	36
2.16	a) Schematic of the band-stop filter at 297.2MHz. b) Simulated transmission (in Blue) and return (in Red) loss of the band-stop filter.....	37
2.17	a) Schematic of the band-stop filter at 120.3MHz. b) Simulated transmission (in Blue) and return (in Red) loss of the band-stop filter.....	38
2.18	Layout of the diplexer used in ADS Momentum simulation	39
2.19	Simulation results for diplexer from 50MHz to 350MHz.	39
2.20	Measurement results for diplexer a). High frequency channel b). Low frequency channel.....	40

2.21	Block diagram of a two-stage LNA designed for MRI application	41
2.22	Schematic of the high input impedance preamplifier.....	42
2.23	Simulated stability factor of ATF54143 with attenuators added at c).123.3 MHz and d). 297.2 MHz.....	43
2.24	Constant gain circles of ATF54143 with attenuator at both 120.3MHz and 297.2MHz.....	45
2.25	Illustration of input and output matching networks for first stage of the high input impedance preamplifier	46
2.26	Simulation schematic of the first stage of the preamplifier.....	47
2.27	Simulation results of the first stage of the preamplifier at 120.3MHz	48
2.28	Simulation results of the first stage of the preamplifier at 297.2MHz	48
2.29	Simulation layout of the high input impedance preamplifier in ADS Momentum simulation	49
2.30	Simulation results of the two-stage high input impedance preamplifier at 120.3MHz.....	50
2.31	Simulation results of the two-stage high input impedance preamplifier at 297.2MHz.....	50
2.32	Measured input impedance of the preamplifier fabricated at a). 120.3MHz b). 297.2MHz. and measured gain and noise figure at a). 120.3MHz b). 297.2MHz ..	51
3.1	Electromagnetic field distribution of the TEM mode of a parallel-plate waveguide.	56
3.2	Simulation model for linear parallel plate coil.	57
3.3	The optimization results of reflection coefficient versus the input impedance for the PPW coil with and without phantom loading.	58
3.4	Simulated reflection coefficient of the PPW coil over the frequency band from 50MHz to 350MHz.	59
3.5	Simulated current distribution on the PPW coil at 120.3MHz and 297.2 MHz.....	60

3.6	Simulated electromagnetic field of the PPW coil in sagittal plane at 120.3MHz and 297.2MHz.	61
3.7	Prototype parallel-plate waveguide. The balanced Chebyshev impedance matching circuits are mounted across the gaps.	62
3.8	Simulation schematic and result of the broadband matching network with Chebyshev frequency response.	63
3.9	Schematic of the balanced broadband matching network and measured reflection coefficient at 120.3MHz and 297.2MHz.....	64
3.10	Schematic representation of the reflection and insertion loss measurement of the PPW coil. When the reflection coefficient was measured, port 2 was terminated with 50 ohm and port was connected to network analyzer.	65
3.11	Measured reflection coefficient of the PPW coil with broadband matching networks and Wilkinson power divider/combiner connected.	66
3.12	Measured insertion loss of the PPW coil with broadband matching networks and Wilkinson power divider/combiner connected.	66
3.13	Schematic of the front-end circuits of the linear PPW coil.....	67
3.14	Bench-testing setting-up for the re-entrant power phase compensation and total insertion loss measurement for 1H transmit channel	70
3.15	Measured phase delay of the re-entrant power path and total insertion loss which includes PPW coil and front-end circuits of 1H transmit channel	71
3.16	Bench-testing setting-up for the re-entrant power phase compensation and total insertion loss measurement for 31P transmit channel.....	72
3.17	Measured phase delay of the re-entrant power path and total insertion loss which includes PPW coil and front-end circuits of 31P transmit channel.....	72
3.18	a) Bench-testing setting-up for the transmit field homogeneity verification for 1H transmit channel. b) Signal detected by single probe.	74
3.19	a) Bench-testing setting-up for the transmit field homogeneity verification for 31P transmit channel. b) Signal detected by single probe.	75
3.20	PPW coil connected with front-end circuit board for imaging experiments.....	77
3.21	a). Measured B_1^+ map and b). TSE image of the phantom in transverse plane	78

3.22	Scanning experiments setting-up for human forearm imaging	78
3.23	TSE (a, c) and GRE (b, d) images of the forearm measured at 7T	79
3.24	P31 spectroscopy obtained using CSI sequence on a). Human forearm and b). phantom	80
3.25	Directly measured (a) and calibrated (b) transmit efficiency of the PPW and birdcage coil loaded with the saline water phantom	82
4.1	Illustration of the H-field generated within the quadrature PPW coils.....	86
4.2	Front view of Quadrature PPW coils models a) without cutouts, b) with cutouts ..	87
4.3	The comparison of imaginary part of the input impedance of inner coil (without loading) between three circumstances a). single inner coil, b) inner and outer coils with no decoupling strategies, c) inner and outer coils with decoupling strategies	87
4.4	Current distribution on single inner PPW coil a). without outer PPW coil. b). current distribution on inner PPW coil with outer PPW coil terminated with load impedance.....	89
4.5	The optimization results of reflection coefficient versus the load impedance for the PPW coils.	90
4.6	B_1^+ field distributions of the quadrature PPW coils in a) Transverse plane. b) Sagittal plane. c) Coronal plane.	91
4.7	Schematic of the Chebyshev matching network of (a) the outer PPW coil and (b) the inner PPW coil. Reflection coefficient measured for (c) outer PPW coil's matching network and (d) inner PPW coil's matching network	93
4.8	Bench-testing setting-up for the reflection coefficient measurement for both inner and outer PPW coils	95
4.9	Bench measured reflection coefficient of inner PPW coil (a) without phantom and (b) with phantom. Bench measured reflection coefficient of outer PPW coil (c) without phantom and (d) with phantom.	96
4.10	Bench-testing setting-up for the phase delay measurement of the PPW coils	97
4.11	Bench measured phase delay of the power re-entrant path of the inner PPW coil ..	97
4.12	Bench measured phase delay of the power re-entrant path of the outer PPW coil	98

4.13	Bench measurement of the transmit efficiency of inner PPW coil at the coil center a) Measurement setting-up b) Signal level detected	100
4.14	Bench measurement of the transmit efficiency of outer PPW coil at the coil center a) Measurement setting-up b) Signal level detected	101
4.15	Schematic of the receive element in the 4-ch receive array	103
4.16	Top and front views of the model of the receiver array positioned in the quadrature PPW coils	104
4.17	Current distributions on all receive elements with four elements excited separately.	106
4.18	Receiving coil profile simulation model (The outer PPW coils is hidden to show the receive array) and simulated profile of four receive elements in sagittal plane	107
4.19	Measured unloaded Q and loaded Q of single isolated receive coil	109
4.20	Bench measurement setting-up for the detune circuit using decoupled double probe	110
4.21	Measured frequency response of single receive element with and without detuning circuit.....	111
4.22	Four-channel receive array positioned in the matched quadrature PPW coils.....	112
4.23	Schematic representation of the four-channel receive array connected with system through interface.....	115
4.24	Schematic representation of the quadrature PPW coils connected with system through interface.....	115
4.25	Scanning experiments setting-up for transmit efficient measurement on head phantom	117
4.26	Normalized signal intensity versus transmit voltage for linear and quadrature structure	117
4.27	GRE images of head phantom in sagittal plane using a) Linear excitation. b) Quadrature excitation	118
4.28	Uncombined images of the four-channel receive array obtained using GRE sequence	119

4.29	Scanning experiments setting-up for human leg imaging	120
4.30	The spin echo images of the calf muscle. a).Coronal plane b). Sagittal plane and c). Transversal plane.	121

List of Tables

2.1	Theoretically calculated values for isolation resistors and characteristic impedances of transmission lines for unequal Wilkinson power divider	22
2.2	Simulated transistor parameters with attenuator attached	44
2.3	Parameters of the designed first stage of the preamplifier.....	47
4.1	Measured S-parameter matrix of the four-channel receive array	112

List of Abbreviations

MRI	Magnetic Resonance Imaging
RF	Radio Frequency
PPW	Parallel Plate Waveguide
FID	Free Induction Decay
CSI	Chemical Shift Imaging
LNA	Low Noise Amplifier
SNR	Signal to Noise Ratio
PIN	Positive Intrinsic Negative

1. Introduction

1.1. MRI Basics

The principles of MRI rely on the spinning motion of specific nuclei present in biological tissues. Nuclei with odd atomic weight and/or an odd atomic number that have a net spin or angular momentum are tend to align their axis of rotation to an applied magnetic field and acquire a magnetic moment. The proton, the nucleus of the hydrogen atom, is the most prominent nucleus used for MR imaging due to its abundance in human body and nonzero nuclear magnetic moment.

In the absence of an applied magnetic field, the magnetic moments of the hydrogen nuclei are randomly distributed and the net magnetization equals to zero [2]. When a strong static external magnetic field B_0 is applied to the sample, the hydrogen nuclei will align with or against this magnetic field and create a net magnetization in the direction of the main magnetic field. Each nucleus that makes up the net magnetization vector is spinning about its own axis while the influence of B_0 field makes magnetic moments of hydrogen precess around B_0 . The precessional frequency is defined by Larmor equation

$$\omega_0 = B_0 \times \lambda \quad (1.1)$$

where B_0 is the magnetic field strength of the magnet, ω_0 is the precessional frequency and λ is the gyromagnetic ratio which represents the relationship between the angular momentum and the magnetic moment of each MR active nucleus.

According the definition of the resonance, nucleus can obtain energy form the external perturbation oscillates at the same precessional frequency. In order to make the

hydrogen nucleus resonate, an external radio frequency B_1 field at exact Larmor frequency of hydrogen needs to be applied. This B_1 tips the NMV from longitudinal plane toward transverse plane with an angle which is so-called flip angle. The magnitude of the flip angle depends on the amplitude and duration of the B_1 field.

When the tipped coherent magnetization cuts across a receiver loop, a voltage (MR signal) is induced and the strength of this MR signal depends on the amount of the magnetization in the transverse plane. After the switching-off of the B_1 field, the NMV returns to align with B_0 and loses energy. Two time constants T_1 and T_2 are used to define the relaxation. The longitudinal component experiences exponential recovery with time constant T_1 and the transverse component experiences exponential decay with time constant T_2 .

1.2. Radio Frequency (RF) Coils for MRI

RF coils usually functions as a transmitter to excite the nuclei inside the imaging subject, and as a receiver to collect MR signal induced by nuclei during the relaxation process [3]. For different structures, the RF coils can be divided into two major categories: volume coils and surface coils.

1.2.1. Volume Coil

Volume coils are designed to cover a bigger field of view such as human head, knee or even the whole body and provide homogeneous RF excitation. The most widely used volume coils clinically include Birdcage Coils, TEM Coils [5] and Saddle Coils [33]. The disadvantage of the volume coils is that large field of view makes them receive

noise from the whole sample and reduce the SNR. To address this problem, quadrature excitation is often employed in volume coil design to increase the SNR by a factor of $\sqrt{2}$ and reduce the power consumption to half [3].

Birdcage coil is the most common used volume coils for both RF excitation and MR signal reception. Since the Birdcage coil will be used in this dissertation for transmit efficiency comparison with the proposed novel volume transmission coil, the basic theory of the Birdcage coil is briefly reviewed in this section and an example of the Birdcage coil designed at 3T is given.

The birdcage coil is made of multiple parallel conductive segments that are parallel to the B_0 field (Fig 1.1). These parallel conductive segments are referred to as the rungs or the legs. These rungs interconnect a pair of conductive loop segments, and the two top and bottom loops are called the end rings. A high-pass coil is where the conductive loops have capacitors between adjacent rungs. A low-pass coil is where the capacitors are in the middle of the rungs. A hybrid coil is where the capacitors are located on the loop segments and the rungs. A high-pass is so called because the high frequency signals will tend to pass through capacitive elements while low frequency signals will tend to pass through inductive elements.

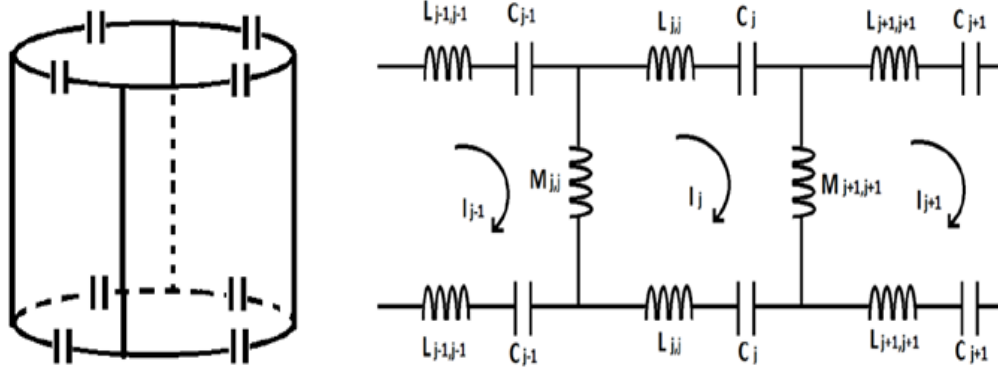


Figure 1.1: High-pass Birdcage coil and its lumped element equivalent circuit.

The current on each rung can be calculated using Equation (1.2) and the resonant frequencies can be derived from Equation (1.3) in which C is the capacitor value, L is the value of the inductance and M represents the mutual inductance.

$$\begin{aligned}
 (I_j)_m &= \cos \frac{2\pi m j}{N} \quad m = 0, 1, 2 \dots \frac{N}{2} \\
 &= \sin \frac{2\pi m j}{N} \quad m = 0, 1, 2 \dots \frac{N}{2} - 1
 \end{aligned} \tag{1.2}$$

$$\omega_m = [C(L + 2M \sin^2 \frac{\pi m}{N})]^{-\frac{1}{2}} \quad m = 0, 1, 2 \dots \frac{N}{2} \tag{1.3}$$

For high-pass birdcage coil $m = 1$ gives the dominant mode at the second highest resonant frequency. The currents in all rungs have an approximate sinusoidal current distribution so that a homogeneous field could be generated.

An 8-rung high-pass Birdcage coil design example is shown in Figure 1.2. The dominant mode of the Birdcage coil was tuned to 123.2MHz. The B_1^+ and B_1^- fields were simulated and shown in Figure 1.2 (c) and (d).

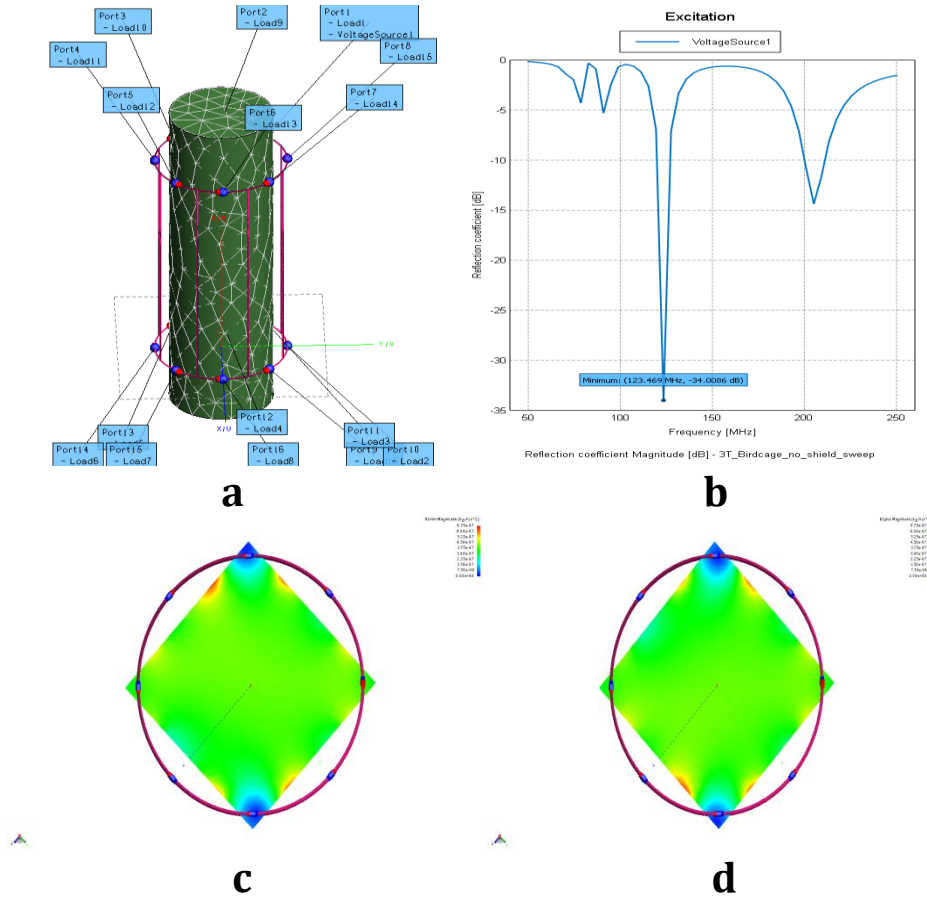


Figure 1.2: a) Model of un-shielded high-pass Birdcage coil designed at 123.2MHz b). Frequency response of the Birdcage coil c). Simulated B_1^- field in transverse plane d). Simulated B_1^+ field in transverse plane.

1.2.2. Surface Coil

Different from the volume coil which detects the signal from the whole sample, the surface coil placed close to the sample surface was firstly developed by Ackerman

and the improved SNR was demonstrated [34]. Due to the fact that the surface coil is positioned much closer to the imaging sample, the signal received is enhanced and meanwhile the noise is only picked up in the vicinity of the surface coil which leads to higher SNR than using volume coils. The SNR of a single surface loop can be derived by dividing the induced electromotive force (EMF) by the total noise of the loop coil. The EMF produced at the terminals of a coil is defined as Equation (1.4) according to the Faraday's Law

$$V_{signal} = - \int \frac{\partial}{\partial t} \{ \overline{B_1} \cdot \overline{M_0} \} dV_s = \frac{1}{\sqrt{2}} \omega_0 B_1 M_0 V_s \quad (1.4)$$

where B_1 represents the RF magnetic field. V_s is the voxel volume in which the fields of the coil and the magnet are assumed as constant. M_0 is the magnitude of the static equilibrium magnetization projected into the transverse plane. The noise of the coil within the signal receiving bandwidth Δf is characterized by the coil resistance R as

$$V_{noise} = \sqrt{4kT\Delta fR} \quad (1.5)$$

in which k is Boltzman's constant and T is the operating temperature. The intrinsic SNR can be derived as the ratio of the peak signal voltage to the rms noise level

$$SNR = \frac{1}{\sqrt{2}} \frac{\omega_0 B_1 M_0 V_s}{\sqrt{4kT\Delta fR}} \quad (1.6)$$

To realize most efficient power transmission and signal reception, the surface coil needs to be tuned exactly to its Larmor frequency. For regular loop coil, the inductance of each wire segment can be easily estimated according to the coil structure and the material

chosen for fabrication. Then the capacitors value can be obtained using Equation (1.7) to realize resonance.

$$C = \frac{1}{(2\pi f)^2 L} \quad (1.7)$$

The capacitors need to be distributed evenly along the loop. Following the rule of thumb, the individual segments of the coil conductor should be smaller than 1/10 of the wavelength to minimize the phase shifts along the coil path [1]. When the coil is connected to the network analyzer for the input impedance measurement, a real impedance should be observed at the input terminal of the loop coil which represents the total loss (coil loss, radiation loss and phantom loss) at the tuning frequency. After tuning the coil to the Larmor frequency, the input impedance of the coil needs to be matched to the system characteristic impedance (50 ohm) to prevent signal reflection. There are many matching network topologies can be employed such as pi-network, L-network and transformer matching. Most appropriate matching schemes should be determined based on different coil dimensions and its applications.

1.2.3. Phased Array

However, the relative small dimension of the surface coil extremely constraints its field coverage. To address this problem, loop array was proposed by Roemer to obtain optimal SNR over the entire volume region covered [26]. Other than improved SNR, phased array also brings in more design flexibility for MRI RF coil design. It could be used for receive-only array, transmit-receive array and parallel imaging.

1.2.4. Receive-only Array

As aforementioned single surface loop can provide a high relative SNR over only a small region, but if with proper image reconstruction techniques, the signal from the array could provide higher SNR over the entire field of interest. The signals from each of the receive element can be combined either by hardware combiner or weighting the signals from each coil for optimal SNR using algorithm. During the SNR optimization, the weighting coefficient includes amplitude and phase for each array element need to be corrected at each single point. There are several methods that could be used for combining the receive signals [26]. The easiest way is to reconstruct the images by directly combining the magnitudes. However, it will result in a lower image SNR than using complex images. Furthermore, optimum B_1 -weighted combining can be employed when B_1 fields generated by the coil elements are known. If the coils magnetic fields are un-known, the root-sum-of squares (RSS) can be used to combine the images and estimate SNR [66]. An example of four channel receive-only array combined images is shown in Figure 1.3.

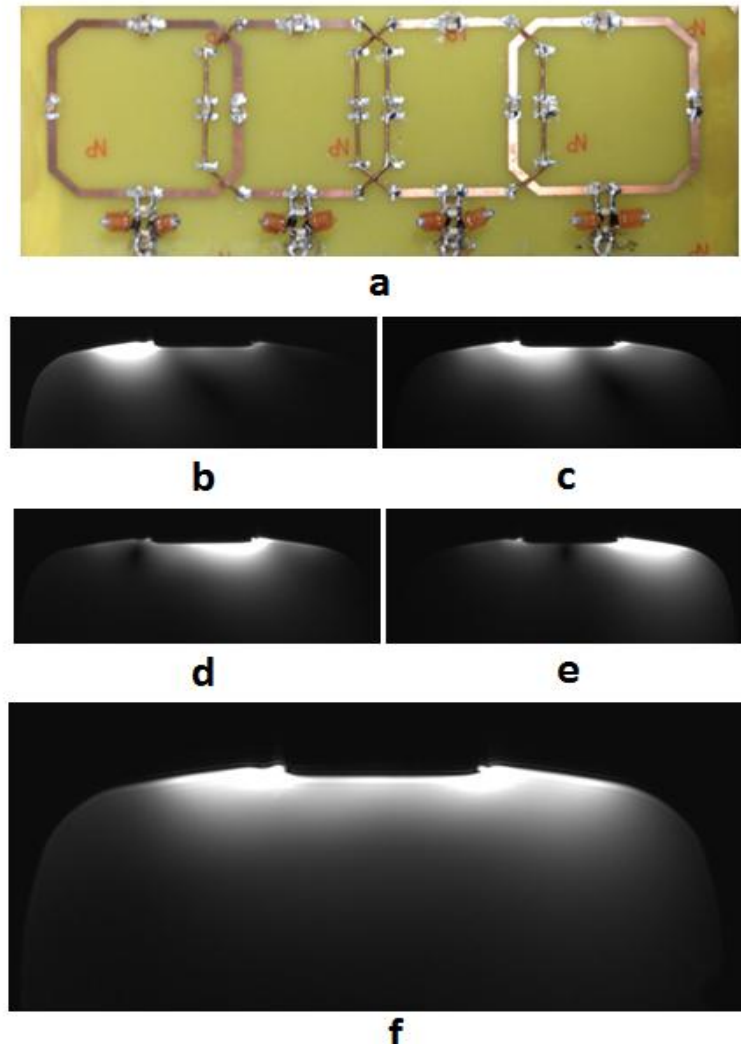


Figure 1.3: a) A four-channel receiver array b-e) Uncombined images of the four coil elements in transverse plane f) Combined image in transverse plane.

Due to this advantage, the receive-only array is widely used in clinical MR system incorporated with a separate transmit coil which provides homogeneous B1 field excitation. However, to obtain optimal SNR in the combined image, each array element needs to be working independently. Theoretically, when two array elements which are tuned to the same resonant frequency are placed in close proximity, the mutual coupling between the elements will split the resonances as shown in Figure 1.4. The mutual

inductance will transfer signal and noise within the coupling elements and then reduce the receive sensitivity [26].

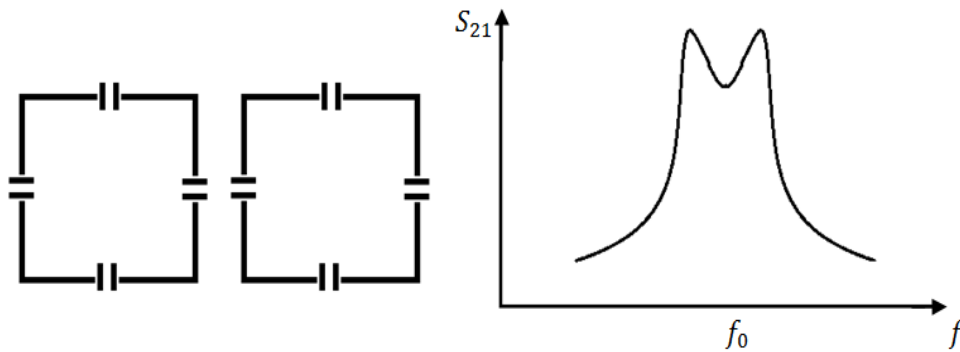


Figure 1.4: When two adjacent surface coils tuned to the same frequency f_0 , the original resonances split into two resonances.

There are several methods can be employed to eliminate the mutual decoupling between array elements. Firstly, by slightly overlapping two neighboring coils, the mutual inductance can be greatly reduced. When two adjacent coils are properly overlapped, the magnetic flux flow through the overlapped area cancels out the magnetic flux in un-overlapped area, so that the inductive coupling can be well-reduced in a wide frequency band. A second method is capacitive decoupling. The voltage drop generate by the current flowing on a coil cancels the electromotive force induced in neighboring coil by the same current. However, the capacitive decoupling is narrow-band and is quite sensitive to the change of the decoupling capacitor. Therefore, tunable capacitors are often used in decoupling procedure performed on bench top. Unfortunately, the above two decoupling methods can only solve the coupling problem between neighboring coils. In order to provide complete decoupling between all coil elements, preamplifier

decoupling method was proposed. Since the mutual coupling is caused by the current flow in the coil element, if the current flow could be suppressed and the voltage is sensed instead by the preamplifier, the mutual coupling can be reduced to a large extent. To fulfill the decoupling, preamplifier with low input impedance (<5 ohm) is widely used in MRI RF receive-only array design because whose low input impedance can be transferred to a large impedance at the input terminal of the coil so that the current in coil is reduced and the mutual coupling is minimized.

Since coaxial cables are often used in RF coil design to connect the preamplifier with the coil, the additional phase delay added by the coaxial cable need to be taken into consideration if the preamplifier decoupling technique was adopted. The method to determine the cable's length varies for different matching networks applied. For quarter-wavelength pi matching network with characteristic impedance of $Z_c = \sqrt{Z_l Z_0}$ where Z_l is the coil input impedance and Z_0 is system impedance, if the preamp is connected to the matching network through a cable with a phase delay of integer number of 180 degree, a high impedance with value of $Z_l Z_0 / Z_p$ will be applied to the coil in which Z_p is the input impedance of the preamplifier [50]. For example, a preamplifier with input impedance of 1 ohm is connected to a coil element with input impedance of 3 ohm, a high impedance of 150 ohm (much larger than the coil input impedance) will be transferred at the coil input port and greatly suppress the current. For L-network matching, by carefully adjusting the length of the coaxial cable, preamplifier decoupling can also be achieved [65]. If the input impedance of the preamplifier is denoted as Z_p , and assume the length of the transmission line is l , the obtained impedance Z_T after the coaxial cable transformations can be derived as

$$Z_T = Z_0 \frac{Z_p + jZ_0 \tan(\beta l)}{Z_0 + jZ_p \tan(\beta l)} \quad (1.8)$$

where $\beta = \frac{2\pi}{\lambda}$

Then Z_T is in series with the capacitor in the L-matching and results in a shunt capacitor which is in parallel with the inductor in the matching network. If the length of the transmission line is adjusted properly, a parallel LC-tank resonates at Larmor frequency will be inserted into the loop coil and reduce the current in coil as shown in Figure 1.5.

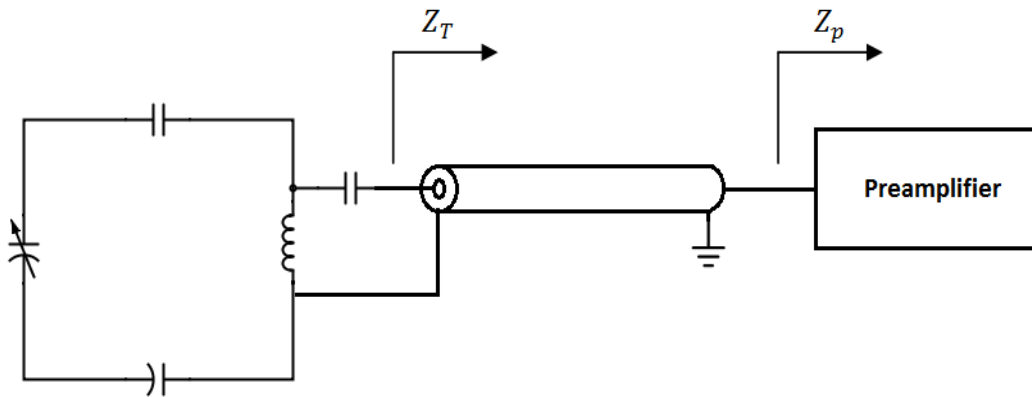


Figure 1.5: Schematic of the preamplifier decoupling for the surface coil matched using L-network.

In bench-testing, the effect of the preamplifier decoupling can be measured by using double probe as shown in Figure 1.6. The double probe is made of two small identical loops which placed adjacently. The two loops are slightly overlapped as is has been done in RF coil design to eliminate the mutual decoupling. Since the loops are relatively small compared to the RF coil, the two loops can be placed closely to the coil

and experience same electromagnetic coupling with the coil. The square root of the measured probe gain is proportional to the coil efficiency and sensitivity by reciprocity. The probes can also be used to measure the Q-factor of the coil by maximum probe gain level and the 3dB bandwidth [74].



Figure 1.6: Double-probe and single probe fabricated using semi-rigid coaxial cable. The screw can be twisted and change the overlap area of the double probe precisely to obtain optimal decoupling.

To evaluate the preamplifier decoupling, the frequency response of the isolated surface loop is measured firstly. Then the DC biased preamplifier is connected to the matched coil via the coaxial cable with proper phase delay and the frequency response is measured again. The reduction of the double probe gain reflects the effect of the preamplifier decoupling. According to experimental experience, a signal reduction close to -20dB can provide enough decoupling between two coil elements as shown in Figure 1.7.

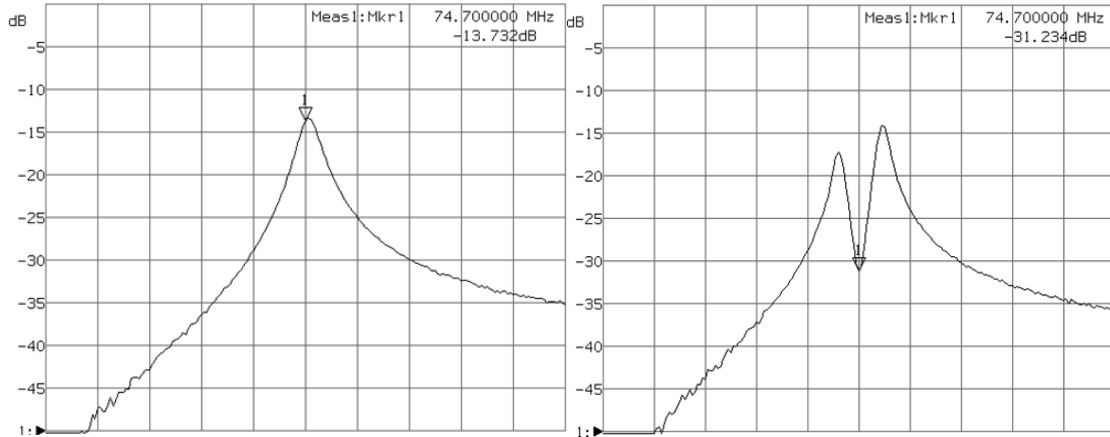


Figure 1.7: Measured probe gain of isolated coil and preamplifier decoupled coil.

1.2.5. Transmit-receive Coil

Due to the fact that the transceiver loop array transmits RF power and receives signal using the same coil structure, the design of the transceiver array is more complex than the receiver-only array. To switch between transmit and receive, a Transmit/Receive switch is necessary in the front-end circuit design as shown in Figure 1.8. Unfortunately, the preamplifier decoupling is only feasible for the receiver-only array, more effort need to be devoted into the decoupling strategies applied to the transceiver array. Just like that the mutual coupling will lower the coil sensitivity of the receiver array, the coupling between transmit elements reduces the transmit efficiency.

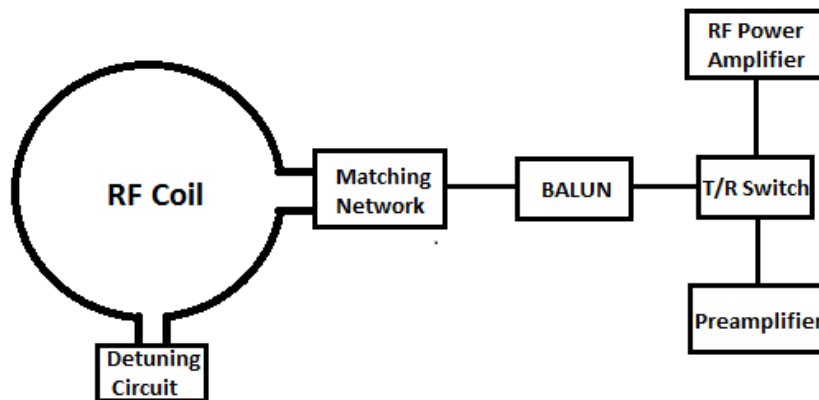


Figure 1.8: Diagram of a typical transmit and receive coil.

However, the profits of using transceiver array are also obvious. The static B_1^+ field shimming can be performed to overcome the undesirable field inhomogeneity. The magnitude and phase of each transmit element's excitation can be calculated using numerical simulation and implemented through hardware design so that the transmit energy can be focused within the field of interest which is more useful for high field MR imaging where the B_1^+ field inhomogeneity gets worse. Another advantage of employing transceiver array is that RF shield can be applied to the transceiver array and helps reduce the radiation loss so that the transmit efficiency and receive sensitivity can be greatly improved.

Following is a design example of the transceiver array for cardiac imaging application. The cardiovascular MR (CMR) is a widely used clinically for cardiac disease and treatments [36,75]. The intrinsic high SNR and CNR of high magnetic field drew increasing research interests in high-field cardiac RF coil design. However, due to the B_1^+

inhomogeneity caused by the short wavelength of the RF fields inside human tissue at high frequency, the B1 field shimming realized through hardware design is necessary to obtain a uniform field distribution within the region of interest. In this example, the B1 field of this 4-channel cardiac array is shimmed to the left of the patient (Figure 1.9 (c)). Also the front-end circuit board is positioned on the top of the coil array and performs as shield in order to lower the radiation loss and increase the transmit efficiency and receive sensitivity.

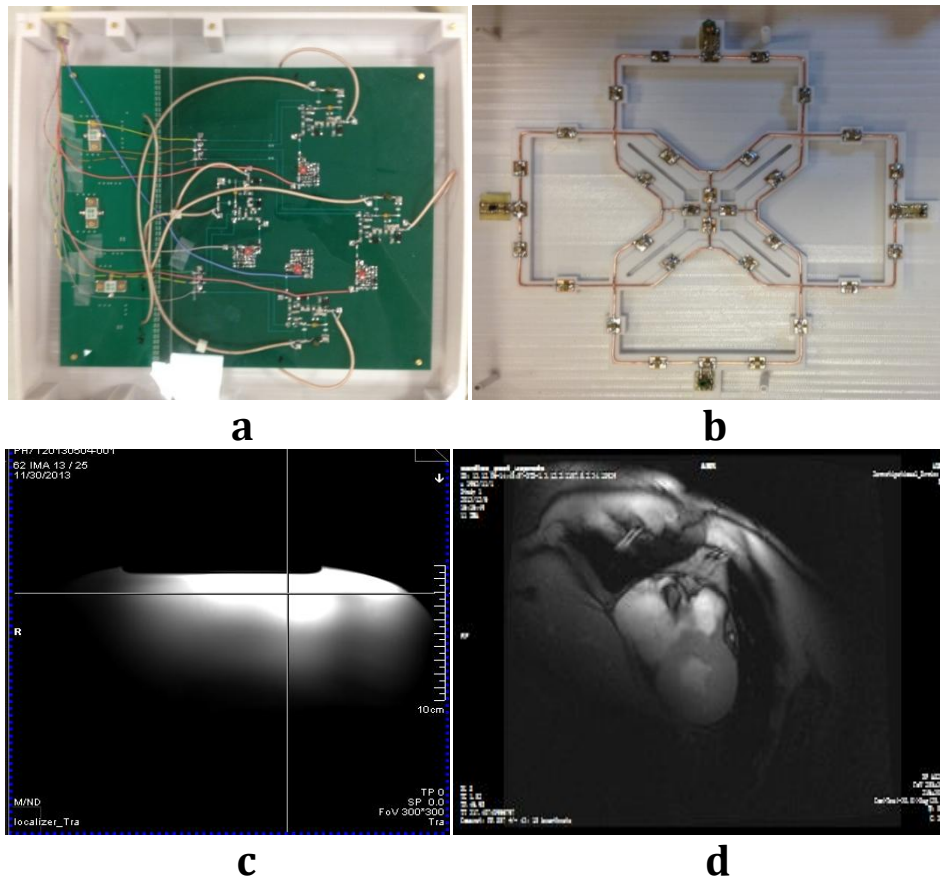


Figure 1.9: Design example of a four-channel cardiac transmit/receive array. a). Front-end circuit board b). Transmit/receive array c). Phantom image in transverse plane d). Human cardiac image.

2. Radio Frequency Front-End Circuits Design

To excite RF power and receive generated MR signal, RF front-end circuits are designed according to different MRI coil structures and applications. For multi-channel transmitting, power dividers such as hybrid and Wilkinson can be employed to split the total input power equally/un-equally and drive the transmit array elements. Conventional circular polarization or static B_1^+ field shimming can be achieved by designing the specific power ratio and phase delay for each transmit channel. On the signal reception side, low noise preamplifiers (LNA) with low input impedance are designed for magnify the weak MR signal and suppress mutual coupling between receive elements. For transceiver array, further transmit/receive switch is added for switching between power transmitting and signal receiving. In this chapter, the design optimization and fabrication procedure of several most commonly used front-end circuits in MRI application are discussed.

2.1. Wilkinson Power Divider

The Wilkinson power divider was firstly published by Ernest J. Wilkinson in 1960 for power splitting, which can achieve isolation between the output ports while maintaining a matched condition on all ports. The Wilkinson power divider designed can also be used as a power combiner because it is made up of passive components and hence reciprocal. Quarter-wavelength transmission lines or lumped elements can be used for the Wilkinson power divider fabrication.

2.1.1. Unequal Power Ratio Wilkinson Power Divider

The Wilkinson power divider/combiner is consists of two quarter-wavelength transmission line with characteristic impedance of Z_2 and Z_3 which connect in parallel at the input port as shown in Figure 2.1. A resistor is used to provide isolation between output ports and two additional quarter-wavelength transmission lines are employed to match the two output ports to the system impedance Z_0 . The characteristic impedances of the transmission lines and the value of the isolation resistor can be derived by assuming that the power split ratio between two output ports is K^2 that is $P_3 = K^2 P_2$ [55].

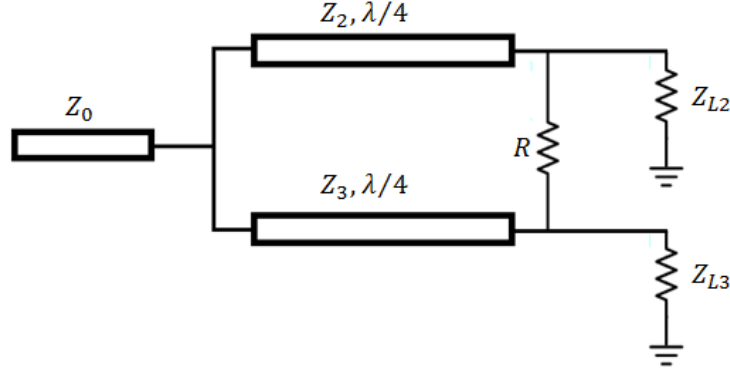


Figure 2.1: A Wilkinson power divider in microstrip form having unequal power division.

Since there's no current flows through the resistor and hence no voltage drop on it, the output voltages at output port 2 and port 3 are identical. To obtain the power split ratio K^2 , the load impedances at port 2 and port 3 should satisfy Equation (2.1)

$$K^2 Z_{L3} = Z_{L2} \quad (2.1)$$

Through the transformation of the two quarter-wavelength transmission lines, the admittance seen by the input port is

$$Y_{in} = \frac{Z_{L2}}{Z_2^2} + \frac{Z_{L3}}{Z_3^2} = Y_0 \quad (2.2)$$

by eliminating Z_{L2} using (2.1) and (2.2), it has

$$(K^2 Z_3^2 + Z_2^2) Z_{L3} = Z_2^2 Z_3^2 / Z_0 \quad (2.3)$$

With same power split ratio at the input joint of two quarter-wavelength transmission lines, the following impedance relationship can also be obtained

$$K^2 Z_3 = Z_2 \quad (2.4)$$

And in order to isolate port 2 and port 3, the isolation resistor should have the value of

$$R = \frac{Z_2 Z_3}{Z_0} \quad (2.5)$$

By using Equations (2.1), (2.3), (2.4), and (2.5), the impedances of the transmission lines and output loads can be expressed as

$$Z_2 = K\sqrt{RZ_0} \quad (2.6a)$$

$$Z_3 = \frac{1}{K}\sqrt{RZ_0} \quad (2.6b)$$

$$Z_{L2} = \frac{K^2 R}{K^2 + 1} \quad (2.6c)$$

$$Z_{L3} = \frac{R}{K^2 + 1} \quad (2.6d)$$

where the value R can be chosen arbitrarily.

To obtain similar characteristics for port 2 and port 3, the load impedance Z_{L2} and Z_{L3} can be chosen as

$$Z_{L2} = KZ_0 \quad (2.7)$$

$$Z_{L3} = \frac{Z_0}{K} \quad (2.8)$$

Two addition quarter-wavelength transmission lines are used to transform the load impedance Z_{L2} and Z_{L3} to Z_0 as shown in Figure 2.2. Then the isolation resistor value and transmission lines impedances can be calculated as

$$R = \frac{1 + K^2}{K} Z_0 \quad (2.9a)$$

$$Z_2 = Z_0 \sqrt{K(1 + K^2)} \quad (2.9b)$$

$$Z_3 = Z_0 \sqrt{\frac{1 + K^2}{K^3}} \quad (2.9c)$$

$$Z_4 = Z_0\sqrt{K} \quad (2.9d)$$

$$Z_5 = \frac{Z_0}{\sqrt{K}} \quad (2.9e)$$

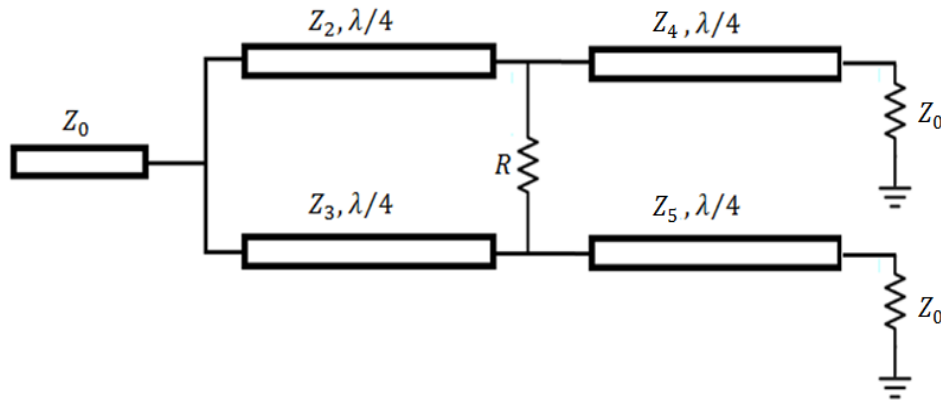


Figure 2.2: Schematic of unequal Wilkinson power divider with additional transmission lines for impedance matching.

To meet the power dividing/combining requirements of the study in Chapter 3, two unequal split Wilkinson power dividers with power split ratio of 2:1 and 5:1 at 120.3MHz and 297.2MHz respectively were designed and fabricated. Firstly, the theoretical values of the resistors and transmission line impedances were calculated using Equations (2.9 a-e) and are listed in Table 2.1

Power Ratio	R	Z_2	Z_3	Z_4	Z_5
2:1	106.07	51.49	102.99	42.04	59.46
5:1	134.16	36.63	183.14	33.44	74.77

Table 2.1: Theoretically calculated values for isolation resistors and characteristic impedances of transmission lines for unequal Wilkinson power divider.

However, the quarter-wavelength in free space is approximate 25.24 cm at 297.2MHz and 62.34 cm at 120.3MHz which are too long for the front-end circuits designed for MRI application. To overcome this problem, lumped element low-pass pi networks were used to replace quarter-wavelength transmission lines at single frequency point. The inductor and capacitor values can be calculated using following equations:

$$L = \frac{Z_0 \sin(\phi)}{\omega_0} \quad (2.10)$$

$$C = \frac{1 - \cos(\phi)}{\omega_0 Z_0 \sin(\phi)} \quad (2.11)$$

where $\phi = 90^\circ$ for quarter-wavelength transmission line and $\omega = 2\pi f_0$. The calculated lumped element components' values were used in the layout simulation performed in ADS Momentum (Agilent Technologies, Palo Alto, California, USA) and optimized for best circuit performance. The layouts of the power dividers were firstly designed in FreePCB and then imported into ADS simulation. Using the ADS Momentum simulation can take the power loss and phase delay brought in by the copper trace on 1/32" FR4 substrate into consideration which could provide more accurate

simulation results and help simplify the tuning procedure on bench. The simulation results for the unequal Wilkinson power dividers are shown in Figure 2.4 and Figure 2.5.

The bench measurements of the dividers are shown in Figure 2.6 and Figure 2.7.

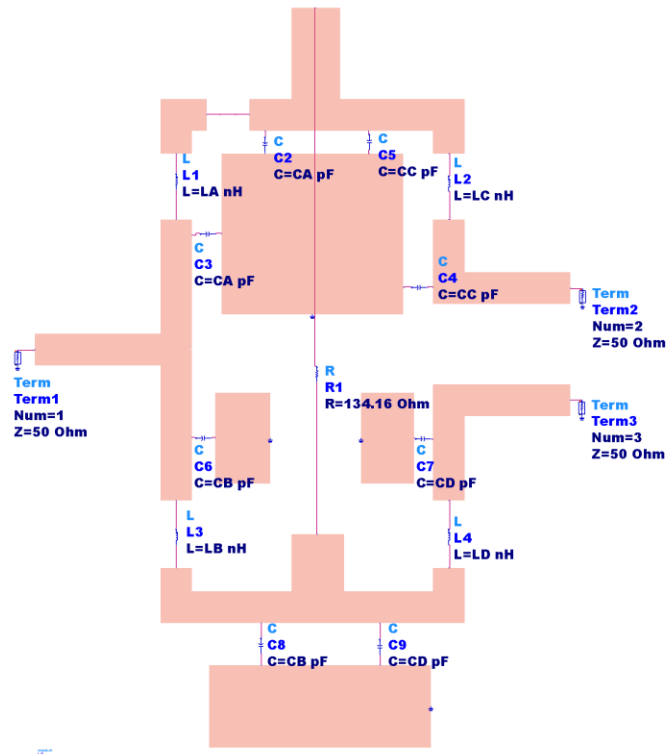


Figure 2.3: Layout of the unequal Wilkinson power divider used in ADS Momentum simulation.

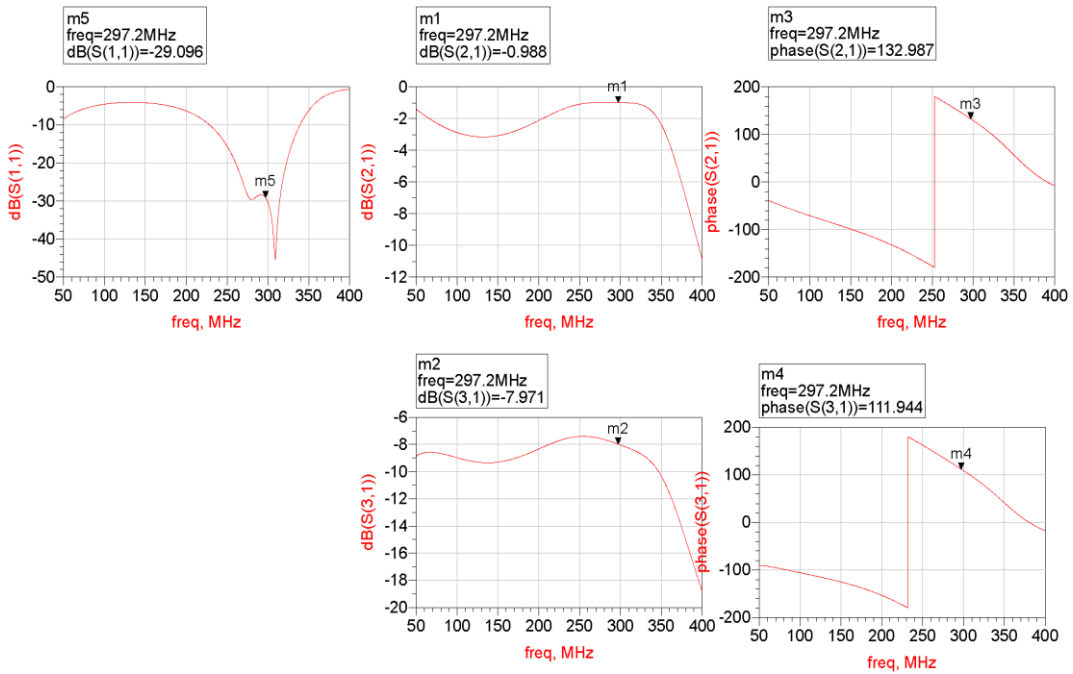


Figure 2.4: Simulation results for 1:5 unequal Wilkinson power divider at 297.2MHz.

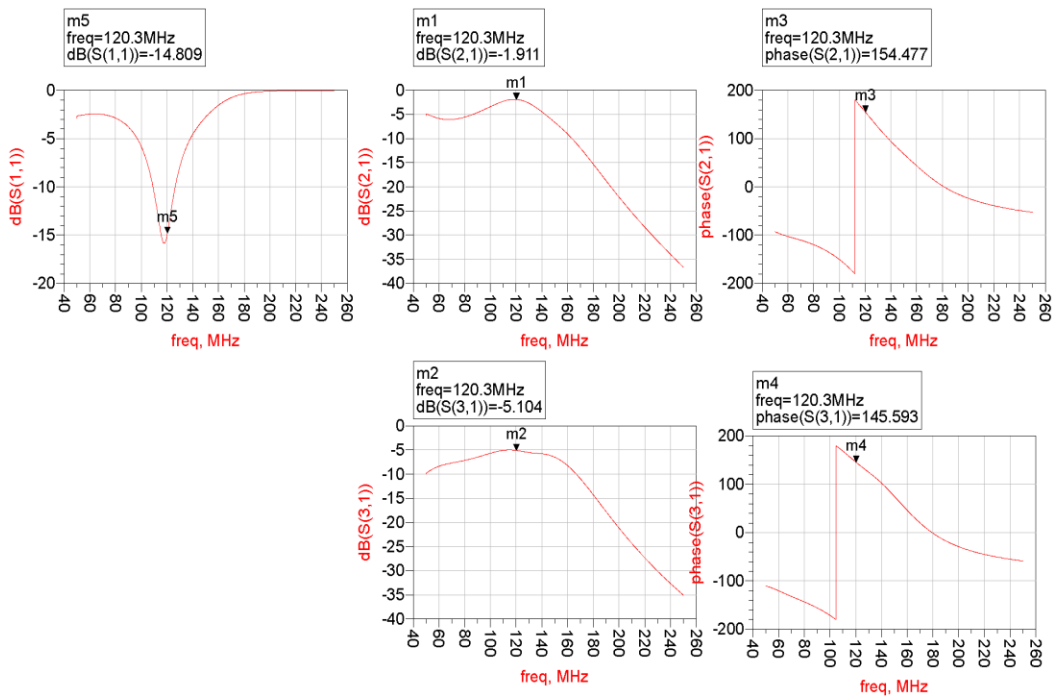


Figure 2.5: Simulation results for 1:2 unequal Wilkinson power divider at 120.3MHz.

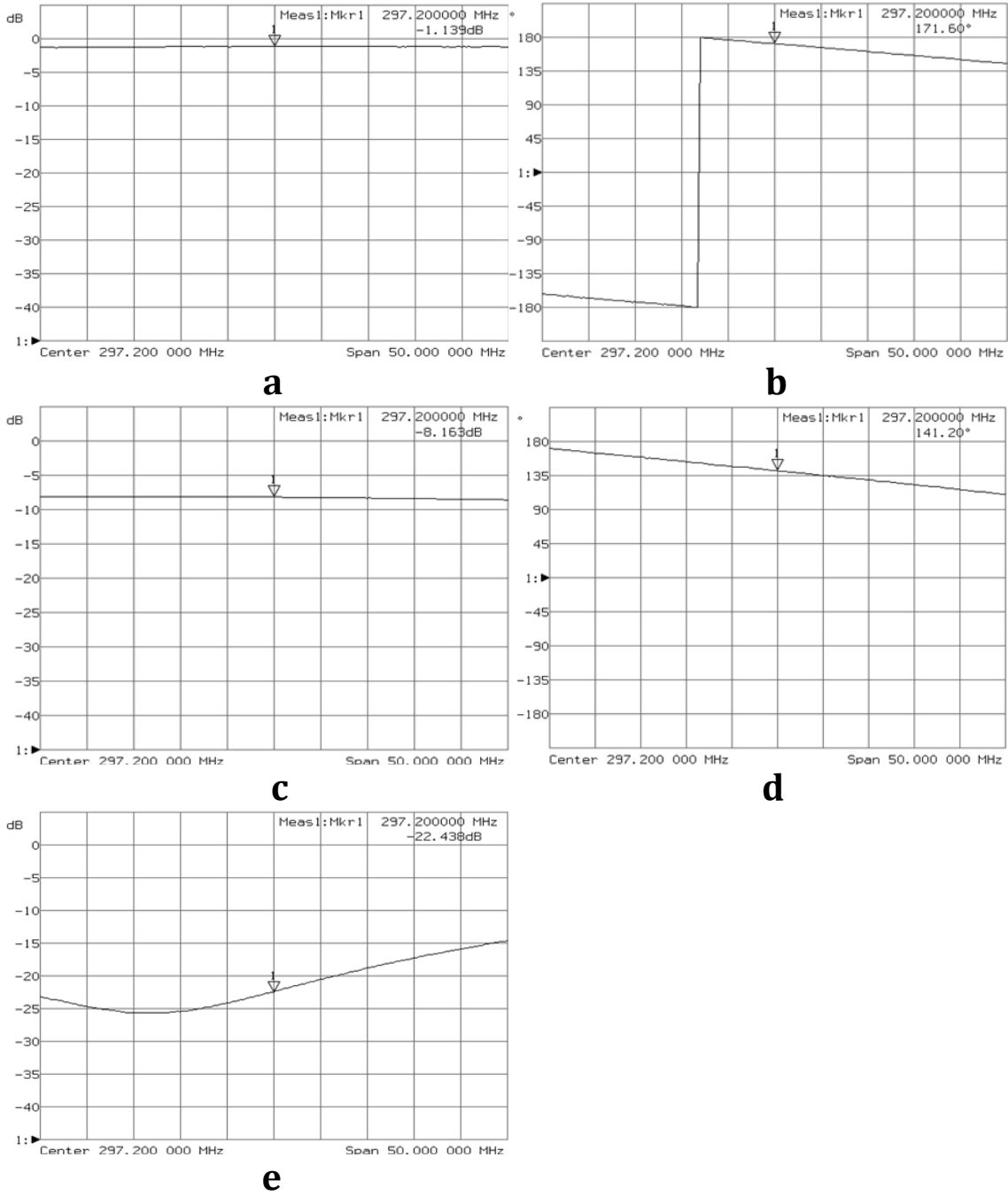


Figure 2.6: Measured S-parameters of the fabricated 1:5 unequal Wilkinson power divider at 297.2MHz. a). Mag(S21) b). Phase(S21) c). Mag(S31) d). Phase(S31) e). Mag(S11).

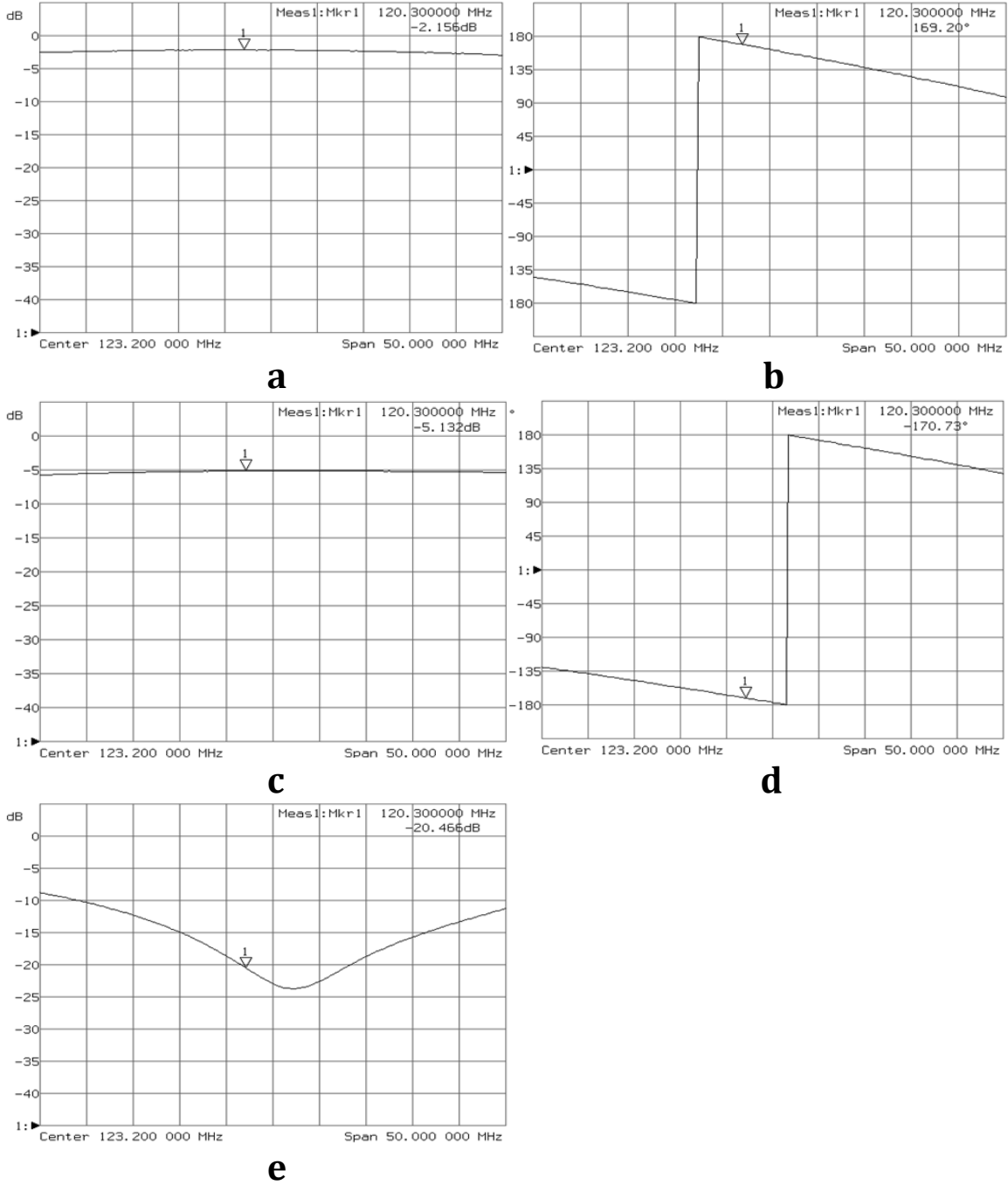


Figure 2.7: Measured S-parameters of the fabricated 1:2 unequal Wilkinson power divider at 120.3 MHz. a). Mag(S21) b). Phase(S21) c). Mag(S31) d). Phase(S31) e). Mag(S11).

2.1.2. Broadband Wilkinson Power Divider

The design of the broadband Wilkinson power divider followed that of a dual-band Wilkinson power divider whose main idea is to use a two-section transformer with different characteristic impedances and physical lengths for each section to realize simultaneous impedance matching at dual frequencies of interest [56]. The two-section transformer is illustrated in Figure 2.8.

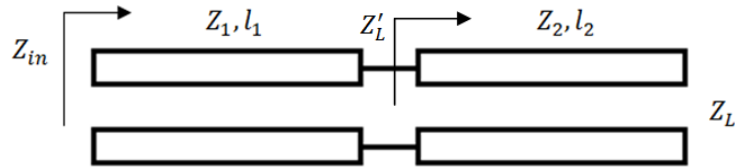


Figure 2.8: Schematic representation of a two-section transformer.

The input impedances Z_{in} and Z'_L at intersections can be derived as

$$Z_{in} = Z_1 \frac{Z'_L + jZ_1 \tan(\beta l_1)}{Z_1 + jZ'_L \tan(\beta l_1)} \quad (2.12)$$

$$Z'_L = Z_2 \frac{Z_L + jZ_2 \tan(\beta l_2)}{Z_2 + jZ_L \tan(\beta l_2)} \quad (2.13)$$

By equating equation (2.12) to Z_0 and solving Z'_L from it, it has

$$Z'_L = Z_1 \frac{Z_0 - jZ_1 \tan(\beta l_1)}{Z_1 - jZ_0 \tan(\beta l_1)} \quad (2.14)$$

The real and imaginary parts of Equations (2.13) and (2.14) are identical, so it can be derived that

$$\tan(\beta l_1) \tan(\beta l_2) = \frac{Z_1 Z_2 (Z_L - Z_0)}{Z_1^2 Z_L - Z_2^2 Z_0} \quad (2.15)$$

$$\frac{\tan(\beta l_1)}{\tan(\beta l_2)} = \frac{Z_1 (Z_2^2 - Z_L Z_0)}{Z_2 (Z_L Z_0 - Z_1^2)} \quad (2.16)$$

Above two equations should hold for both two frequencies and yield to

$$l_1 = l_2 = \frac{\pi}{\beta_1 + \beta_2} \quad (2.17)$$

$$Z_1 = \left(\frac{Z_0}{2\alpha} (Z_L - Z_0) + \left(\left[\frac{Z_0}{2\alpha} (Z_L - Z_0) \right]^2 + Z_0^3 Z_L \right)^{\frac{1}{2}} \right)^{\frac{1}{2}} \quad (2.18)$$

$$Z_2 = \frac{Z_0 Z_L}{Z_1} \quad (2.19)$$

where $\alpha = (\tan(\beta l_1))^2 = (\tan(\beta l_2))^2$

The resistor values and transmission lines characteristic impedances of the dual-band Wilkinson power divider can be obtained by applying the derivation results of two-section transformer to even/odd mode analysis of Wilkinson power divider[59]. Using even mode analysis, the transmission line impedances can be derived by plugging $R_L = 2Z_0$ into Equations (2.18) and (2.19), and it has

$$Z_1 = Z_0 \left(\frac{1}{2\alpha} + \left(\frac{1}{4\alpha^2} + 2 \right)^{1/2} \right)^{1/2} \quad (2.20)$$

$$Z_2 = \frac{2Z_0^2}{Z_1} \quad (2.21)$$

Then the resistor values can be obtained from odd-mode analysis and the above characteristic impedance and physical length of the transmission lines.

The dual frequencies of the Wilkinson power divider were set at $f_1 = 166.7MHz$, $f_2 = 333.3MHz$ and the center frequency f_0 is located at $250MHz$. The parameters of the transmission lines and isolated resistors were calculated as $Z1=75.97$ ohm, $Z1=65.81$ ohm, $R1=136.4$ ohm, $R2=164.7$ ohm, $L1=52.75$ degree, $L2=127.25$ degree. To make the dimension of the broadband power divider reasonable at MR frequencies, the transmission lines in the power divider were also replaced by lumped element pi networks. However, unlike the single frequency application, using lumped element in broadband design will cause problem since it only equivalent to transmission line at the single frequency it was designed. To realize broadband functionality, the center frequency $250MHz$ was used in the calculation of all the lumped element pi networks and circuit optimization tool of ADS was employed to optimize all the capacitor and inductor values over a wide frequency band as shown in Figure 2.9.

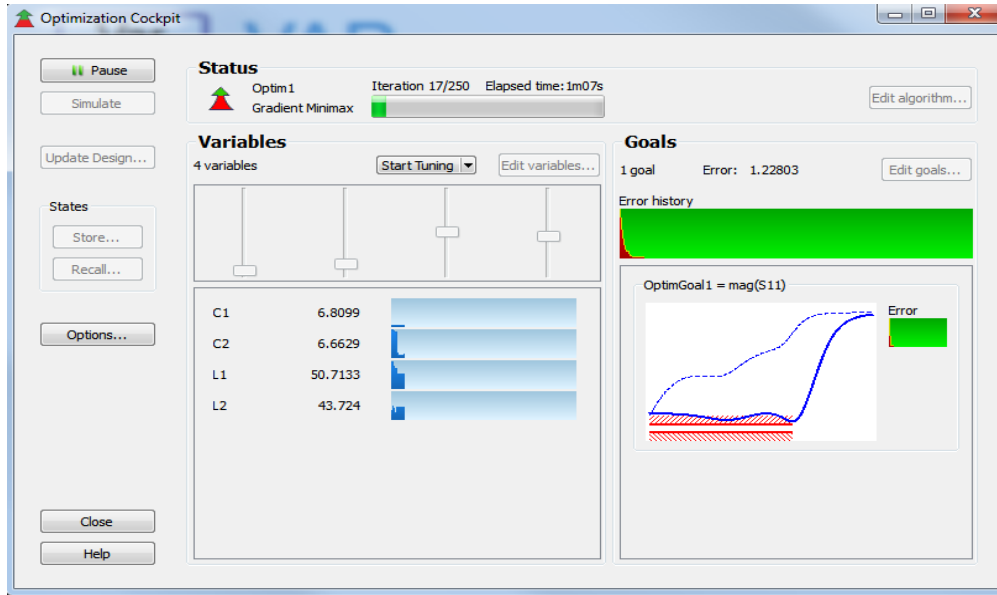


Figure 2.9: Control panel of the ADS circuit performance optimization. For the broadband Wilkinson power divider, the magnitude of the reflection coefficient was optimized over a wide frequency band.

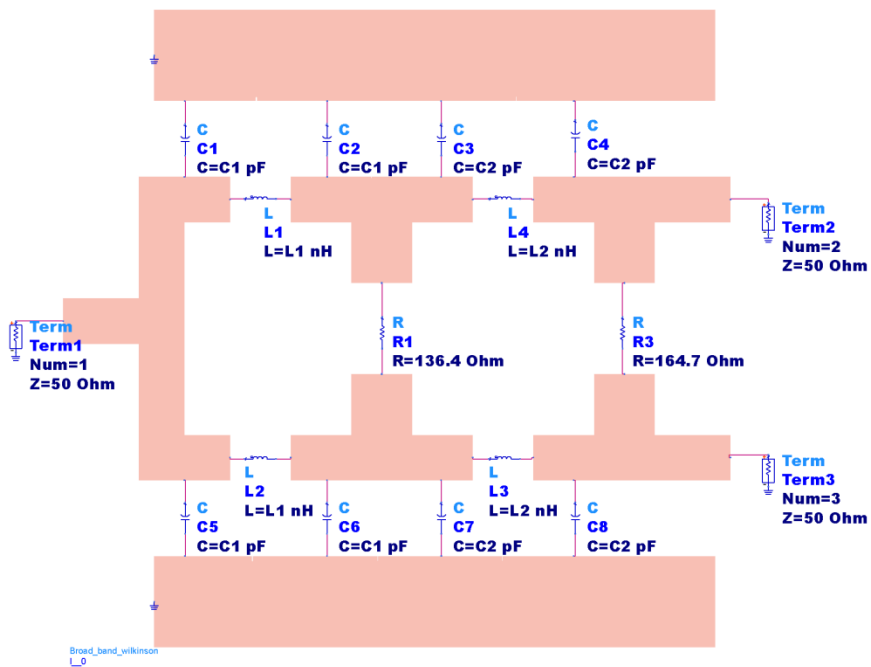


Figure 2.10: Layout of the broadband Wilkinson power divider used in ADS Momentum simulation.

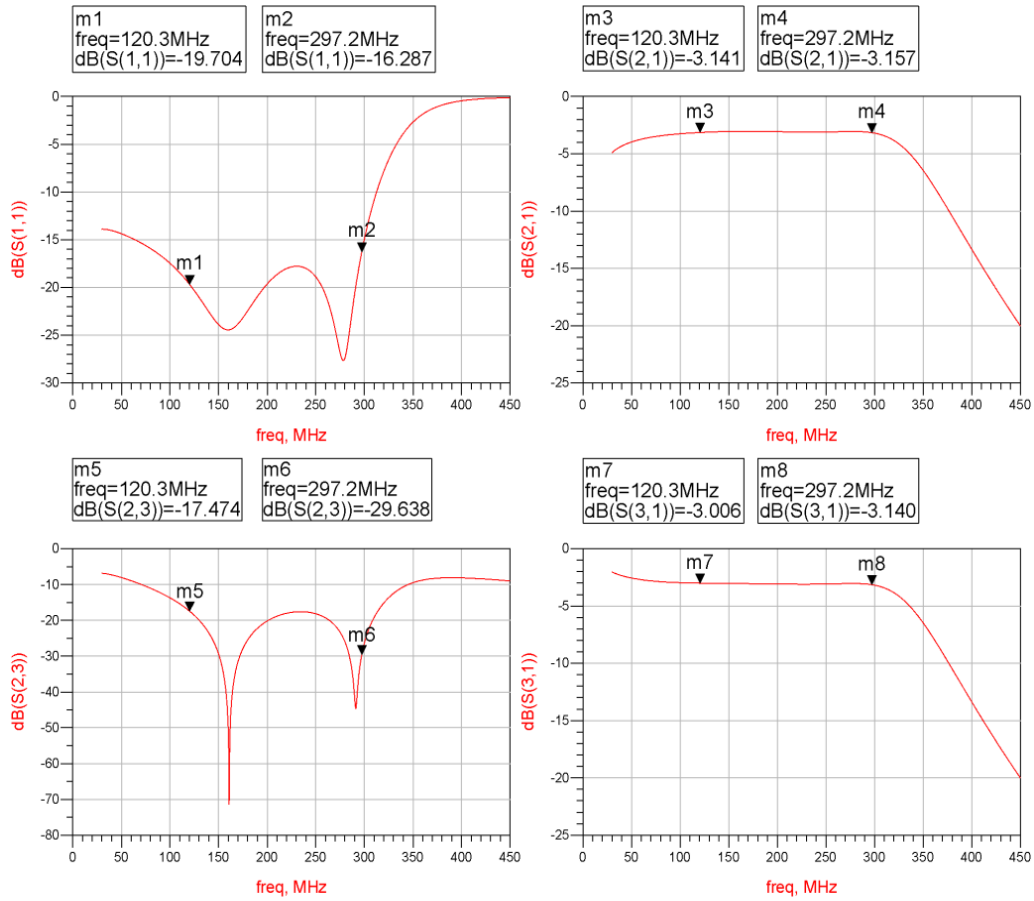


Figure 2.11: Simulation results for broadband Wilkinson power divider from DC to 400MHz.

Then the optimized components values and designed circuit layout were directly used in the fabrication. Due to the tolerance of the commercial available components, some further adjustments on component values were conducted to achieve best circuit performance. Following are the bench-testing results of the broadband Wilkinson power divider/combiner fabricated. The measurement results match well with the simulation results as shown in Figure 2.12. The input power is split equally (Amplitude balance = ± 0.1 dB) and the phase difference between two output ports is controlled within 5 degree.

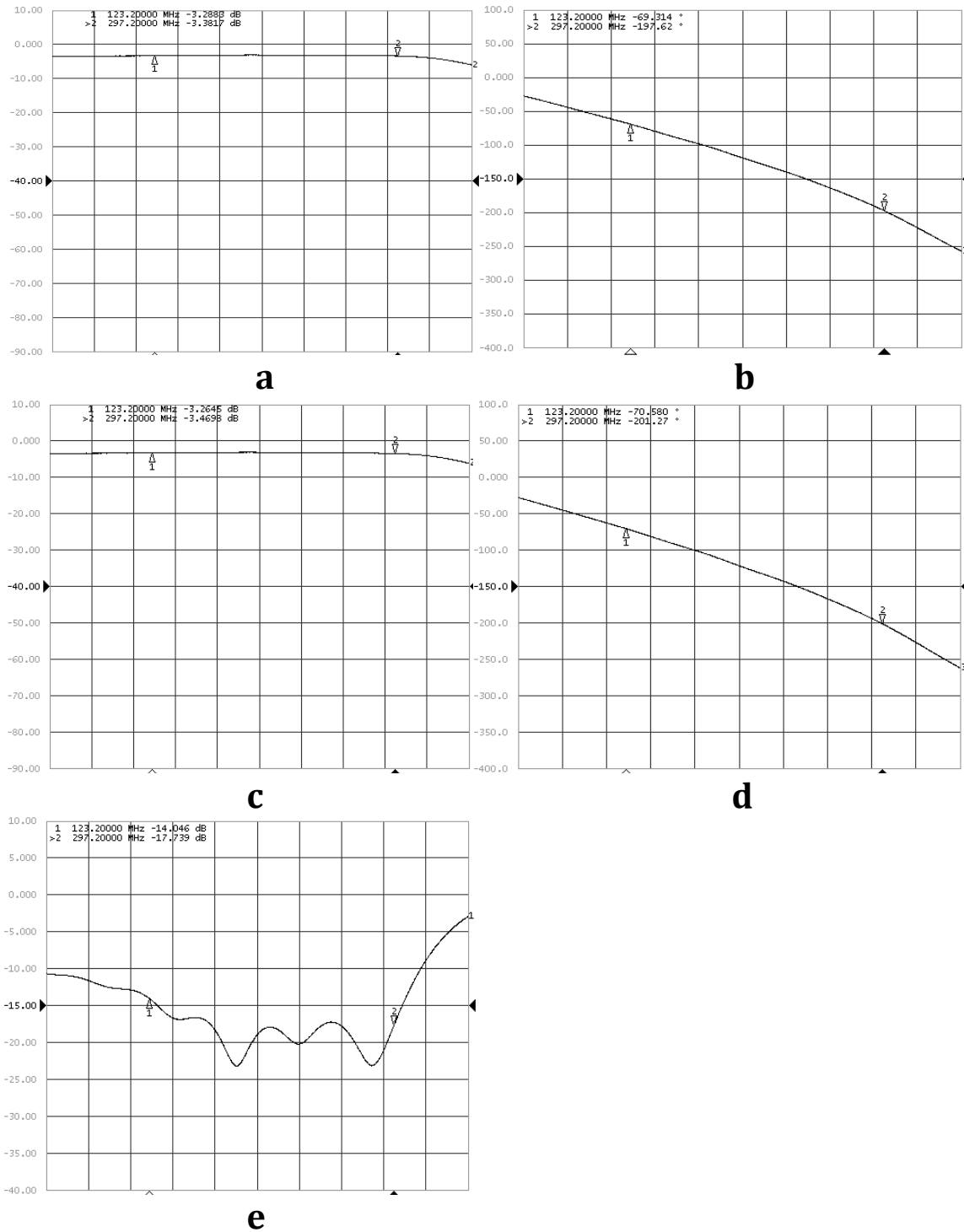


Figure 2.12: Measured S-parameters of the fabricated broadband Wilkinson power divider at both 123.2MHz and 297.2MHz. a). Mag(S₂₁) b). Phase(S₂₁) c). Mag(S₃₁) d). Phase(S₃₁) e).

Mag(S₁₁).

2.2. T/R Switch

For high scanning image quality and patient safety, MRI RF coils need T/R switches to provide reliable and fast switching between power transmission and signal receiving within the short durations of the RF pulses. The main goals of T/R switch design are: first, the attenuation of both transmit and receive channels need to be minimized in order to prevent too much loss in transmit efficiency and receive sensitivity. Secondly, the isolation between transmit channel and receive channel is maximized to prevent high transmit power being coupled into receive loops. The schematic of the T/R switch design is shown in the Figure 2.13.

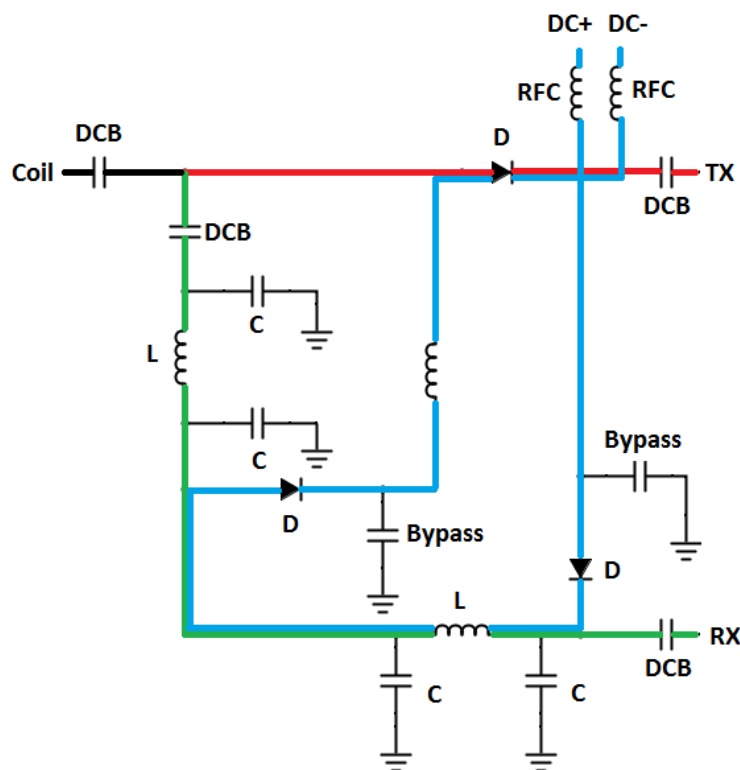


Figure 2.13: Schematic of the Transmit/Receive switch.

To completely shut down the receive channel during transmitting, the PIN diodes in the above schematic are forward biased using DC signal and connect the quarter-wavelength pi networks directly to ground (short). This short is then transformed to an open at the other end of the pi-network which blocks the transmit power from receive channel. In order to provide excellent isolation ($<-30\text{dB}$) between transmit and receive channels, two sections of the quarter-wavelength lumped element pi networks were used in the T/R switch design. The capacitors and inductors values in the pi-network were optimized to obtain low insertion loss and high isolation simultaneously. The transmit channel design was relatively simple, a high voltage PIN diode is forward biased during transmitting and turned off when receive channel is activated.

For the purpose of switching between transmit and receive for both proton and phosphorous signals at 7T, T/R switches were designed at 120.3MHz and 297.2MHz separately due to the narrow-band property of the pi-network. Figure 2.14 and Figure 2.15 show the measurement results of the T/R switches designed for 120.3MHz and 297.2MHz.

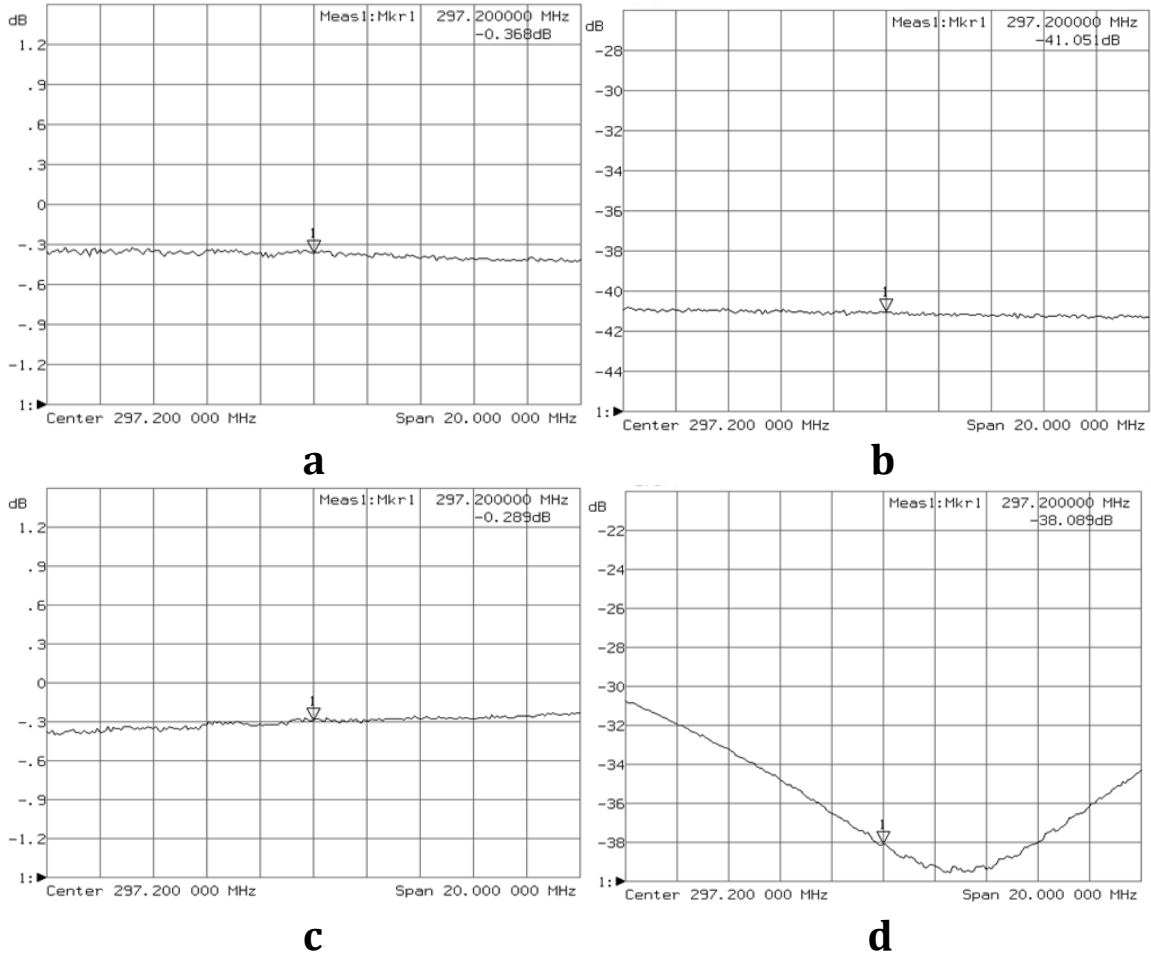


Figure 2.14: Measurement results for 297.2MHz T/R switch. a). Insertion loss of receive channel
 b). Isolation of receive channel c). Insertion loss of transmit channel d). Isolation of transmit channel.

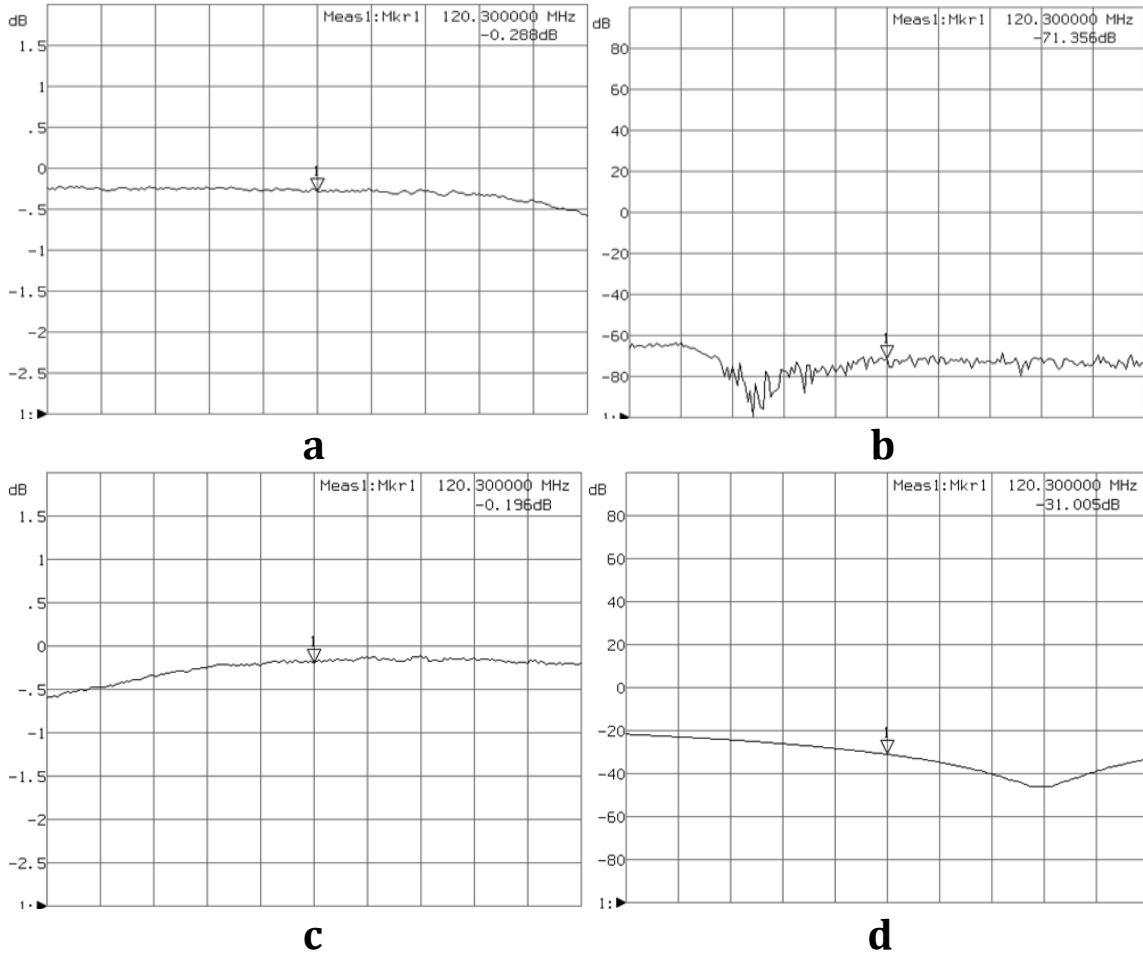


Figure 2.15: Measurement results for 120.3MHz T/R switch. a). Insertion loss of receive channel b). Isolation of receive channel c). Insertion loss of transmit channel d). Isolation of transmit channel.

2.3. Diplexer

To make both 1H and 31P signals share the same coil structure during RF power transmitting, a diplexer was designed and fabricated for low frequency signal (120.3MHz) and high frequency signal (297.2MHz) coexistence. According to the theory of the diplexer, two band-stop filters with center frequencies at 120.3MHz and 297.2MHz were firstly designed for 50 ohm system using Elsie as shown in Figure 2.16 and Figure 2.17.

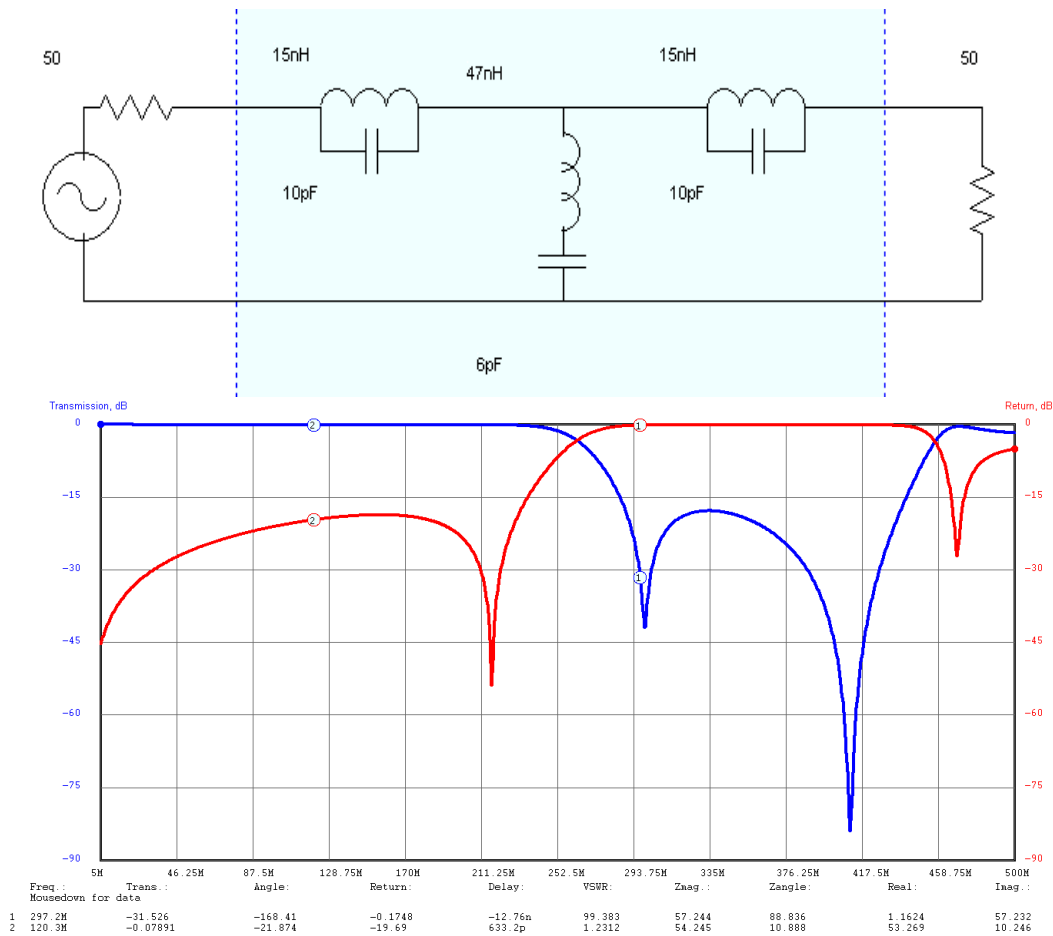


Figure 2.16: a) Schematic of the band-stop filter at 297.2MHz

b) Simulated transmission (in Blue) and return (in Red) loss of the band-stop filter.

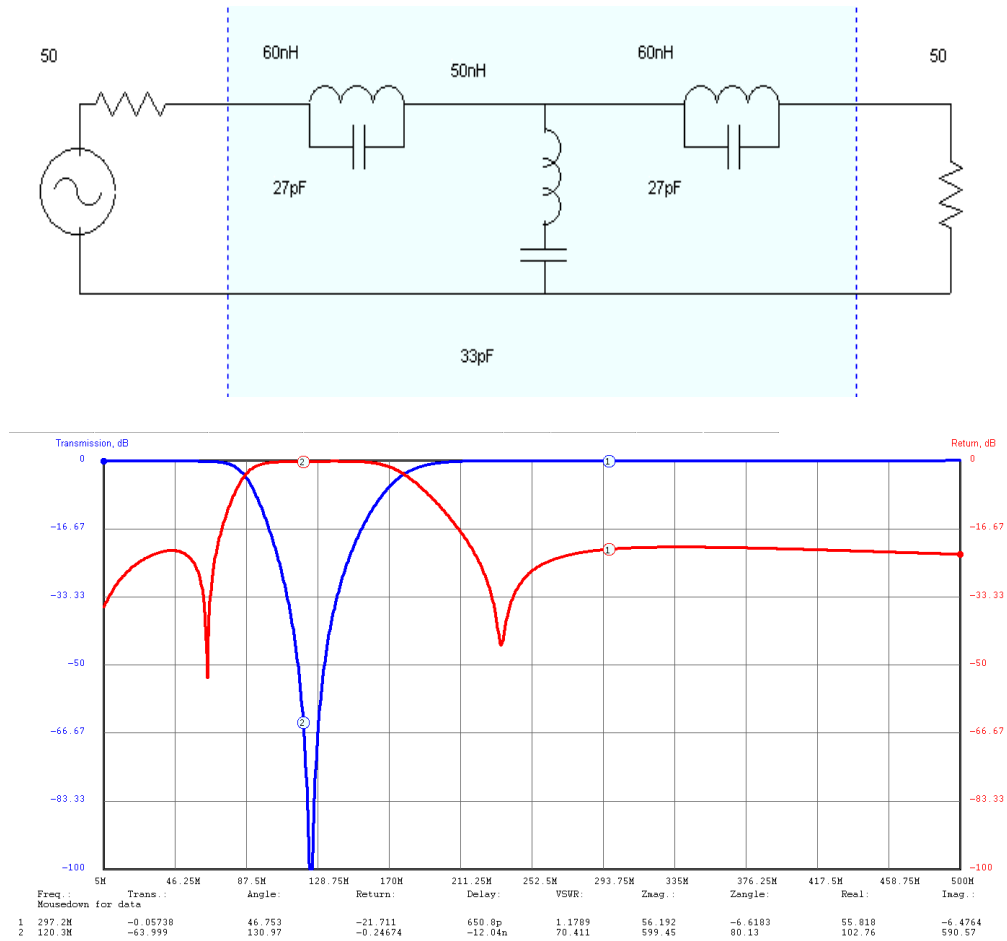


Figure 2.17: a) Schematic of the band-stop filter at 120.3MHz

b) Simulated transmission (in Blue) and return (in Red) loss of the band-stop filter.

Then these two designed filters were connected to a common port to implement frequency domain multiplexing. However, the coupling between two filters will impact the performance negatively. Additional optimization based on the attenuations and isolations at target frequencies was performed. The diplexer was first simulated in ADS momentum with circuit layout imported and then fabricated on 1/32" fr4 board with one ounce copper thickness.

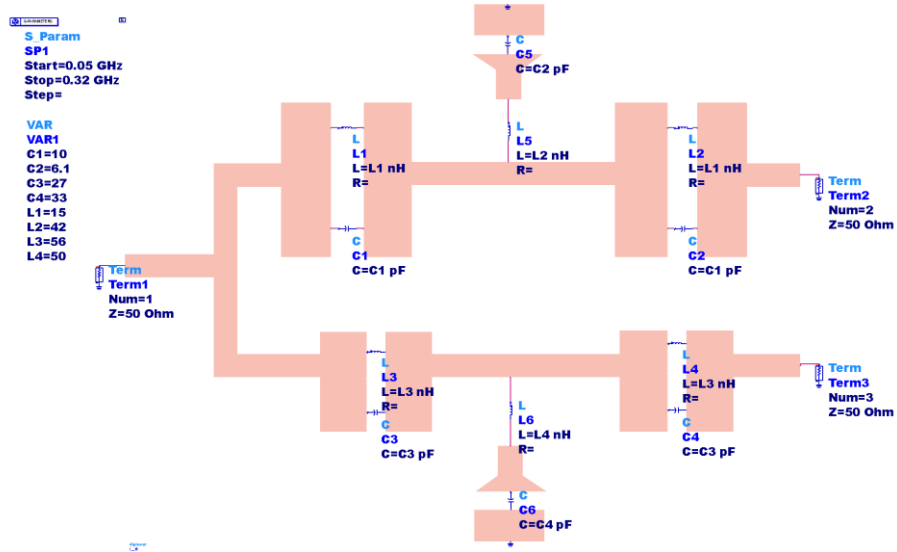


Figure 2.18: Layout of the diplexer used in ADS Momentum simulation.

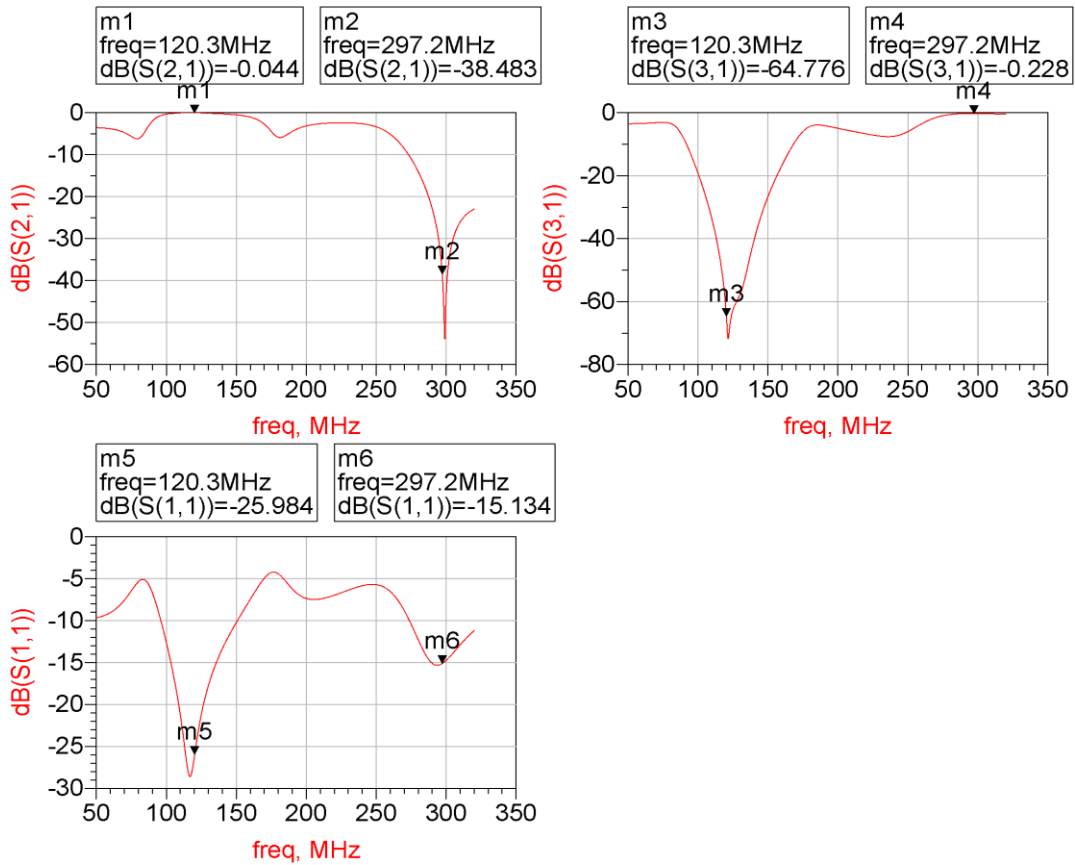


Figure 2.19: Simulation results for diplexer from 50MHz to 350MHz.

After circuit performance optimization in simulated, the diplexer was fabricated and measured on bench top. The measurement results are shown in Figure 2.20. The insertion losses at both frequencies are controlled below -0.35 dB and the isolations are lower than -40 dB.

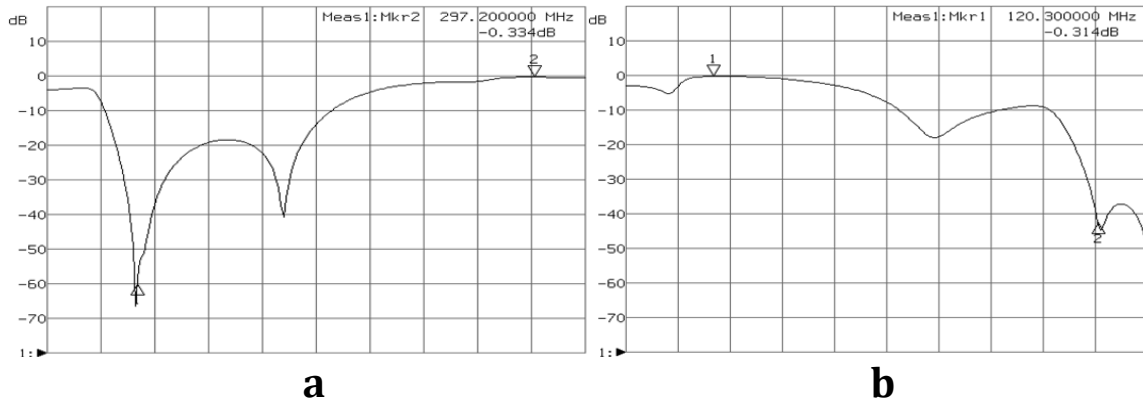


Figure 2.20: Measurement results for diplexer a). High frequency channel b). Low frequency channel.

2.4. Low Noise Preamplifier

As mentioned in Chapter 1, low noise amplifier (LNA) is widely used in the MRI RF coil design to magnify the weak MR signal and eliminate the mutual coupling between neighboring coils by tuning the input impedance of the preamplifier to a small value [50]. However, to meet the specific requirements of the study that will be discussed in Chapter 3, the design procedure of a high input impedance preamplifier is discussed in this section.

A two stages LNA structure was employed for the high input impedance preamplifier design as shown in Figure 2.21. Since the noise level of the first stage dominates the whole noise figure of preamplifier according to Equation (2.2), a low noise FET transistor ATF54143 (Avego Technologies., San Jose, California, USA) was chosen for the first stage signal amplification. To provide further amplification to the MR signal, a NPN bipolar transistor BFP720 (Infineon Technologies, Neubiberg, Germany) was used in the second stage. Active DC bias circuits were designed for both stages of the preamplifier to provide 3V, 40mA bias to ATF54143 and 3V, 15mA to BFP720 as shown in Figure 2.22.

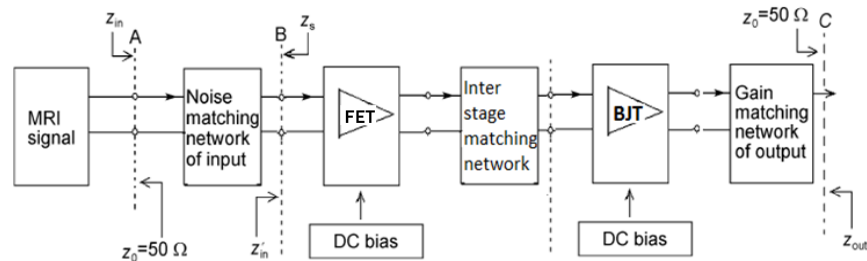


Figure 2.21: Block diagram of a two-stage LNA designed for MRI application.

$$N_F^2 = N_{f_1}^2 + \frac{N_{f_2}^2}{G_1^2} + \frac{N_{f_3}^2}{G_1^2 G_2^2} + \dots \quad (2.22)$$

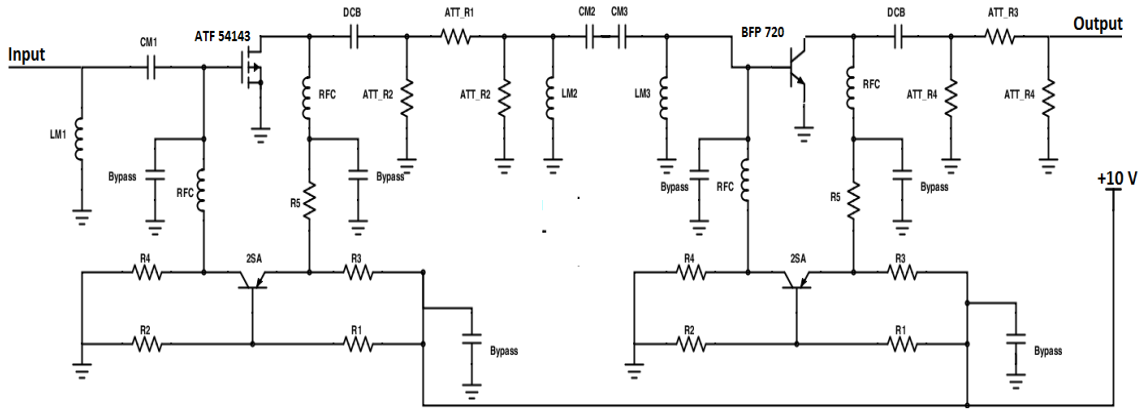


Figure 2.22: Schematic of the high input impedance preamplifier.

Because of that the ATF 54143 is fabricated specifically for wireless communication application (450 MHz~6 GHz), the transistor parameters such as transistor stability were not optimized for low frequency application (<400 MHz). To prevent the transistor oscillate during operation in scanner, pi attenuators were added at the output of the transistors at both frequencies to make the transistor unconditionally stable ($K > 1$) at MR frequencies as shown in Figure 2.23.

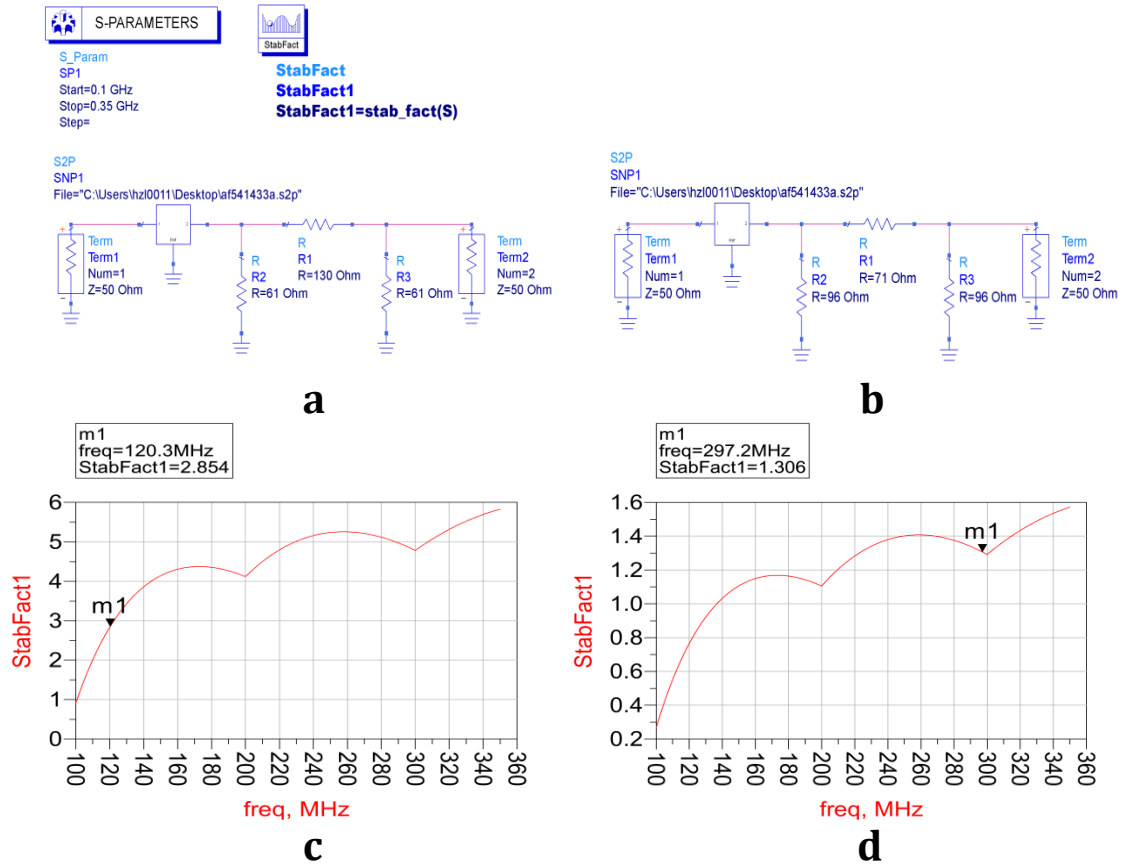


Figure 2.23: Simulated stability factor of ATF54143 with attenuators added at c).123.3 MHz and d). 297.2 MHz.

After achieving unconditionally stable, the S-parameters, NF_{min} , Γ_{opt} and R_n of transistor and the pi attenuators were re-simulated for LNA design as shown in Table 2.2.

Frequency	120.3 MHz	297.2 MHz
S11	0.916-j0.346	0.595-j0.708
S12	0.0007+j0.003	0.003+j0.007
S21	-7.618+j1.849	-5.983+j3.794
S22	0.055-j0.015	0.042-j0.031
NF_{min}	0.235	0.241
Γ_{opt}	0.306+j0.229	0.277+j0.285
R_n	2.739	2.728

Table 2.2: Simulated transistor parameters with attenuator attached.

For the high input impedance preamplifier design, an arbitrary Γ_L was firstly selected arbitrarily within the constant gain circle (gain>11dB) calculated using following equations so that the first stage of the preamplifier can provide a reasonable gain [49].

$$\left| \Gamma_L - \frac{(S_{22}^* - \Delta^* S_{11})G}{1 + G(|S_{22}|^2 - |\Delta|^2)} \right|^2 = \frac{1 - 2K|S_{12}S_{21}|G + |S_{12}S_{21}|^2G^2}{1 + G(|S_{22}|^2 - |\Delta|^2)^2} \quad (2.23)$$

$$Center = \frac{(S_{22}^* - \Delta^* S_{11})G}{1 + G(|S_{22}|^2 - |\Delta|^2)} \quad (2.24)$$

$$Radius = \frac{\sqrt{1 - 2K|S_{12}S_{21}|G + |S_{12}S_{21}|^2G^2}}{1 + G(|S_{22}|^2 - |\Delta|^2)} \quad (2.25)$$

where $G = G_{desired}/|S_{21}|^2$ and $\Delta = S_{11}S_{22} - S_{21}S_{12}$

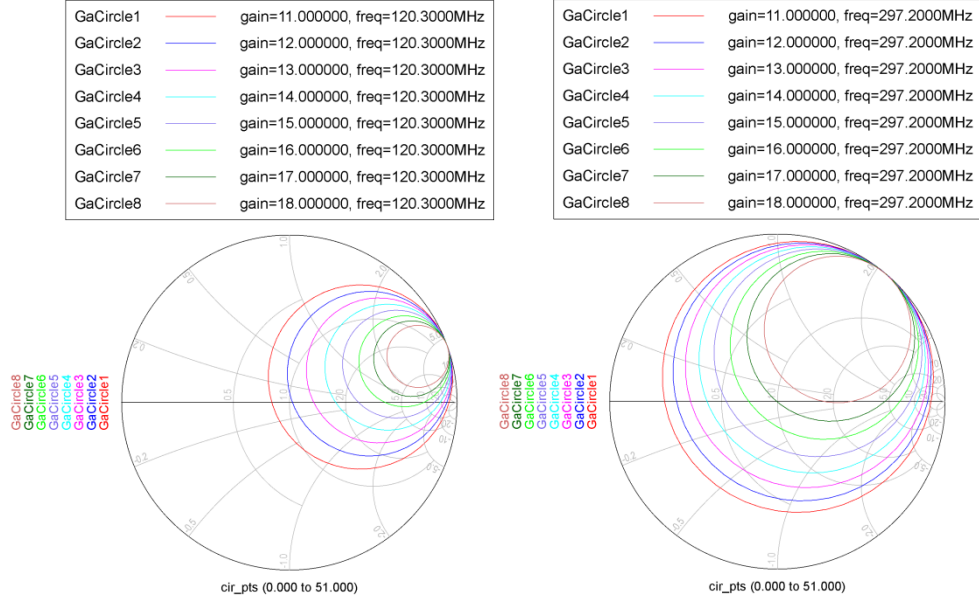


Figure 2.24: Constant gain circles of ATF54143 with attenuator at both 120.3MHz and 297.2MHz.

Then Γ_{IN} was calculated using equation

$$\Gamma_{IN} = \frac{S_{11} - \Delta\Gamma_L}{1 - S_{22}\Gamma_L} \quad (2.26)$$

And Γ'_{IN} can be obtained using preamplifier high input impedance by

$$\Gamma'_{IN} = \frac{Z'_{IN} - Z_0}{Z'_{IN} + Z_0} \quad (2.27)$$

With above derived equations, a circle of Γ_s with following center and radius can be found as [70, 71]

$$C = \frac{(1 - |\Gamma'_{IN}|^2)\Gamma_{IN}^*}{1 - |\Gamma'_{IN}\Gamma_{IN}|^2} \quad (2.28)$$

$$R = \frac{(1 - |\Gamma'_{IN}|^2)|\Gamma'_{IN}|}{1 - |\Gamma'_{IN}\Gamma_{IN}|^2} \quad (2.29)$$

However, above equations can only return a Γ_s which guarantees a preamplifier input impedance with high input reflection coefficient. To accomplish a high input impedance with real value, further selection on the calculated Γ_s need to be performed. As shown in Figure 2.25, through the L-matching network Z'_{IN} is matched to Z_{IN} and in reciprocity Z_s is matched to Z_0 .

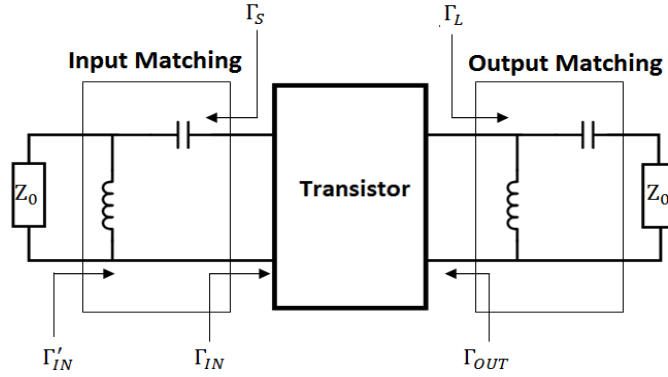


Figure 2.25: Illustration of input and output matching networks for first stage of the high input impedance preamplifier.

With Z_{IN} (Equation (2.23)) and Z'_{IN} (high input impedance) known, the inductor and capacitor values in the L-network can be obtained. Then the Z_s which can be transferred to Z_0 using the same designed matching network was selected for NF and gain calculation using following equations

$$G_T = \frac{|S_{21}|^2(1 - |\Gamma_s|^2)(1 - |\Gamma_L|^2)}{|1 - \Gamma_s\Gamma_{IN}|^2|1 - S_{22}\Gamma_L|^2} \quad (2.30)$$

$$NF = NF_{min} + \frac{4R_n|\Gamma_s - \Gamma_{opt}|^2}{(1 - |\Gamma_s|^2)(1 + \Gamma_{opt})^2} \quad (2.31)$$

The Γ_s gave best NF and gain was chosen for high-input impedance preamplifier implementation as listed in Table 2.3.

Frequency	120.3 MHz	297.2 MHz
Γ_L	0.0554-j0.0832	0.034+j0.1971
Γ_s	-0.013+j0.0417	-0.0748+j0.0775
L (Input Matching)	384.50 nH	63.32 nH
C (Input Matching)	312.82 pF	47.55 pF
Input Impedance	5000 ohm	1500 ohm
NF	0.3673 dB	0.2625 dB
Gain	11.77 dB	16.89 dB

Table 2.3: Parameters of the designed first stage of the preamplifier

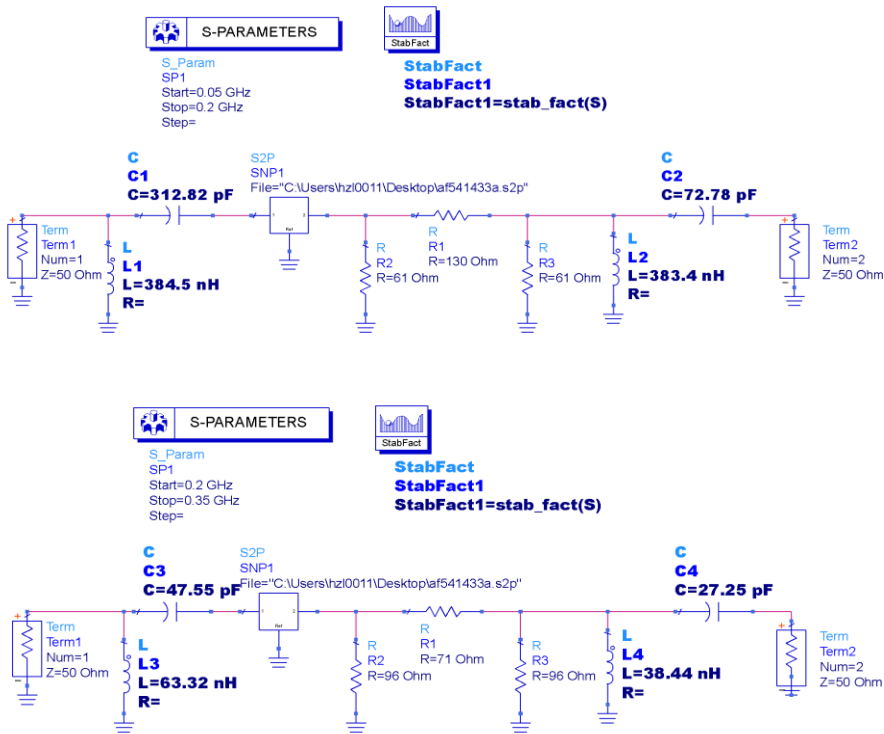


Figure 2.26: Simulation schematic of the first stage of the preamplifier.

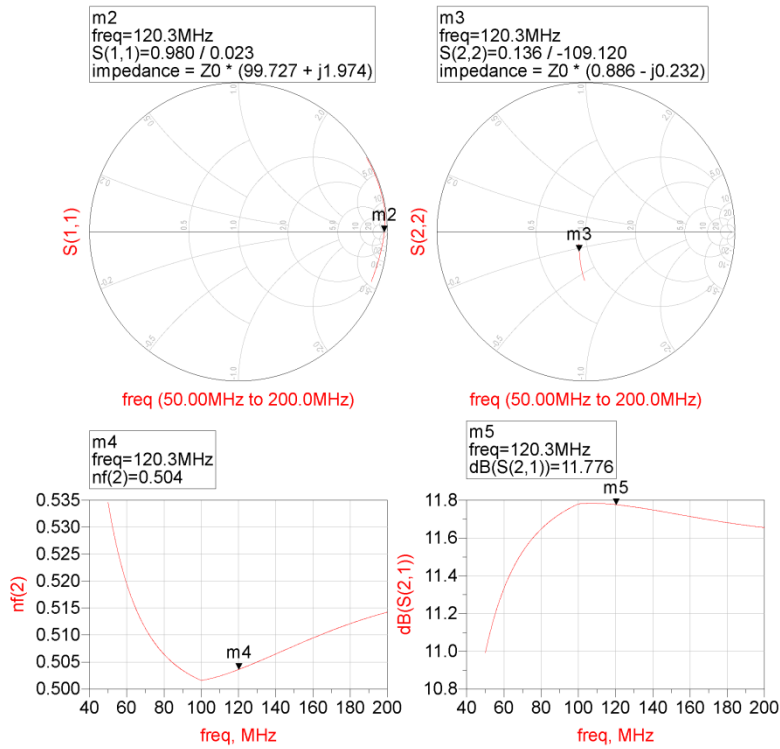


Figure 2.27: Simulation results of the first stage of the preamplifier at 120.3MHz.

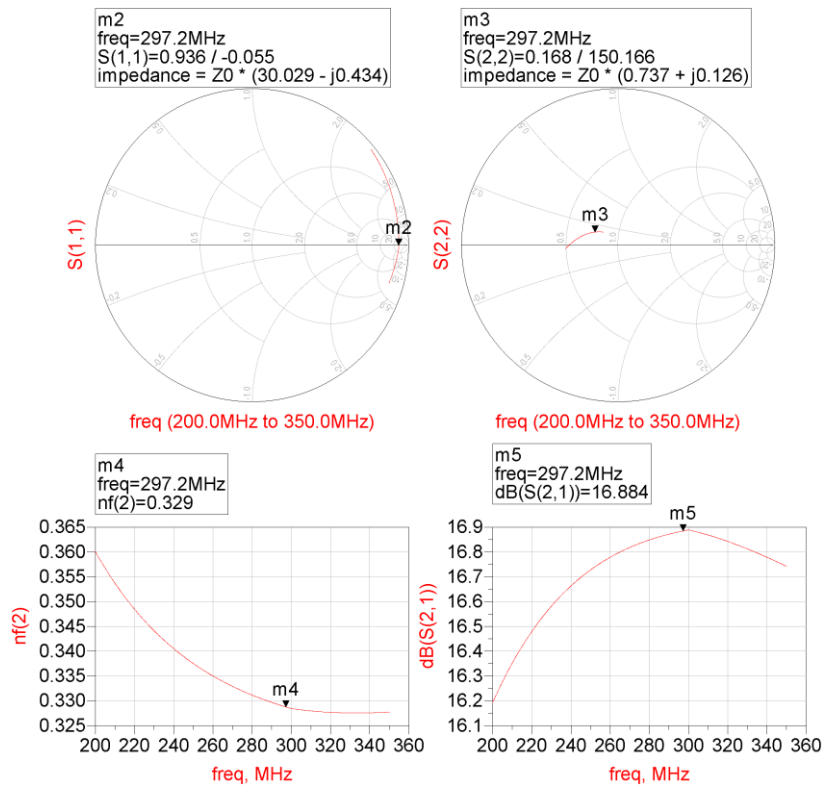


Figure 2.28: Simulation results of the first stage of the preamplifier at 297.2MHz.

The same design procedure was performed for the second stage. The difference is that the input impedance of the second stage was matched to the output impedance of the first stage to realize gain matching. The gain of the second stage was controlled so that an approximate 30dB gain can be achieved by the two-stage preamplifier. Similar to the previous front-end circuits design, the layout of the preamplifier was involved in the ADS Momentum simulation as shown in Figure 2.29.

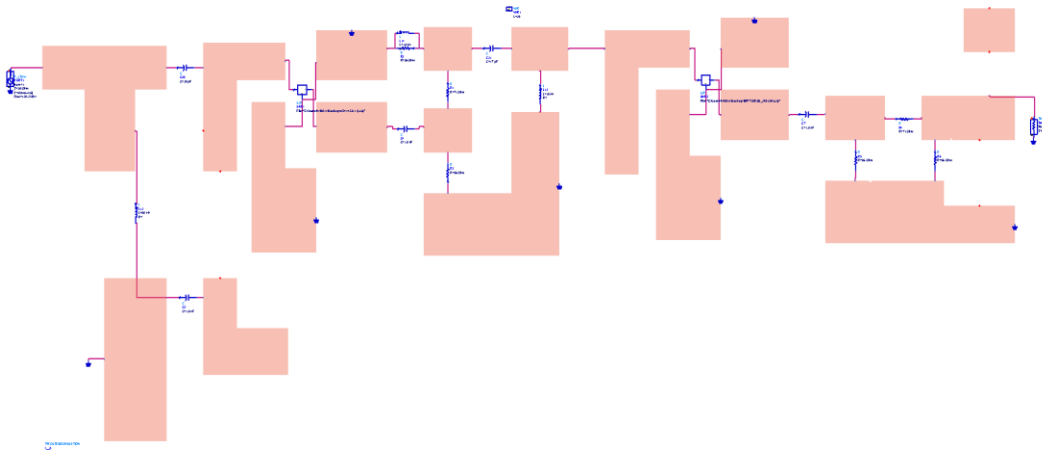


Figure 2.29: Simulation layout of the high input impedance preamplifier in ADS Momentum simulation.

The values of the inductor and capacitor in the input matching network were slightly adjusted so that high input impedances could be obtained. The measured input impedances of the fabricated preamplifiers at both frequencies exceed 800 ohm. The gains of the preamplifier are approximate 30dB and the noise figures are controlled to a low level as shown in Figure 2.32.

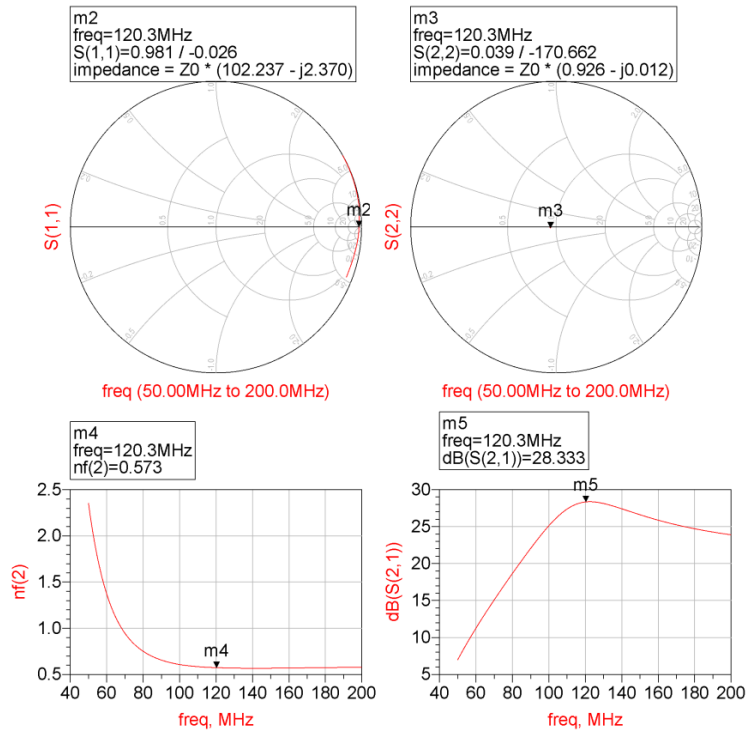


Figure 2.30: Simulation results of the two-stage high input impedance preamplifier at 120.3MHz.

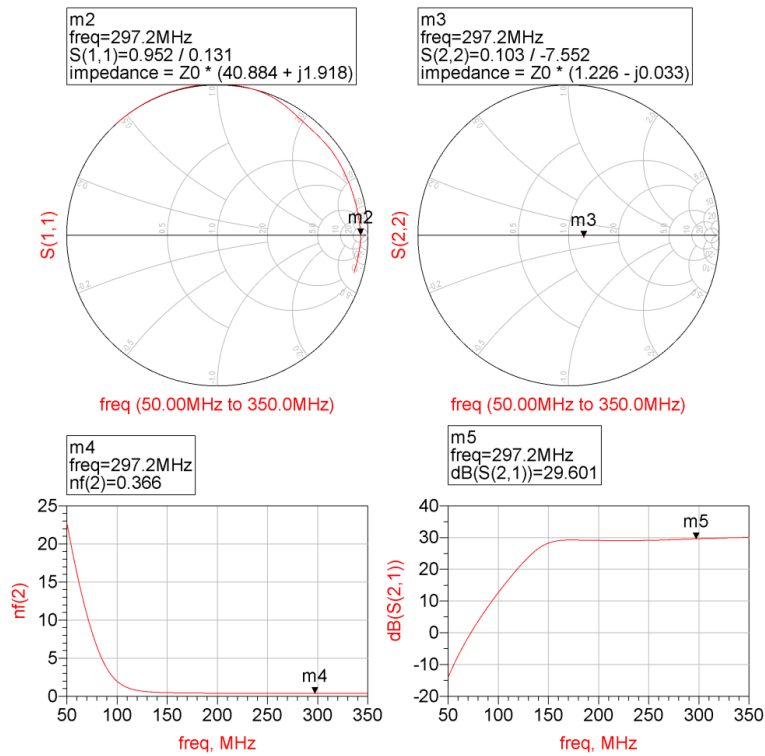


Figure 2.31: Simulation results of the two-stage high input impedance preamplifier at 297.2MHz.

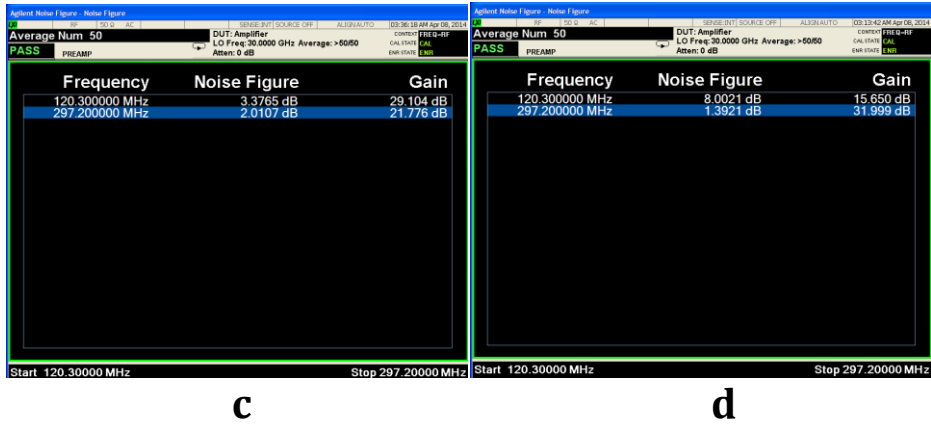
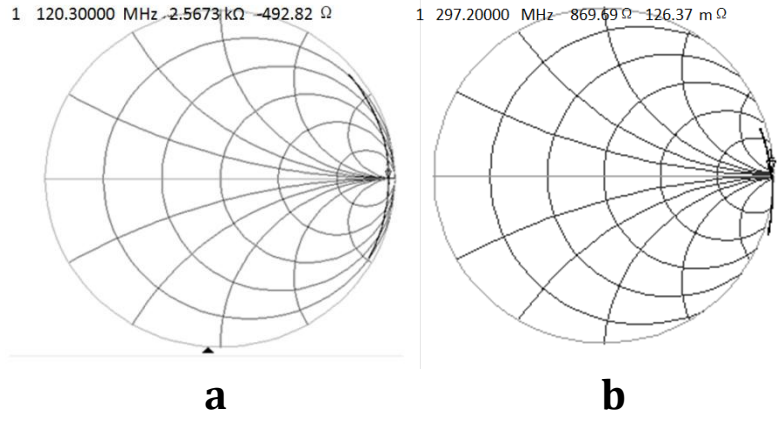


Figure 2.32: Measured input impedance of the preamplifier fabricated at a). 120.3MHz b). 297.2MHz. and measured gain and noise figure at a). 120.3MHz b). 297.2MHz.

3. Parallel-Plate Waveguide for Volume Radio Frequency Transmission in MRI [84]

3.1. Introduction

As mentioned in Chapter 2, the conventional RF coil designed for MR imaging application such as volume coils (birdcage coil, TEM coil) and surface array coils are resonant structures. Optimal transmit efficiency or receive sensitivity can only be achieved by tuning the coil to the specific Larmor frequency [1, 4, 5]. However, the changes in loading to be imaged and the scanning environment may cause the tuning frequency of the RF coil shift from the Larmor frequency. This frequency shift makes RF power input reflect back to the generator due to impedance mismatch [6] and lower the coil's performance. This narrowband feature is typically characterized by the quality factor (Q-factor) [1] and high-Q coils are preferred for their low coil/sample losses. On the other hand, it also indicates the sensitivity of a coil to its operating condition. This problem is especially pronounced in high-field applications, where the design of transmit coils can be a challenging task [7, 8, 9, 10]. From the electromagnetic perspective, high-Q resonators are sufficient but not necessary for effective RF transmission. The use of traveling-wave structures, which are non-resonant, has been studied extensively in antenna engineering [6]. Due to the lack of sharp resonant peaks, broadband antennas require no frequency tuning within its operating bandwidth, and are less sensitive to environment variations and manufacture defects [6]. The use of traveling-wave structures in MRI has been studied by different groups in the past. Brunner et al. [11] demonstrated the feasibility of using the RF shield of an MRI scanner as a waveguide to support

traveling waves. The main waveguide structure does not require reactive components for tuning, and a circularly polarized patch antenna was used for RF excitation and signal reception. This concept was further extended by using dielectric inserts to reduce impedance mismatch between air/tissue boundaries [12, 13]. Zhang et al. [14] performed a thorough comparison of waveguide-based transmitters and the TEM coil via numerical simulations. The investigators found that wave attenuation and reflection from body boundaries caused substantial B_1^+ inhomogeneity; although a high degree of uniformity was achieved inside an empty scanner bore. One of the main features of waveguide-based transmitters is that the scanner bore size needs to be large enough so that the cutoff frequency of the desired mode is below the Larmor frequency [11]. Otherwise, electromagnetic waves are evanescent, not traveling. Because the bore size of regular human scanners is barely large enough to support traveling waves at 7T [11], this type of structure is not suitable for clinical MRI. Tang et al. [15] reported that the TEM mode of a coaxial cable was applied in order to avoid the cutoff frequency issue. However, the requirement of a center conductor makes human imaging difficult. Zhang et al. [16] developed a surface transmitter using the TEM mode supported by two closely spaced conductors; Pan and Zhang later developed a volume transmitter for parallel transmission using an array of such coils [17]. In this study, feasibility of using a different traveling wave structure (i.e., parallel-plate waveguide) for MRI was investigated. A parallel-plate waveguide is a transmission line that consists of two conductors with appropriate terminations that match its wave impedance. Just like coaxial cables, its wave impedance is frequency-independent. The use of transmission lines as broadband antennas can be dated back to the 1930s [18]. This technique enjoyed a long history of success due to its

simplicity and, more importantly, its effectiveness. As will be demonstrated, much of these advantages can be retained in MRI. A transmitter as simple and compact as two actively driven parallel conducting plates can provide broadband RF excitations. It should be noted that the proposed method is fundamentally different from the one proposed by Vazquez et al. [19], which applied a birdcage coil and two floating parallel conductors. By leaving both ends of the floating conductors open-circuited, a narrowband transmission line resonator rather than a broadband waveguide is formed [20].

3.2. Broadband Volume Transmitter Design

The electromagnetic field between two parallel plates can be expressed as the combination of different modes, which are not necessarily uniform except for the TEM mode (Figure 3.1) [20]. To be useful in MRI, non-TEM (or higher-order) modes need to be suppressed. According to electromagnetic theories, higher-order modes can be classified as TE_n^z and TM_n^z modes, where superscript z represents wave propagation direction, which is also the direction of B_0 field (Figure 3.1), and subscript n is the mode index. For TE_n^z modes, there exists a non-zero magnetic field component [20]

$$H_x = (j\omega\varepsilon/k_c)A_n \cos\left(\frac{n\pi y}{d}\right)e^{-j\beta z} \quad (3.1)$$

where A_n is the mode amplitude, d is the distance between the plates, $\beta = \omega\sqrt{\mu\varepsilon}$ is the angular wavenumber, and $k_c = n\pi/d$ is the cutoff wavenumber. By Ampere's law, currents flowing on the two plates are in the same direction (common mode) when n is odd, and in opposite directions (differential mode) when n is even. For TM_n^z modes, there exists a non-zero electric field component

$$E_x = (j\omega\mu/k_c)B_n \sin\left(\frac{n\pi y}{d}\right)e^{-j\beta z} \quad (3.2)$$

where B_n is the mode amplitude. A virtual ground exists in the middle of the two plates only if n is even, which corresponds to differential modes. Thus, both TE_n^Z and TM_n^Z are differential when n is even. Because the TEM mode is differential, in theory only higher order differential modes can be simultaneously excited when the TEM mode is intended. In practice, balanced feeding structures are preferred in order to suppress common modes.

The suppression of higher order modes can be further suppressed by impedance mismatch. For the TEM mode, its frequency-independent wave impedance is

$$Z_{TEM} = \eta \frac{d}{w} \quad (3.3)$$

where $\eta = \sqrt{\mu/\varepsilon}$ is the characteristic impedance and w is the width of the parallel plate. For TM_n^Z mode, its wave impedance is

$$Z_{TM} = \eta \sqrt{1 - \left(\frac{k_c}{k}\right)^2} \quad (3.4)$$

For TE_n^Z mode, its wave impedance is

$$Z_{TE} = \frac{\eta}{\sqrt{1 - \left(\frac{k_c}{k}\right)^2}} \quad (3.5)$$

In both cases, the wave impedances are frequency-dependent. If the distance-to-width ratio is close to unity, the wave impedances of both TE_n^Z and TM_n^Z modes will be substantially different from that of the TEM mode. For an impedance matching network designed to match cable impedance to that of the TEM mode, higher-order modes are rejected due to impedance mismatch.

Equation (2.3) further indicates that the TEM mode is broadband in nature since it does not have a size-related cutoff or resonant frequency. Its impedance is determined by the dielectric property of the medium between the plates and the distance-to-width ratio, not the actual size. Thus, the effect of loading to the wave impedance can be approximated by using an effective permittivity [20]. Because the human body does not have a regular shape, numerical simulations can be used for more accurate prediction of the wave impedance.

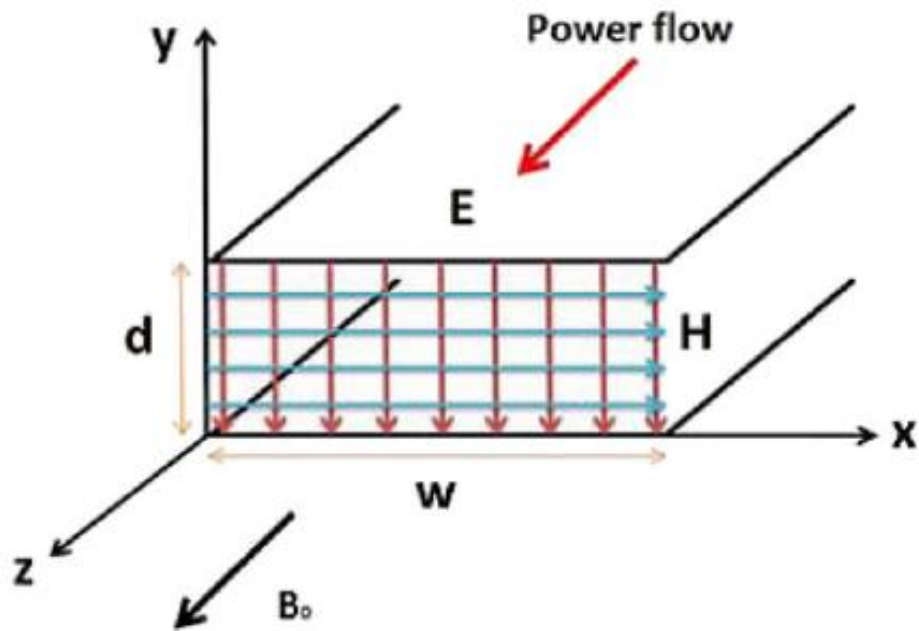


Figure 3.1: Electromagnetic field distribution of the TEM mode of a parallel-plate waveguide.

3.3. Numerical Simulation

To achieve optimal transmit efficiency (minimize reflection coefficient), the parallel plate waveguide and its impedance matching tapered transmission lines were modeled in EM simulation platform of FEKO (EMSS S.A. Pty Ltd, Stellenbosch, South Africa) as shown in Figure 3.2 for numerical simulations. The width and length of the waveguide were 7cm and 20cm respectively. A cylinder with diameter of 9.2 cm filled with dielectric (permeability=56, conductivity=0.657) was used as phantom to mimic the loading of the human forearm. The load impedances at all four ports were set as identical and optimized through simulation. Figure 3.3 shows the curve of the load impedance versus reflection coefficient. Best transmit efficiency of the parallel plate waveguide could be achieved when the load impedance equals to 210 ohm.



Figure 3.2: Simulation model for linear PPW coil.

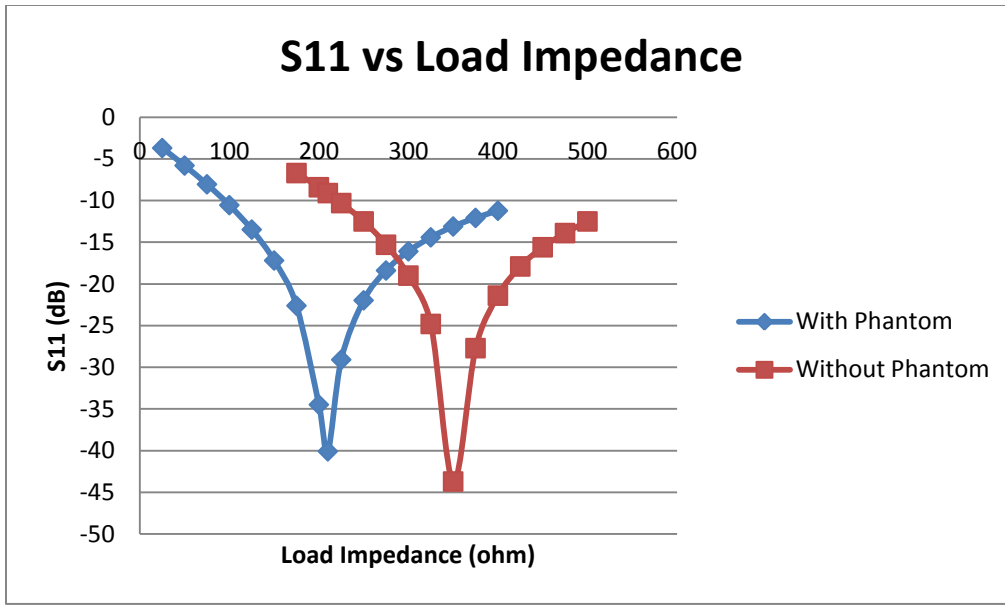


Figure 3.3: The optimization results of reflection coefficient versus the input impedance for the PPW coil with and without phantom loading.

Obtained the optimal characteristic impedance of the parallel plate waveguide, the reflection coefficient was simulated over a wide frequency band to prove the broadband functionality of the PPW coil. As shown in Figure 3.4, the S11 simulated from 50 to 350 MHz was below -10 dB which is a reasonable value for transmitting without severe power reflection.

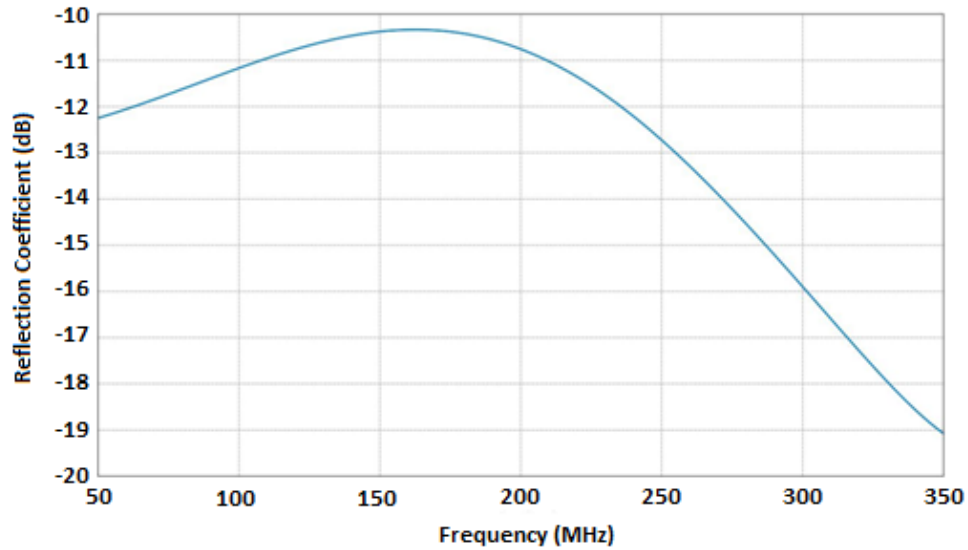
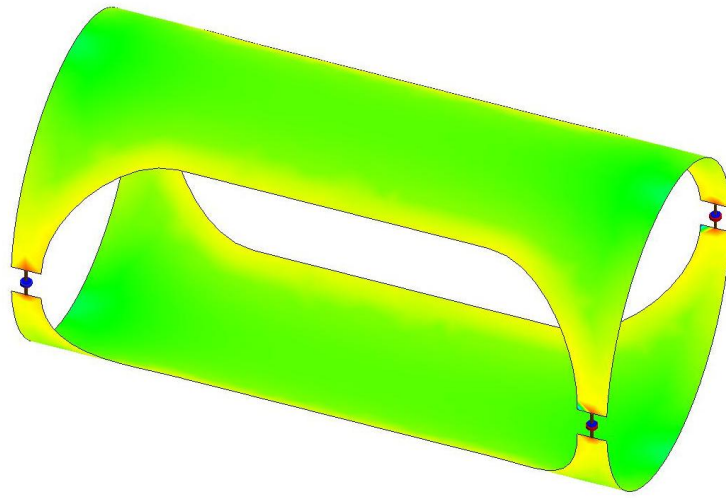
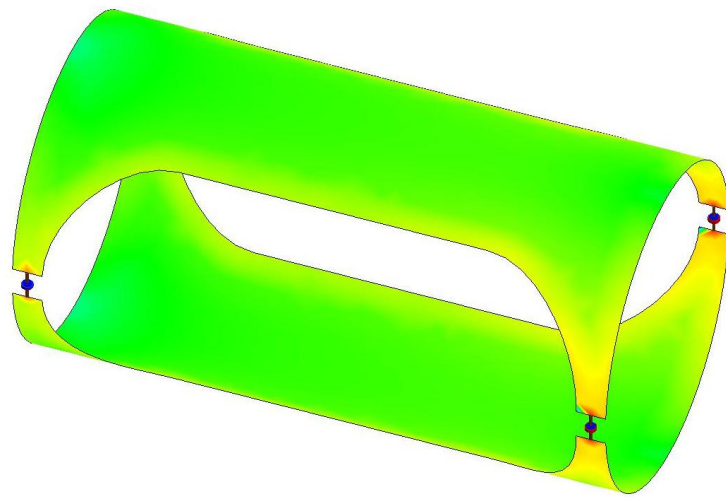


Figure 3.4: Simulated reflection coefficient of the PPW coil over the frequency band from 50MHz to 350MHz.

At two frequencies of interest 120.3MHz and 297.2 MHz, the current distributions and H-field distributions in sagittal plane within the cylinder phantom were simulated as shown in Figure 3.5 and Figure 3.6. At higher frequency (297.2MHz), the nonuniformity of the magnetic field was observed due to that the dielectric resonance effect is getting worse (Figure 3.6 b).).

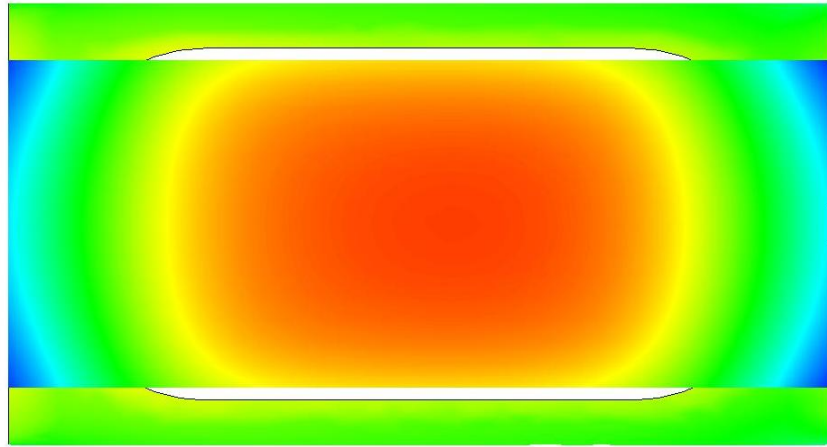


a

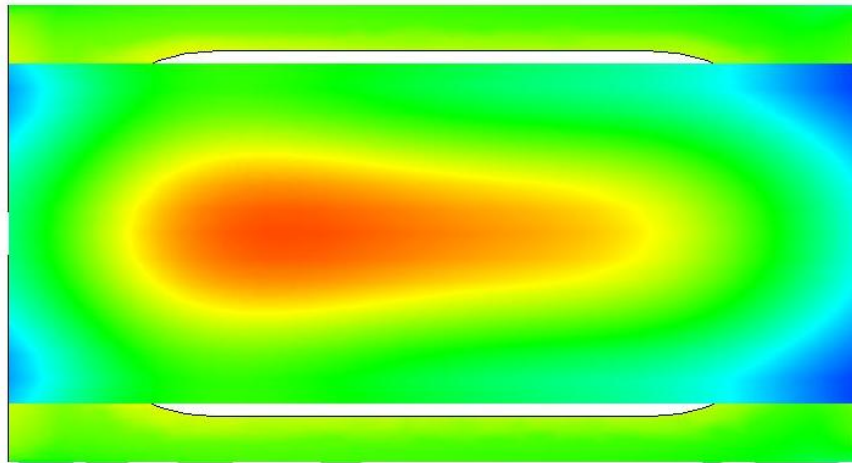


b

Figure 3.5: Simulated current distribution on the PPW coil at a).120.3MHz and b).297.2 MHz.



a



b

Figure 3.6: Simulated electromagnetic field of the PPW coil in sagittal plane at a). 120.3MHz and

b). 297.2MHz.

3.4. Transmit Coil Fabrication

3.4.1. Transmit Coil Matching

A coil suitable for imaging the human forearm was constructed in the above manner. Copper foils (3M, Saint Paul, Minnesota, USA) 7 cm wide and 20 cm long were laid on the outside of an acrylic tube (McMaster-Carr, Elmhurst, Illinois, USA) with a 10.8-cm outer diameter. The corresponding distance-to-width ratio of the parallel-plate waveguide was 1.54. Each copper foil was split at the ends and tapered down to form a 1-cm gap as shown in Figure 3.7. The entire coil structure does not have any reactive components for tuning.



Figure 3.7: Prototype parallel-plate waveguide. The balanced Chebyshev impedance matching circuits are mounted across the gaps.

To match the PPW coil input impedance to 50-ohm characteristic impedance over a wide frequency band from 100MHz to 300MHz, a broadband matching network with Chebyshev frequency response was designed, fabricated and connected across each gap of the built PPW coil. It was implemented symmetrically for common-mode suppression (Figure 3.9). The matching network was designed using ADS broadband matching design toolbox and optimized based on reflection coefficient.

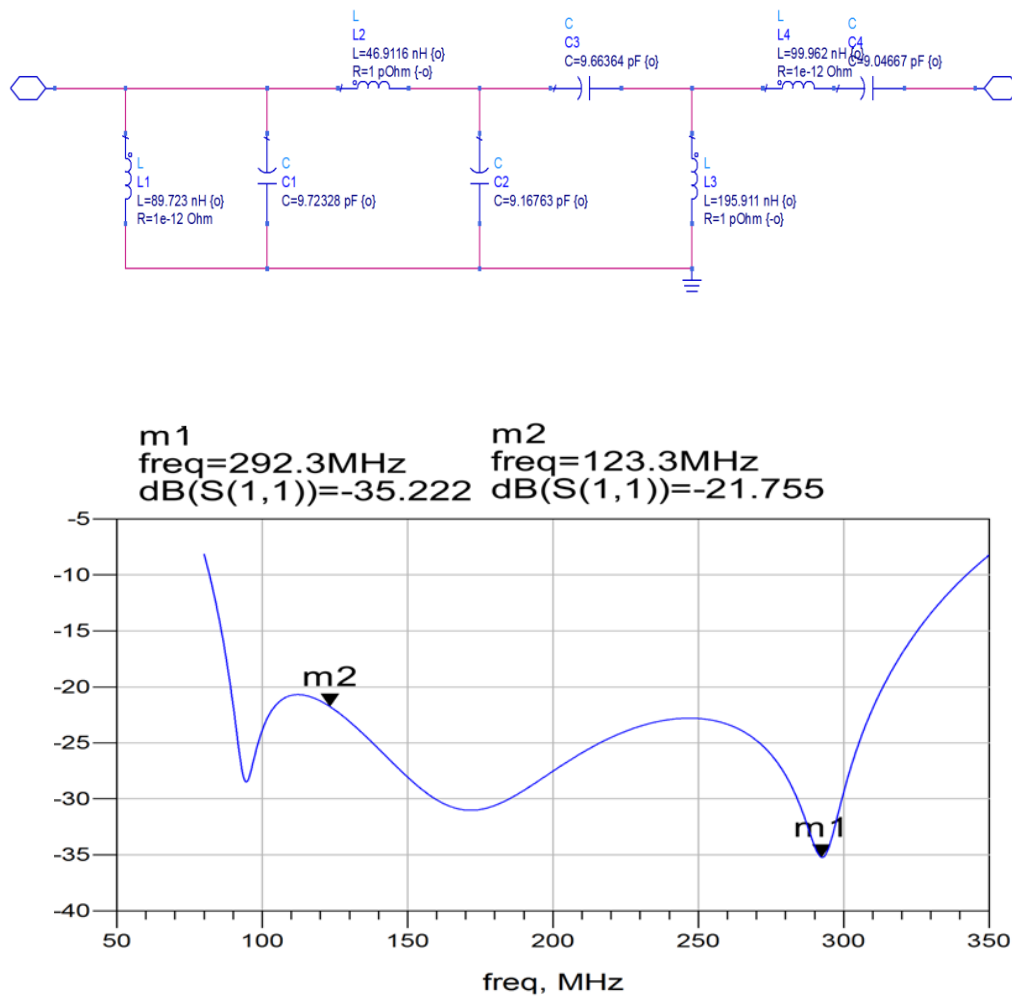


Figure 3.8: Simulation schematic and result of the broadband matching network with Chebyshev frequency response.

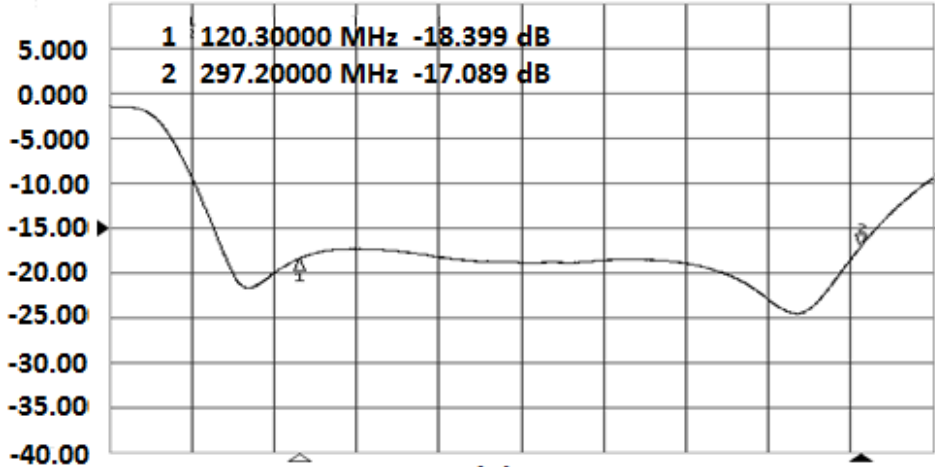
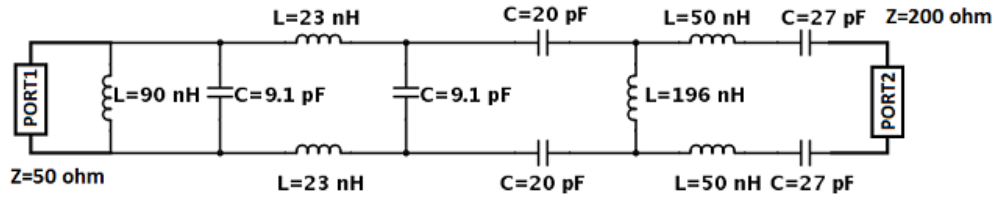


Figure 3.9: Schematic of the balanced broadband matching network and measured reflection coefficient at 120.3MHz and 297.2MHz.

With the PPW coil matched to 50-ohm in wideband, a broadband Wilkinson power divider described in the front-end circuit section was applied to one end of the PPW coil to split the RF input equally and in-phase. Its outputs were connected to the Chebyshev matching networks. At the other end of the waveguide, a broadband Wilkinson power combiner was used to combine the RF energy flowing out of the waveguide and feed it back to the input by using a third Wilkinson power combiner to form a re-entrant scheme.

To determine the system loss which includes coil loss, phantom loss, and loss in the matching circuits and Wilkinson power divider/combiner, the total insertion loss over the frequency band from 100 MHz to 320 MHz was measured using following coil setting-up as shown in Figure 3.10. According to the measurement results, the total loss of the coil and broadband Wilkinson power divider/combiner was -1.63 dB and -7.17 dB at 120.3MHz and 297.2MHz respectively. These insertion losses will be used for calculating the loss of the RF front-end circuits in the following section.

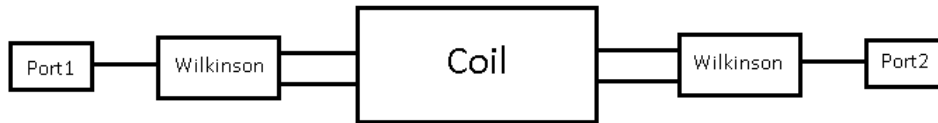


Figure 3.10: Schematic representation of the reflection and insertion loss measurement of the PPW coil. When the reflection coefficient was measured, port 2 was terminated with 50 ohm and port was connected to network analyzer.

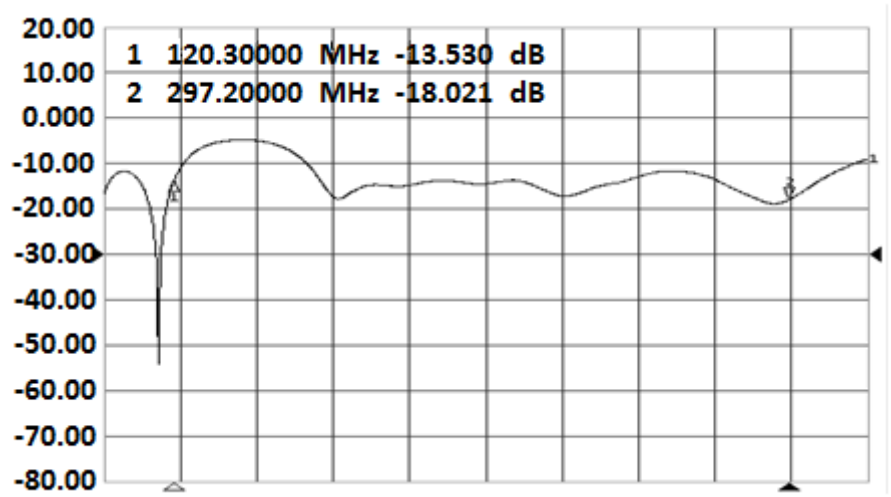


Figure 3.11: Measured reflection coefficient of the PPW coil with broadband matching networks and Wilkinson power divider/combiner connected.

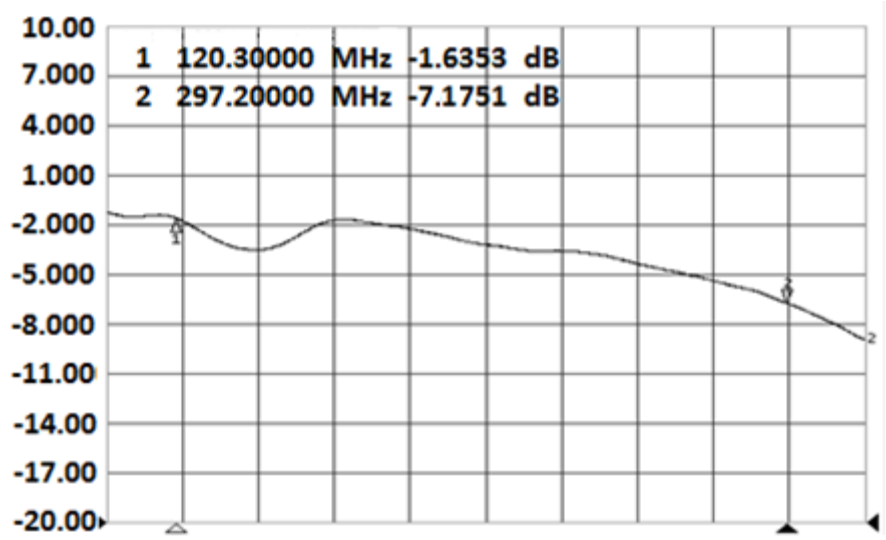


Figure 3.12: Measured insertion loss of the PPW coil with broadband matching networks and Wilkinson power divider/combiner connected.

3.4.2. Front-end Circuits

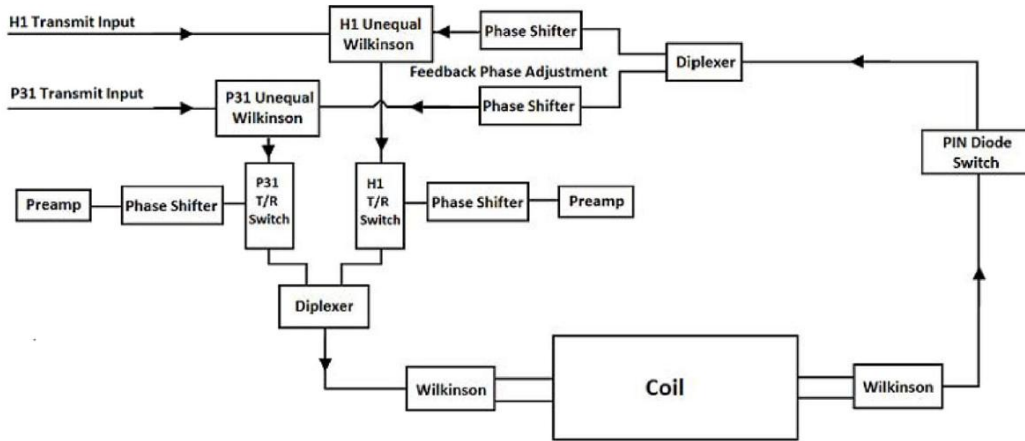


Figure 3.13: Schematic of the front-end circuits of the linear PPW coil.

Incorporated with the parallel plate waveguide coil, radio frequency front-end circuits were designed and fabricated for both proton (1H) and phosphorous (31P) respectively. Broadband Wilkinson power divider and combiner were positioned at both feeding and terminating points of the PPW coil. T/R switches controlled by the PIN diode signal obtained from the scanner system were employed to realize reliable switching between transmit and receive. The isolation between transmit and receive was carefully tuned to protect preamplifier from high transmit power. At transmit side, due to the attenuation of the PPW at different frequency, Wilkinson power dividers with different power ratio discussed in Chapter 2 were used to combine the input power with the re-entrant power to prevent power dissipation on the isolation resistors of the Wilkinson power dividers. Phase shifters were inserted into the transmit path to make the re-entrant power is in-phase with input power so that the maximum transmit efficiency could be achieved. To combine 1H and 31P signals, diplexers with low attenuation and good

isolation were designed by taking advantage of band-stop filters. At receive side, phase shifters were used to adjust the total phase delay of the receive path in order to make the parallel plate waveguide work as open ended resonator, and the signal generated was detected by the high-input impedance low noise preamplifier designed specifically at 120.3 MHz and 297.2 MHz .

The design of all front-end circuit was facilitated by using ADS as discussed in Chapter 2. All capacitors were from the ATC-100B series (American Technical Ceramics, Huntington Station, New York, USA). The inductance was implemented by 164-series and 165-series tunable inductors (Coilcraft, Cary, Illinois, USA). Two types of PIN diode, i.e., UM9415B (Microsemi, Aliso Viejo, California, USA) and MA4P7470-1072T (M/A-COM, Lowell, Massachusetts, USA), were applied for transmit/receive (T/R) switches. Bench measurements were performed by using an Agilent E-5061A network analyzer (Agilent Technologies). A 1.25-L phantom, which was a 20-cm-high and 8-cm-wide bottle filled with 55 mM NaCl and 100 mL phosphate, was prepared for bench measurement and phantom imaging.

3.4.3. Power Re-entrant

If the parallel plate waveguide is simply terminated with a load resistance which matched to the characteristic impedance of the waveguide, half of the input power will be dissipated on the load. To improve the transmit efficiency, a feedback system firstly proposed for travelling wave antenna was employed in the parallel plate waveguide design [30]. In this feedback system, the power dissipated on the load is re-circulated back to the system input terminal with a transmission line with an electrical length which

guarantees the re-enter power is in phase with the system input as shown in the front-end schematic (Figure 3.13). To make sure that the re-enter power and input power were in phase and optimal transmit efficiency was achieved, following measurements on bench top were performed.

3.4.4. Transmit Coil Bench-testing

During the bench top testing procedure of the PPW coil, the total phase delays of the power re-entrant path at both frequencies for 1H and 31P was measured. To guarantee that the feed-back power is in phase with the input power, the phase delay should be adjusted to an integer number of 360 degree. Also, in order to compare the intrinsic transmit efficiency of the PPW coil designed with that of the Birdcage coil with the same dimensions, the additional power loss brought in by the front-end circuit of the PPW coil aforementioned need to be measured and calibrated during the later transmit efficiency calculation. Therefore, in the bench-testing, the power loss of the front-end circuits includes T/R switch, unequal Wilkinson power divider and diplexers were calculated through subtracting the total insertion loss measured by the power loss of the PPW coil measured in section 3.4.1. The schematic presentation of the PPW coil bench testing setting-up at 297.2MHz is shown in Figure 3.14. The port for feed-back power connection was terminated by 50 ohm load during the measurements.

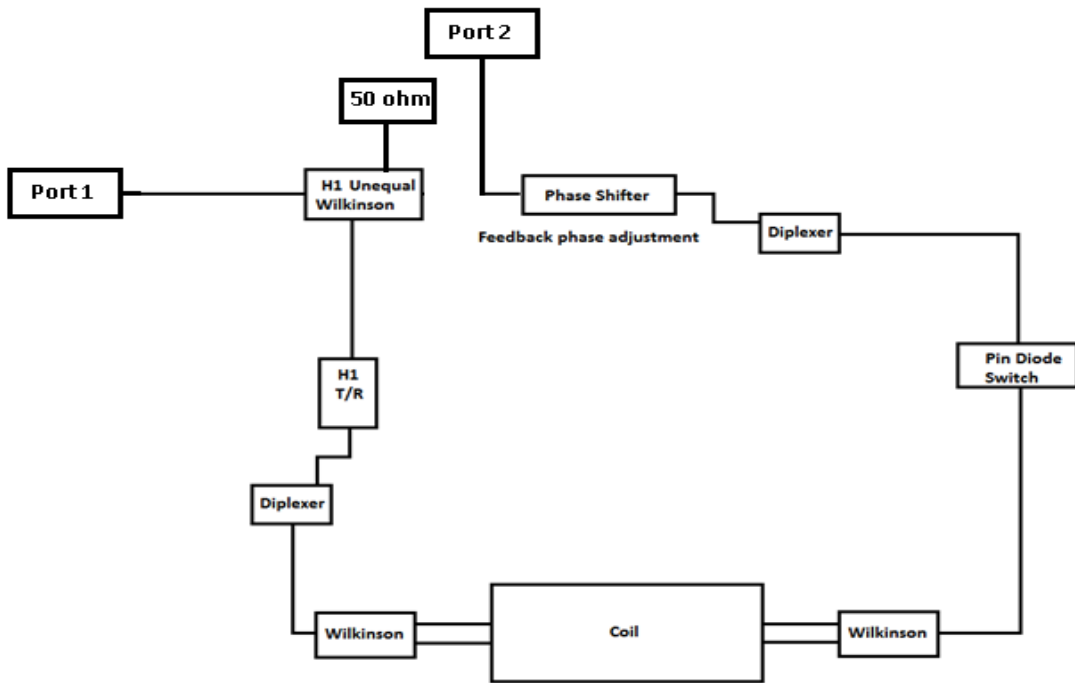


Figure 3.14: Bench-testing setting-up for the re-entrant power phase compensation and total insertion loss measurement for 1H transmit channel.

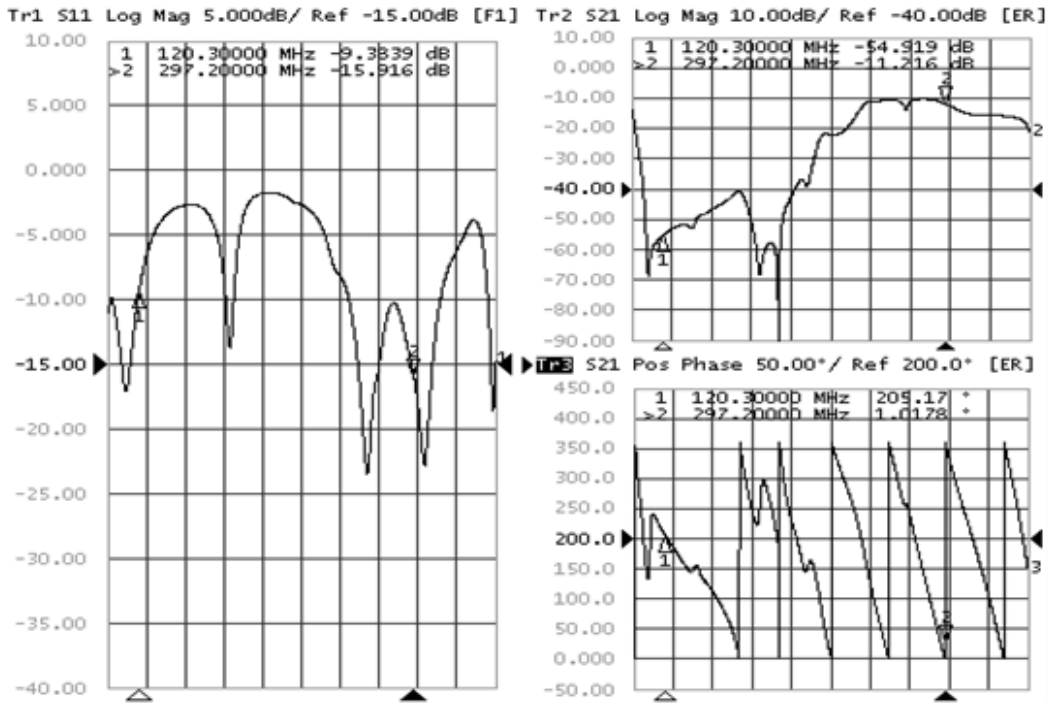


Figure 3.15: Measured phase delay of the re-entrant power path and total insertion loss which includes PPW coil and front-end circuits of 1H transmit channel.

As shown in Figure 3.15, the phase delay of the re-entrant power path was measured as -359 degree and the insertion loss of the 1H front-end circuits can be calculated as

$$\begin{aligned}
 IL_{Front-end} &= IL_{Total} - IL_{Coil} - \text{Power Ratio of Wilkinson} \\
 &= -11.22 \text{ dB} - (-7.18 \text{ dB}) - (-1.04 \text{ dB}) = -3.0 \text{ dB}
 \end{aligned}$$

Same measurement procedure was repeated for the 31P channel (120.3MHz), the measurement schematic and results are shown in Figure 3.16 and Figure 3.17.

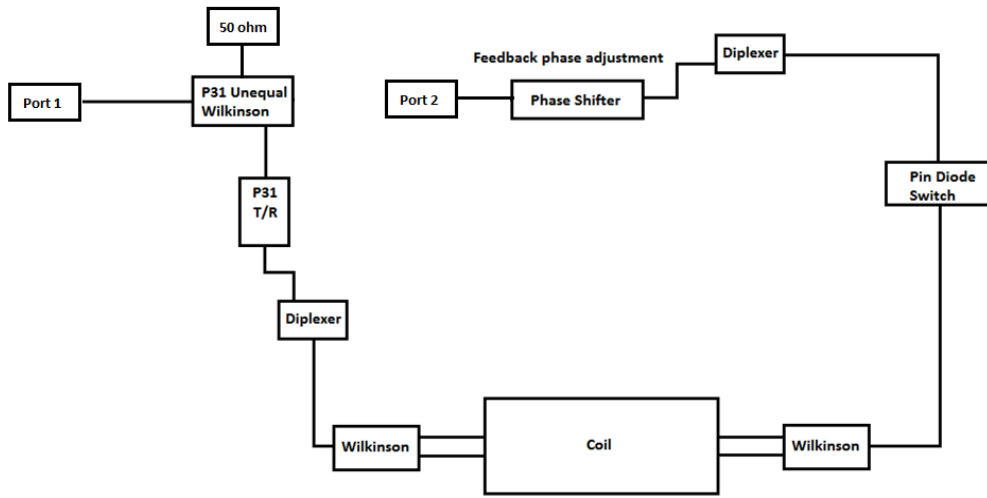


Figure 3.16: Bench-testing setting-up for the re-entrant power phase compensation and total insertion loss measurement for 31P transmit channel.

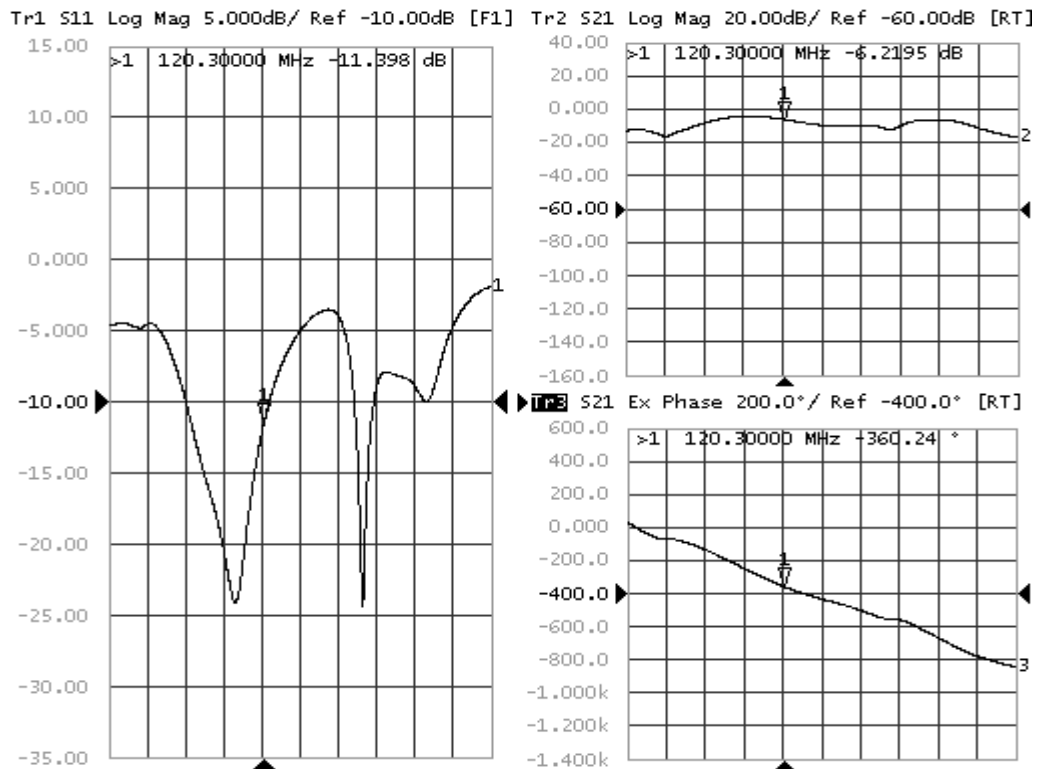
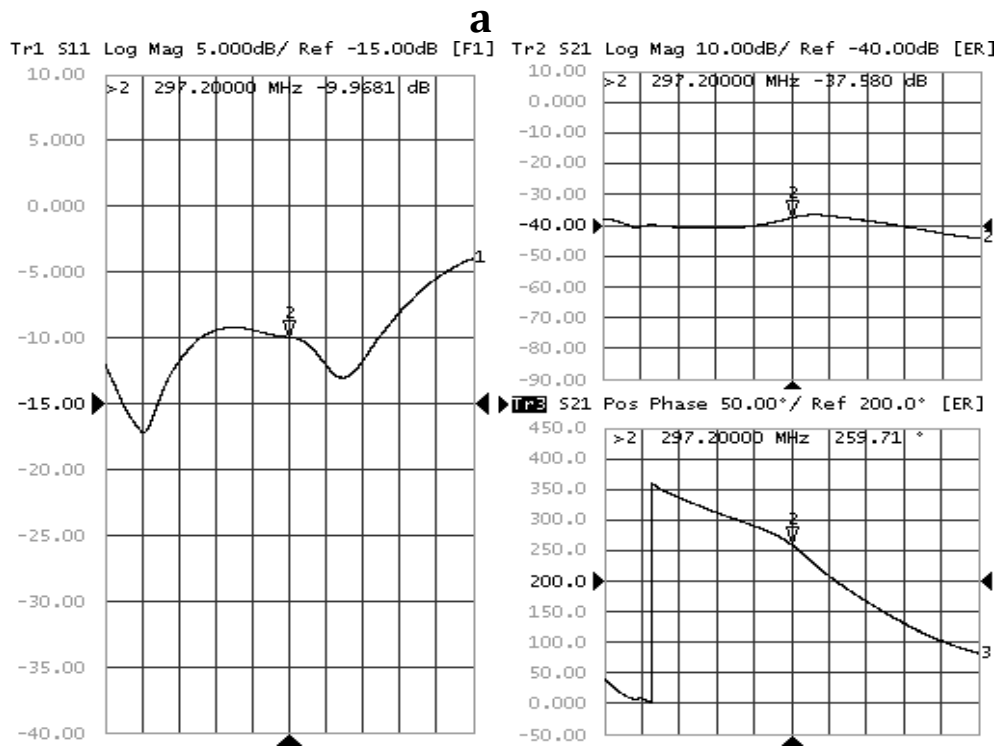
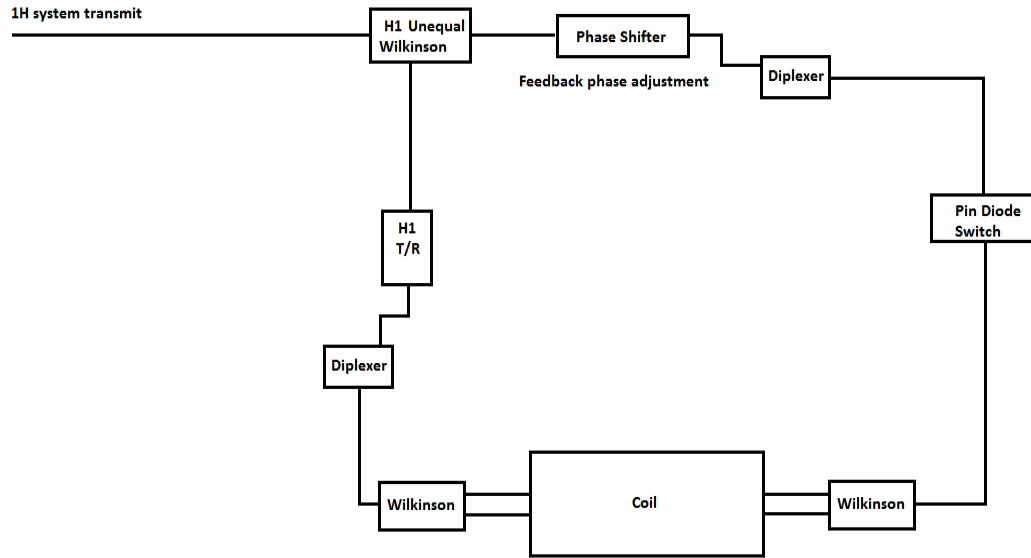


Figure 3.17: Measured phase delay of the re-entrant power path and total insertion loss which includes PPW coil and front-end circuits of 31P transmit channel.

The phase delay of the re-entrant power path was measured as -360 degree and the insertion loss of the 31P front-end circuits can be calculated as

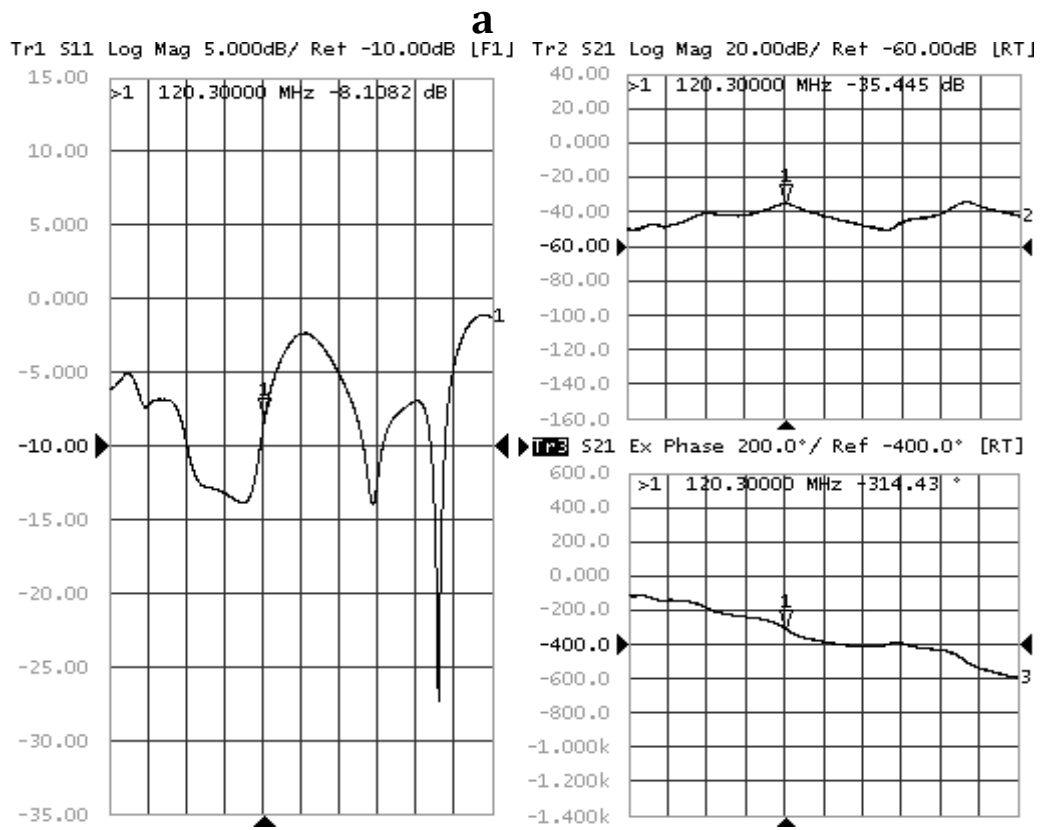
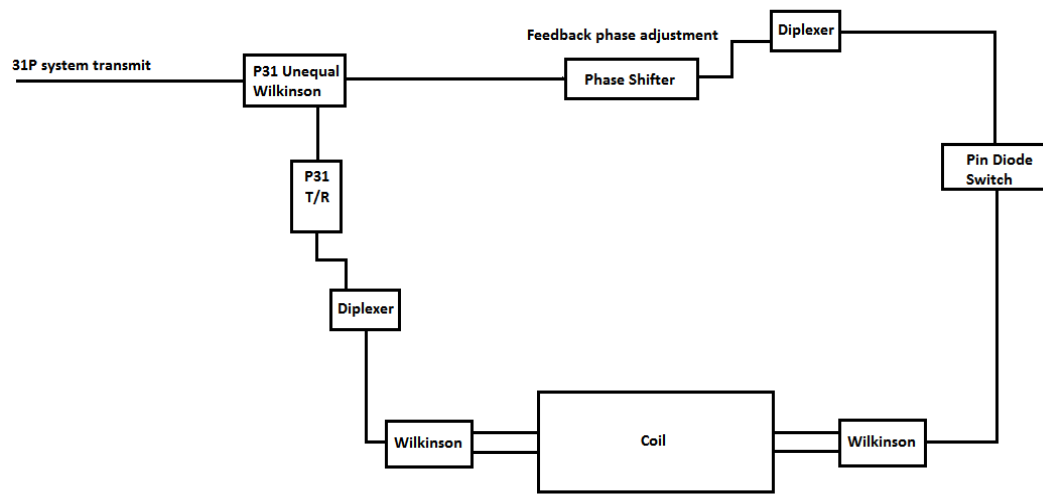
$$\begin{aligned} IL_{Front-end} &= IL_{Total} - IL_{Coil} - \text{Power Ratio of Wilkinson} \\ &= -6.22 \text{ dB} - 1.63 \text{ dB} - 2.2 \text{ dB} = -2.39 \text{ dB} \end{aligned}$$

Then the feed-back power was connected to the unequal Wilkinson power combiners at both frequencies with compensated phase delay. To prevent B1 field inhomogeneity and signal drop-off caused by the coil fabrication defects. The PPW coil was connected to the front-end circuits fabricated and the electromagnetic field distribution within the PPW coil was detected using a single probe. Due to the nature of the TEM wave, the magnetic field generated was uniform and no abrupt change in probe picked-up signal was observed at both working frequencies. Also because of that the feed-back path was only compensated to in phase with input power at single frequency to optimize the transmit efficiency, a local signal peak was observed at the target frequency as shown in Figure 3.18 and Figure 3.19 which proves that the power feed-backs were connected correctly.



b

Figure 3.18: a) Bench-testing setting-up for the transmit field homogeneity verification for 1H transmit channel. b) Signal detected by single probe.



b

Figure 3.19: a) Bench-testing setting-up for the transmit field homogeneity verification for 31P transmit channel. b) Signal detected by single probe.

3.4.5. Receiver Design

Signal reception follows the principle of open-circuited transmission-line resonator [20]. It is preferred to sense the induced voltage rather than the current for better signal-to-noise ratio (SNR) [26]. This was achieved by adjusting the total electrical length of an open-circuited transmission line to be equal to multiples of half wavelength, and connecting one end of the open-circuited waveguide to a low-noise preamplifier (LNA) with a high input impedance [26]. In Figure 3.11, the rightmost PIN diode is switched off during signal reception, which creates one open end of the transmission line. At each frequency, the phase measured between the PIN diode and the input of the LNA through the Wilkinson power dividers/combiners, the parallel-plate waveguide, the diplexers, and the T/R switches were adjusted to be equal to multiples of 180 degree. The high-impedance LNAs were implemented by using an ATF-54143 for the first stage and a BFP-720 for the second stage at 120.3 and 297.2 MHz, respectively as discussed in Chapter 2.

3.5. MRI Measurements

3.5.1. ^1H Images and ^{31}P Spectroscopy

7T MRI scans were performed on a Siemens MAGNETOM scanner (Siemens Medical Systems, Erlangen, Germany) at Auburn University. A proton B_1^+ map in the saline phantom was firstly acquired by using Siemens' product sequence based on the double-angle method. The scan parameters were as follows: pulse repetition time $TR = 1000\text{ ms}$; echo time $TE = 14\text{ ms}$; field of view $FOV = 300 \times 300\text{ mm}$; and $matrix\ size = 256 \times 256$. The turbo spin echo (TSE) image of the same phantom (Figure 3.21) was also acquired using the following parameters: $TR = 3600\text{ ms}$; $TE = 87\text{ ms}$; $FOV = 179 \times 199\text{ mm}$; $matrix\ size = 362 \times 448$; and one average.

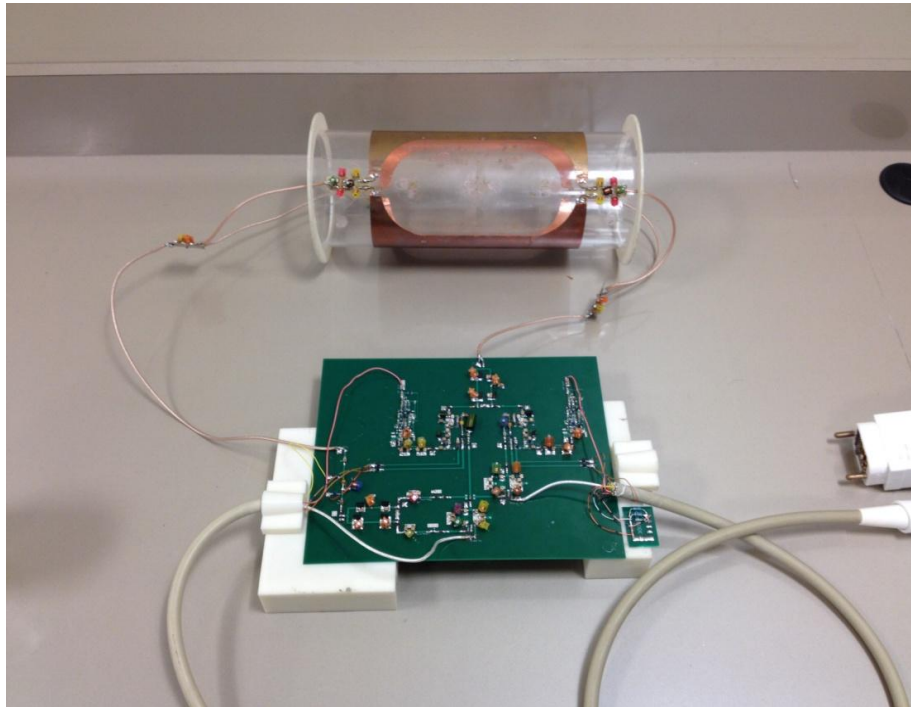


Figure 3.20: PPW coil connected with front-end circuit board for imaging experiments.

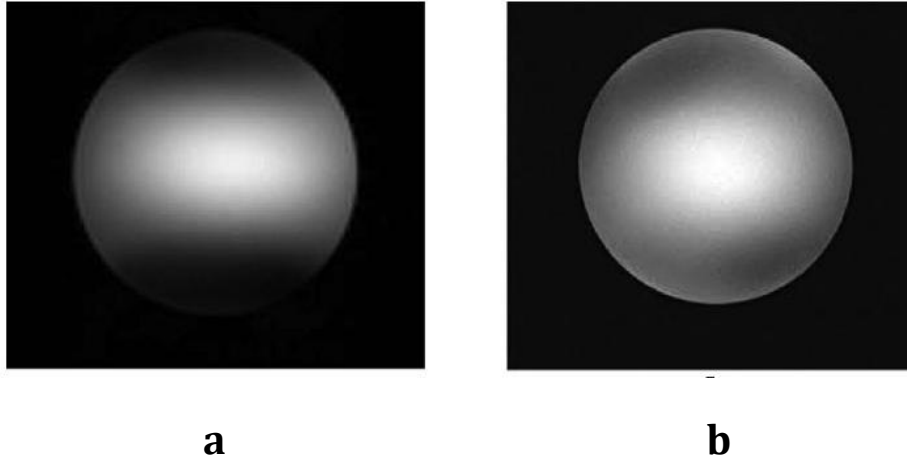


Figure 3.21: a). Measured B_1^+ map and b). TSE image of the phantom in transverse plane.

The TSE image of the human forearm was acquired by using the same parameters but a slightly shorter 83-ms TE. For comparison, the gradient echo (GRE) image of the forearm was acquired (Figure 3.23) using the following parameters: $TR = 8.6\text{ ms}$; $TE = 3\text{ ms}$; $FOV = 250 \times 250\text{ mm}$; $matrix\ size = 512 \times 512$; and one average.



Figure 3.22: Scanning experiments setting-up for human forearm imaging.

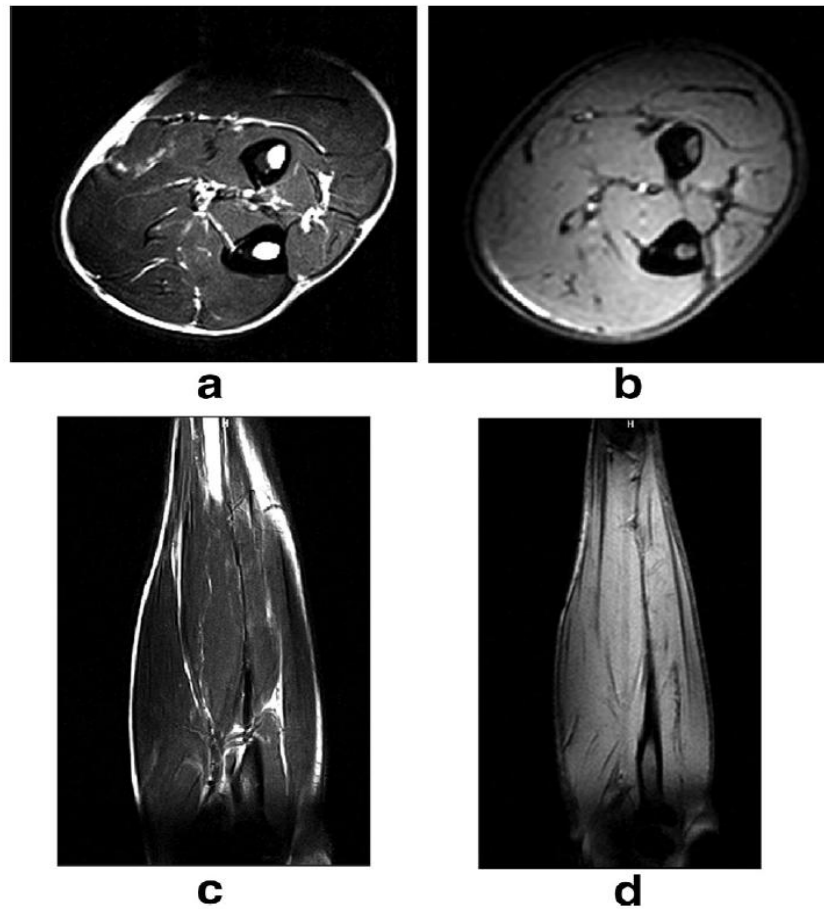
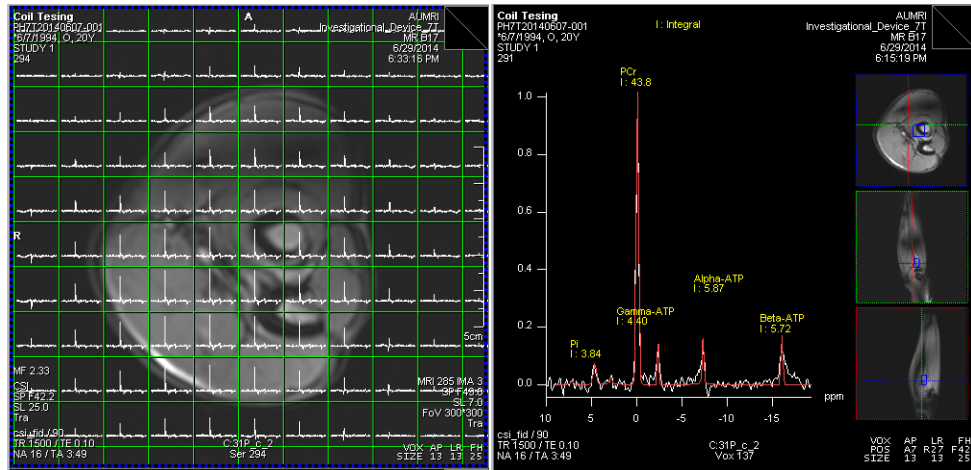
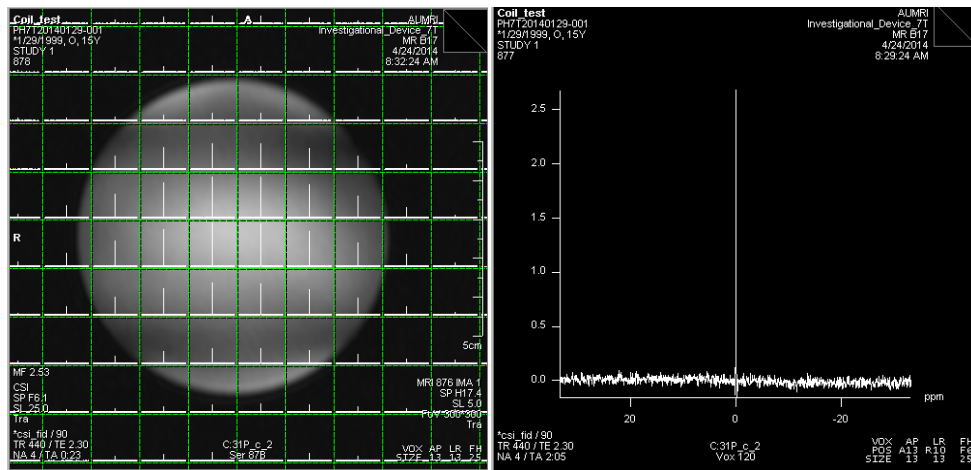


Figure 3.23: TSE (a, c) and GRE (b, d) images of the forearm measured at 7T.

Phosphorous spectroscopy of both buffer solution and human forearm were obtained using a Siemens' product chemical shift imaging (CSI) sequence. The scan parameters were as follows: $TR = 1500\text{ ms}$; $TE = 0.1\text{ ms}$; $bandwidth = 5\text{ kHz}$; $cubic\ volume\ size = 25\text{ mm}$; and 16 averages. The metabolite PCr, γ -ATP and β -ATP were detected in each voxel of the CSI sequence grid measured on forearm as shown in Figure 3.24 a).



a

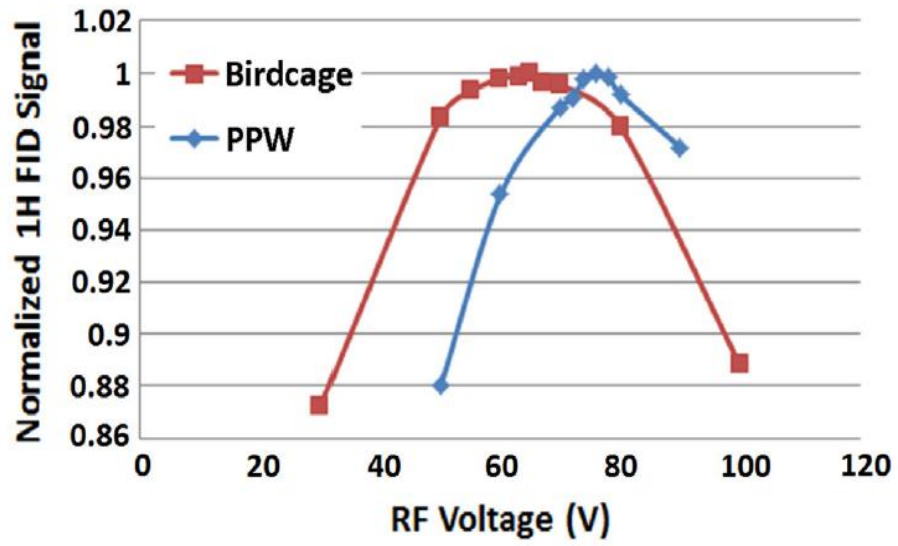


b

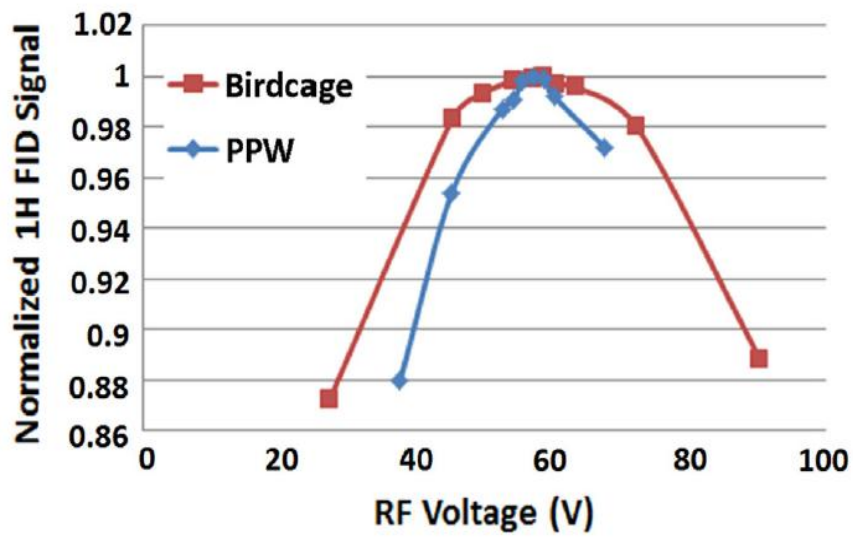
Figure 3.24: P31 spectroscopy obtained using CSI sequence on a). Human forearm and b). phantom.

3.5.2. Transmit Efficiency Comparison with Birdcage Coil

For transmit efficiency comparison purposes, an eight-rung unshielded linear high-pass birdcage coil was constructed by taping a 3/8-inch-wide copper foil on an acrylic cylinder with a 10.8-cm outer diameter, which was the same as the parallel-plate waveguide. The length of the birdcage was also the same as the parallel-plate waveguide. It was tuned and matched to 297.2 MHz with the saline phantom by using 2.3 pF capacitors. The proton transmit efficiency was measured with the 1.25-L phantom by using a free induction decay sequence with a 1-ms rectangular pulse, 1500-ms TR, and 1.1-ms TE. The RF power was increased incrementally until maximum signal intensity was detected. The finest voltage resolution was 2 V (peak RF voltage reading from scanner). The same procedure was repeated for the unshielded linear birdcage coil with a dedicated proton interface box that consists of a T/R switch and a low-impedance LNA. The measured proton transmit efficiency is shown in Figure 3.25 a). Maximum signal intensity was observed with a peak RF voltage of 76 V and 65 V (scanner reading) for the parallel-plate waveguide and birdcage coil, respectively. Considering the loss of the front-end circuit and coil mismatch, the maximum signal appeared at 57 V for both coils (Figure 3.25 b)).



a



b

Figure 3.25: Directly measured (a) and calibrated (b) transmit efficiency of the PPW and birdcage coil loaded with the saline water phantom.

3.6. Conclusion

In this study parallel-plate waveguide for broadband MRI was introduced. Its design principle and hardware implementation were discussed. 7T proton images and 31P CSI results acquired using the same coil demonstrate its feasibility. Compared with resonant coils, the proposed coil is broadband in nature and relatively easier to construct. No reactive components are required for tuning. As a result, its performance is more stable with respect to loading conditions.

4. Quadrature Parallel-Plate Waveguide for Larger Volume Transmission in MRI

4.1. Introduction

The biggest disadvantage of the traditional RF transmitting coils for MRI application is their narrow frequency band which makes the transmit coil need to be re-tuned carefully for different loadings so that optimal transmit efficiency can be achieved which is time-consuming and impractical. To prevent this tedious tuning procedure, a broadband transmission structure can be employed. In the previous section, a parallel plate waveguide (PPW) was used to generate a volume transmission for MRI with low sensitivity to loading change and homogenous magnetic field generation [84]. Using the PPW structure for volume transmission has following advantages. First, since the TEM characteristic impedance of the waveguide is only a function of its distance to width ratio and the relative permeability of the substrate filled and frequency independent [20], the PPW transmit coil is insensitive to the different loading unless the filling factor and loading material changed dramatically. Secondly, due to the nature of the TEM wave generated within the PPW, a homogeneous magnetic field can be obtained which is ideal for MRI volume transmission. Also, the broadband feature of the PPW can be employed for multi-nuclei excitation. The feasibility of using same PPW transmit coil for acquiring both proton image and P31 spectrum signal has been demonstrated in Chapter 3.

However, the dimensions of the aforementioned PPW transmit coil cannot meet the requirements of some large volume MRI study which targets at human brain, leg or torso [12, 14, 17]. Therefore, in this chapter the possibility of using PPW for larger

volume transmission which has a wider MRI application range is investigated. However, the large size of the waveguide employed will lead to much higher power dissipation on waveguide structure and radiation into free space which will result in lower transmit efficiency. To compensate for the power loss due to the increase in coil size, a quadrature structure with two sets of PPW positioned in perpendicular was employed to improve the transmit efficiency. Incorporated with the transmit coil, a four-channel clover shape coil array was designed and fabricated for receiving purpose. Both linear and quadrature structures were measured and the results were compared to demonstrate the increase in transmit efficiency at 3T scanner platform.

4.2. Numerical Simulation

Similar to traditional MRI RF coils, when one puts two sets of PPW coils in close proximity, both magnetic and capacitive coupling between them need to be taken into consideration during the coil design and fabrication process to avoid performance deterioration. According to the theory of the PPW, if TEM waves were generated, the magnetic field within two sets of PPW are perpendicular to each other as shown in Figure 4.1 in which H fields generated by two PPWs are illustrated. In this manner, the magnetic coupling between two PPW coils is much less than that of some conventional RF coils such as Birdcage coil and surface array coil, so that no specific magnetic decoupling method needs to be applied during the coil modeling.

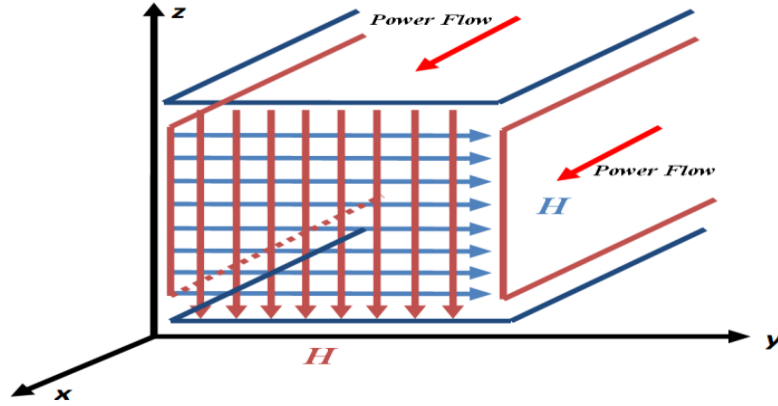


Figure 4.1 Illustration of the H-field generated within the quadrature PPW coils.

Unfortunately, the capacitive coupling of this coil is much severe than the magnetic coupling and canceling the capacitive coupling is a more challenging goal to achieve. During the coil fabrication, in order to transform the characteristic impedance of the PPW to the system 50 ohm impedance, two split tapered transmission lines were used at each side of the coil. But this matching technique makes the overlap between two PPW coils unavoidable and introduces unwanted capacitive coupling. If observe from the feeding point, these capacitances generated by the copper foil overlapping are in parallel with the input impedance of the PPW coil in schematic. If the reactance of the coupling capacitance at the Lamor frequency is comparable to the coil input impedance, the current flow will be divided between coil and coupling capacitors and will affect the coil performance negatively. The solution to this problem is to lower the coupling capacitance value by reducing the overlapped area of the copper foil. To fulfill this purpose, several decoupling strategies were adopted in the geometry design of the PPW coils. Firstly, the length of the outer transmission line coil was increased by 4 cm at both sides so that the feed points of the outer coil can be kept away from the inner coil. Secondly, since the

capacitance value is proportional to the size of the overlap area, cutouts were added at the overlap region of the copper foils to decrease capacitive coupling between two PPW coils as shown in Figure 4.2.

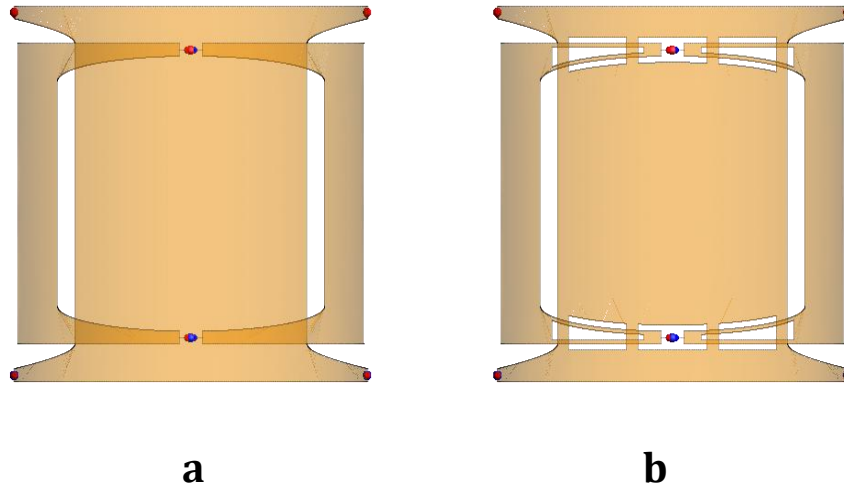


Figure 4.2 Front view of Quadrature PPW coils models a) without cutouts, b) with cutouts.

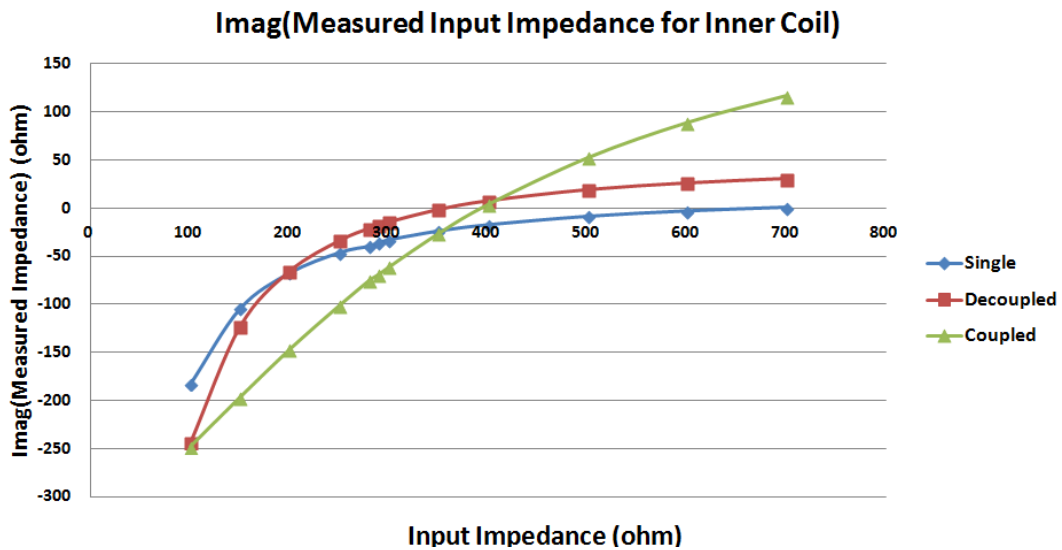


Figure 4.3 The comparison of imaginary part of the input impedance of inner coil (without loading) between three circumstances a). single inner coil, b) inner and outer coils with no decoupling strategies, c) inner and outer coils with decoupling strategies.

Since the current is mainly distributed at the edge of the waveguide structure, the cutouts added at the middle part of the copper foil won't affect the current flow on the waveguide surface. To determine the specific positions and dimensions of the cutouts, numerical simulations were performed on FEKO and evaluated the effectiveness of the capacitive coupling. Theoretically, if a PPW is working in TEM mode, its characteristic impedance will be a real number. But with another PPW coil positioned closely, the capacitive coupling will introduce imaginary part to the measured input impedance and can be observed from the simulated load impedance of the PPW coil. During the simulation process, the location and size of the cutouts were adjusted carefully until the imaginary part within the input impedance was close to that of an isolated coil as shown in Figure 4.3.

To further examine the effect of the cutouts have on capacitive coupling, the current distributions on a single PPW coil with and without the existence of the other PPW coil were compared. With proper decoupling methods employed, no obvious change of current flows was observed between these two different scenarios as shown in Figure 4.4.

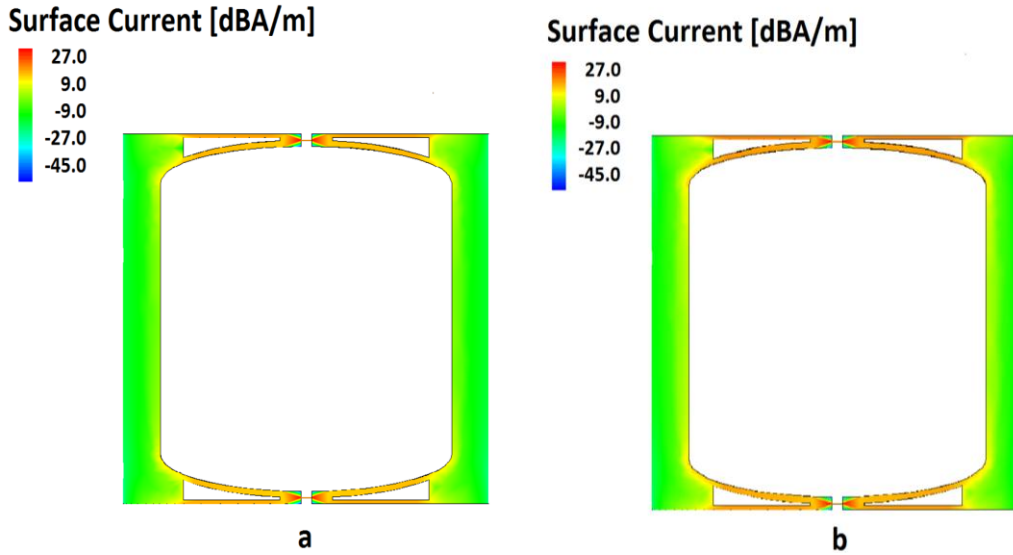


Figure 4.4: Current distribution on single inner PPW coil a).without outer PPW coil. b). Current distribution on inner PPW coil with outer PPW coil terminated with load impedance.

After deciding the decoupling strategies, the input impedances of the two sets of PPW coils were simulated. All the input impedances at four ports of the two sets of PPW coils were treated as identical due to the symmetry of the PPW coils and optimized through numerical simulation to minimize the power reflected so that no standing wave will be generated within the waveguide structure. The simulated input impedances at the input ports were used in the later broadband matching network design. Figure 4.5 shows the simulated optimal load impedances of the quadrature PPW coils. To mimic the loading of human leg, a cylinder filled with material ($\epsilon = 56, \sigma = 0.657$) was involved in the simulation.

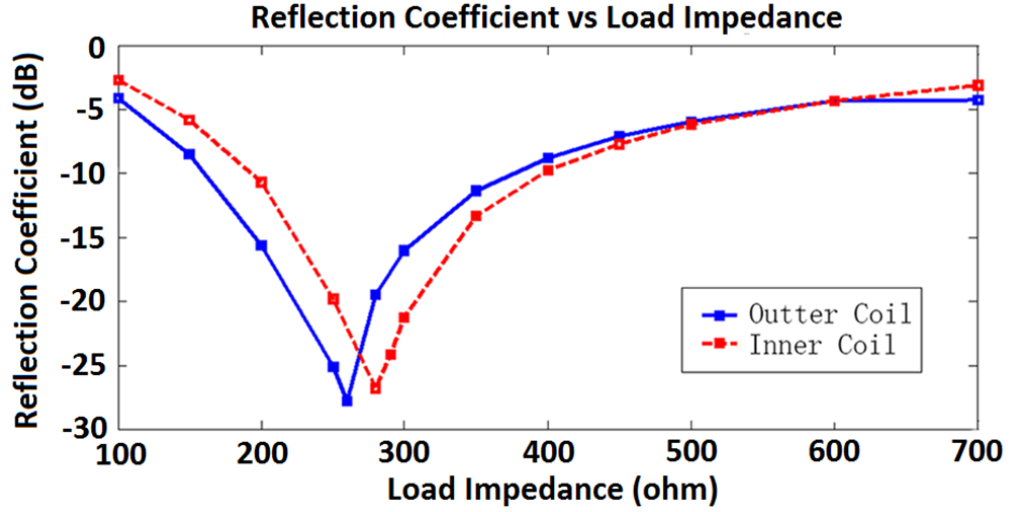
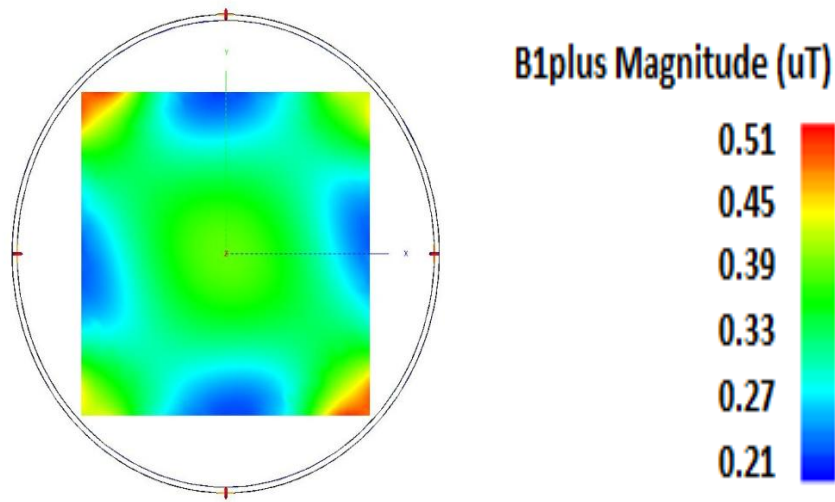


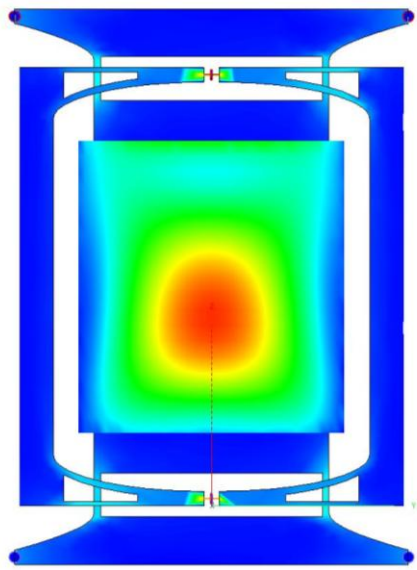
Figure 4.5: The optimization results of reflection coefficient versus the load impedance for the PPW coils.

For volume transmit coil, the B_1^+ field homogeneity is of the most importance during the design process to prevent non-uniformity within the target region. To test the field homogeneity, a quadrature excitation (same magnitude, 90 degree phase difference) was applied to the PPW coils in the simulation, and the B_1^+ fields of three planes were obtained by processing the obtained H-field distribution using equation (4.1)

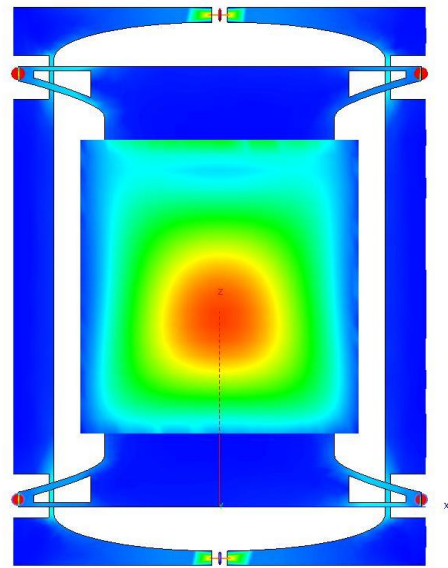
$$B_1^+ = \frac{B_{1,x} - jB_{1,y}}{\sqrt{2}} \quad (4.1)$$



a



b



c

Figure 4.6: B_1^+ field distributions of the quadrature PPW coils in a). Transverse plane.
 b). Sagittal plane. c). Coronal plane.

4.3. Transmit Coil Fabrication

With numerical simulation finished, the PPW coils were implemented with adhesive backed copper foil (3M, St Paul, MN, USA) mounted onto the inner and outer surface of a fiber glass tube. The length and diameter of the inner PPW coil are 30 cm and 26.035 cm. The length and diameter of the outer PPW coil are 38 cm and 26.67 cm. All these dimensions were chosen as suitable for human leg imaging application. Furthermore, to diminish the eddy current introduced, several slots were also cut on the surface of both PPW coils and 1nF capacitors were soldered across these slots.

Since both the PPWs and the tapered line transformers are wideband, a broadband matching network which transforms impedance of the transmission line coil at all four ports to 50 ohm system impedance was designed to make the whole transmit structure functional within a wide range of frequency. The benefit of this technique is that the detuning of the transmit coil caused by the shift of the resonant frequency when different loading were applied can be avoided. To fulfill the requirement of broadband matching, same band-pass Chebyshev impedance matching network used in the linear PPW coil were designed and fabricated specifically for both inner and outer transmission line according to their load impedances. The center frequency of the Chebyshev impedance transformer was set as 123.2MHz and the passband edge-to-edge width was approximate 100 MHz. A 10-th order impedance transformer was employed to flat the passband so that perfect impedance matching can be realized within the whole 100MHz frequency band and the reflection loss can be reduced to the largest extent. This broadband matching network with Chebyshev frequency response was designed and optimized in ADS filter design guide (ADS 2011.10; Agilent Technologies). In fabrication, fixed high-

Q ATC-100B capacitors (American Technical Ceramics, Huntington Station, NY) were used to reduce the insertion loss of the matching network. Through numerical simulation, the impedances at the feeding points for inner and outer PPW coils were determined as 260 ohm and 280 ohm. When terminated with these impedances, the simulated reflection coefficients for both PPW coils were below -25dB at 123.2 MHz. To match the PPW coils to the system 50 ohm characteristic impedance, following broadband Chebyshev matching circuits were employed. Figure 4.7 (a) and 4.7 (b) show the schematic circuits and component values of the matching networks. And in order to suppress higher-order modes of the waveguides, the matching networks were last transformed to balanced form. The measured reflection coefficients are below -20 dB over an approximate 100 MHz frequency range as shown in Figure 4.7 (c) and 4.7 (d).

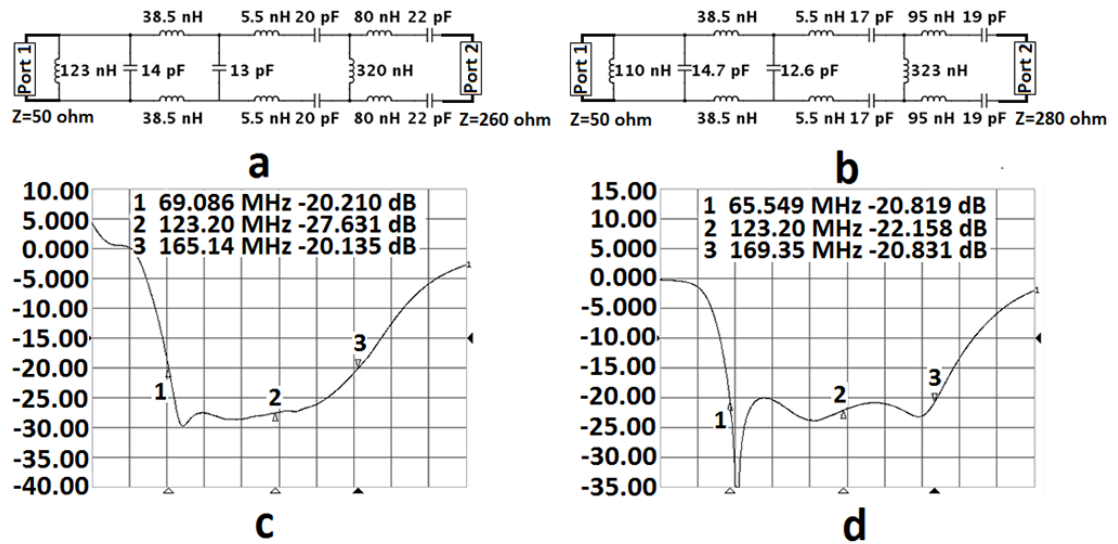


Figure 4.7: Schematic of the Chebyshev matching network of (a) the outer PPW coil and (b) the inner PPW coil. Reflection coefficient measured for (c) outer PPW coil’s matching network and (d) inner PPW coil’s matching network.

To connect the transmission line coils to the system interface, a equally split Wilkinson power divider with center frequency of 123.2MHz was used at the driving end of the PPW coils which splits the system input power equally in both magnitude and phase and feeds into the coils. At the terminating end, a same Wilkinson power divider was added to combine the power of two output ports. To re-use the RF power flowing out of the PPW coils, the RF power at termination side was connected back to the driving side and combined with the system input power using a third Wilkinson power combiner. To realize the maximum transmit power usage, the phase of the re-circulate power was compensated to in-phase with the input power to prevent any power cancellation due to the phase difference. All Wilkinson power divider and combiner circuits were implemented with ATC-100B capacitors and the 164-series and 165-series tunable inductors (Coilcraft, Cary, IL). Since this coil was designed for 3T testing purpose, conventional narrow-band 1:1 Wilkinson power divider working at 123.2 MHz was used as power splitter and combiner. The power dividing ratio was -3.2 dB for both two output ports and the phase difference was -3° .

4.4. Bench-testing

A head phantom filled with saline water of $\epsilon = 56, \sigma = 0.657$ was used as the loading in the bench testing procedure of both quadrature PPW coils and receive array to mimic the loading of human head. The reflection coefficient was measured for both inner and outer PPW coils. With the existence of the loading, the measured S11 for both coils were below -17dB as shown in Figure 4.9 (b) and Figure 4.9 (d), which represents only about 2 percent of the transmit power will be reflected back to the system. Under the circumstance of totally no loading inside the coil, the S11 measured for both PPW coils were still below -15dB (Figure 4.9 (a) and Figure 4.9 (c)) which demonstrates that the quadrature PPW coils are quite insensitive to the change in loading. The frequency span for the measurement of reflection coefficient was 60MHz and the measured reflection coefficients included the PPW structure, Chebyshev matching networks and the Wilkinson splitter/combiner as shown in Figure 4.8.

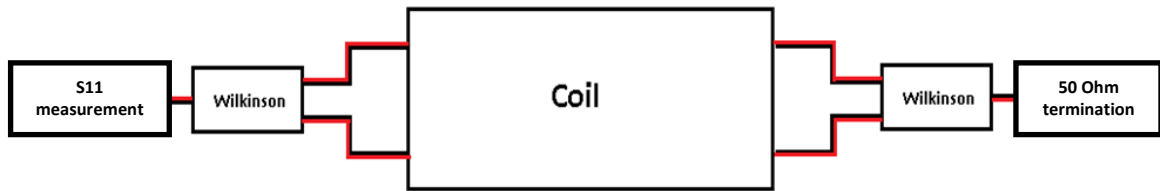


Figure 4.8: Bench-testing setting-up for the reflection coefficient measurement for both inner and outer PPW coils.

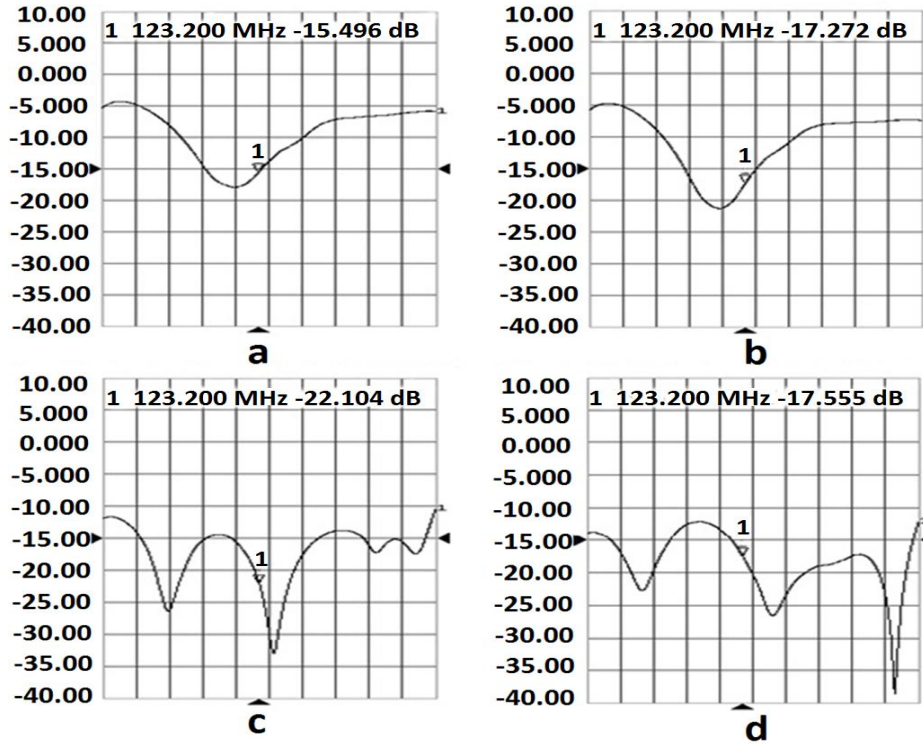


Figure 4.9: Bench measured reflection coefficient of inner PPW coil (a) without phantom and (b) with phantom. Bench measured reflection coefficient of outer PPW coil (c) without phantom and (d) with phantom.

Similar to the linear PPW transmit coil, power feedback was added to the design to achieve optimal transmit efficiency. The phase difference between transmit power and feedback power was compensated to integer number of 360 degree during bench-testing. To measure the total phase delay of the feed-back power path, the port of the Wilkinson combiner for the re-entrant power connection was terminated by 50 ohm, and the phase delay of the feedback power path was measured using network analyzer as shown in Figure. 4.10.

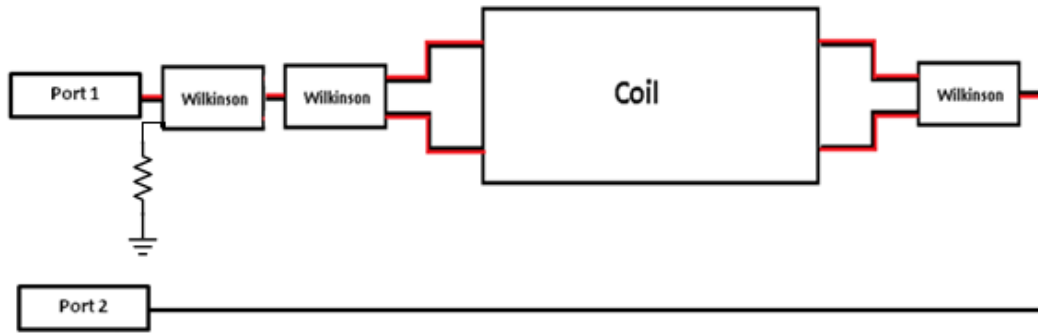


Figure 4.10: Bench-testing setting-up for the phase delay measurement of the PPW coils.

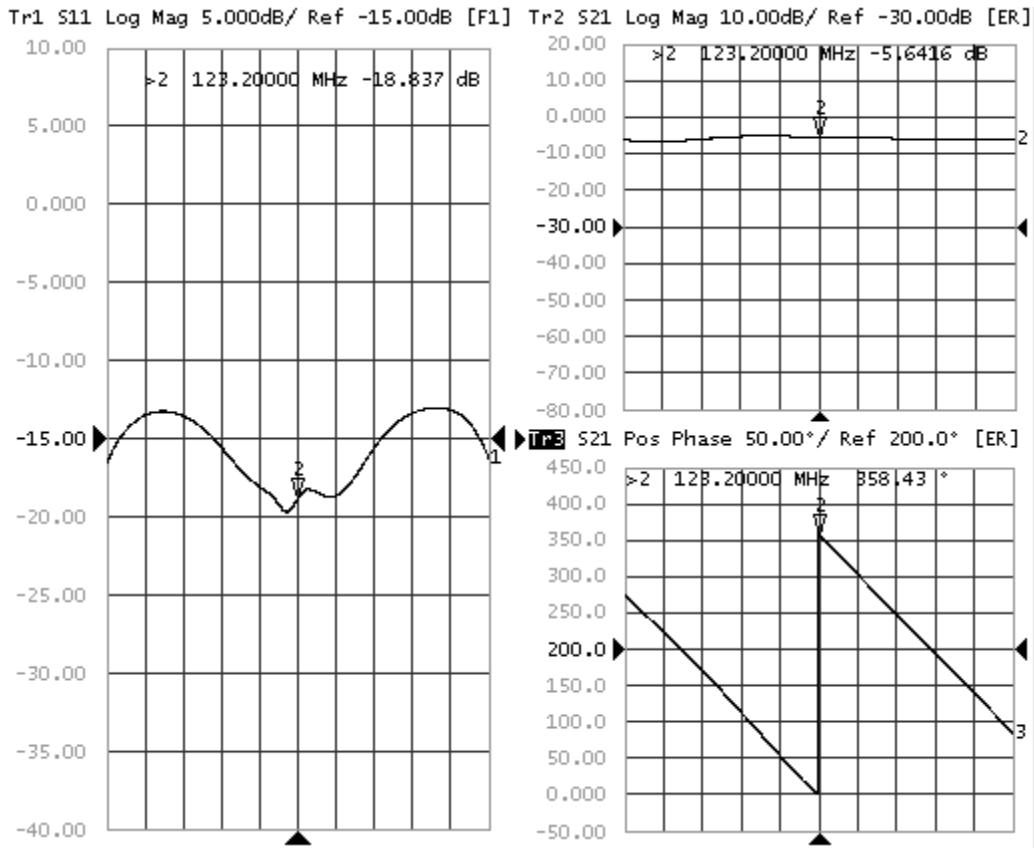


Figure 4.11: Bench measured phase delay of the power re-entrant path of the inner PPW coil.

The phase delay of the re-entrant power was adjusted to integer number of 360 by adjusting the length of the coaxial cable as shown in Figure. 4.11. The total power loss which includes PPW coil's loss, radiation loss, phantom loss, cable loss and front-end circuits' attenuation is -2.64 dB at 123.2MHz. Same measurements were performed on the outer PPW coil and the results are shown in Figure. 4.12. The power loss for the outer PPW coil is approximate -2.44 dB.

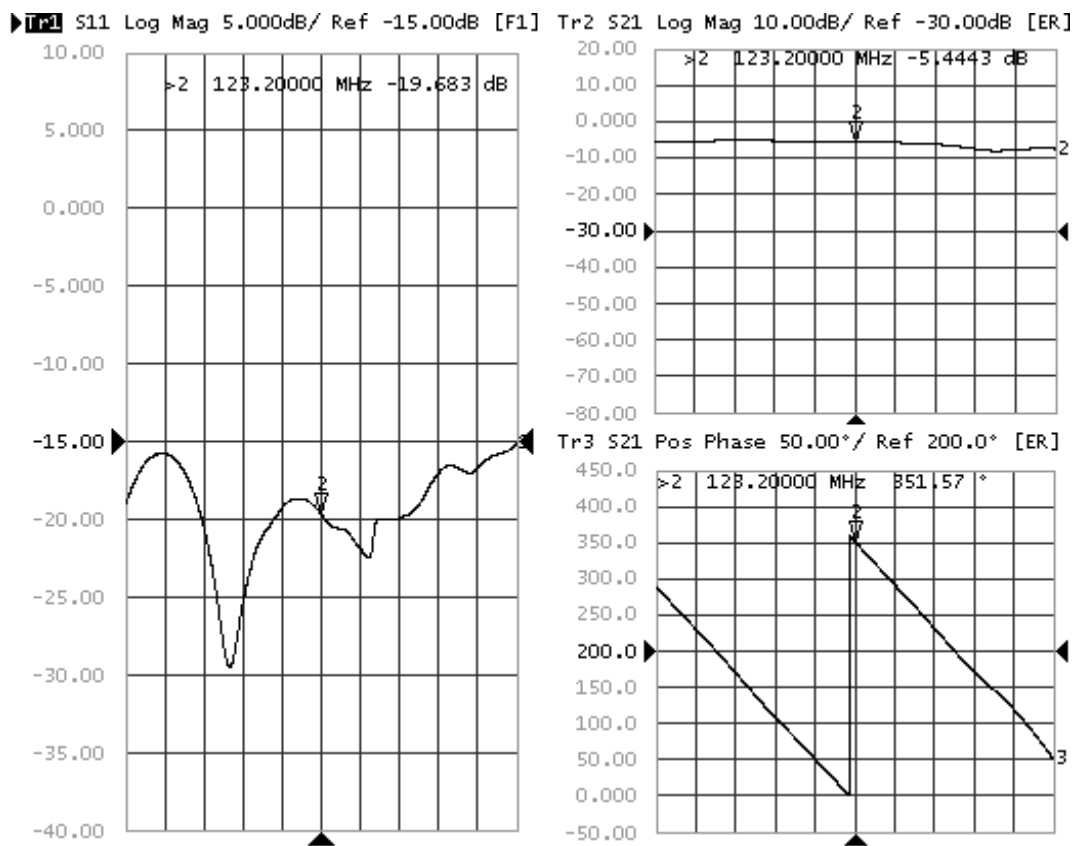
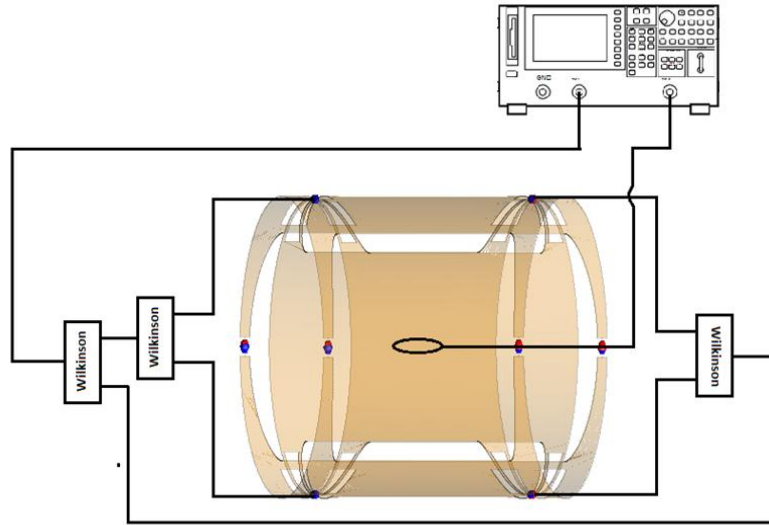
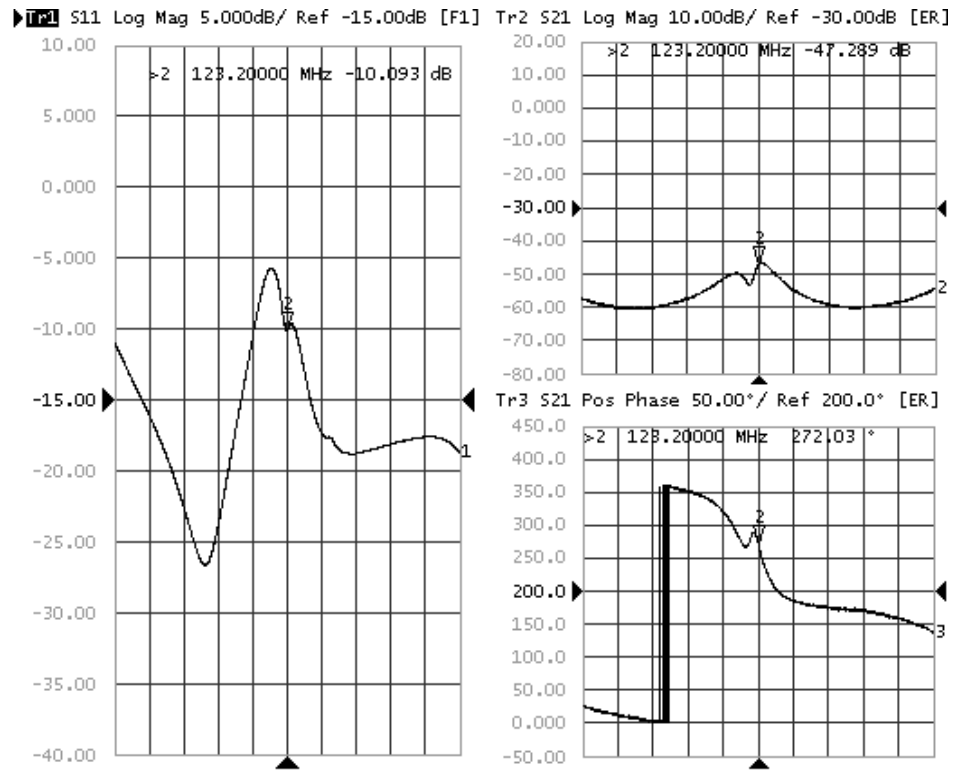


Figure 4.12: Bench measured phase delay of the power re-entrant path of the outer PPW coil.

Before performing the experiments on scanner, the transmit efficiency of both inner and outer PPW transmit coils was also tested qualitatively using a single loop probe with following experiment setting-ups as shown in Figure 4.13. The input of the PPW coils was connected to the port 1 of the network analyzer for excitation, and the single probe was connected to port 2 to detect the electromagnetic fields inside the PPW coils. The signal was detected for both inner and outer PPW coils with probe positioned in the plane which is perpendicular to the corresponding electromagnetic fields. Since the probe gain is proportional to the transmit efficiency which is $(B_1^+)/\sqrt{P}$, the homogeneity of the B_1^+ field generated can be tested by the sliding the probe within the PPW coil with the probe plane kept perpendicular to the electromagnetic fields and observing the strength of the detected probe signal. As shown in Figure 4.13 (b) and Figure 4.14 (b), the detected signal levels of inner and outer PPW coils are identical in both magnitude and phase which demonstrate the consistency between the PPW coils fabricated and guarantee that the quadrature excitation can be achieved and reduce the power consumption to half approximately.



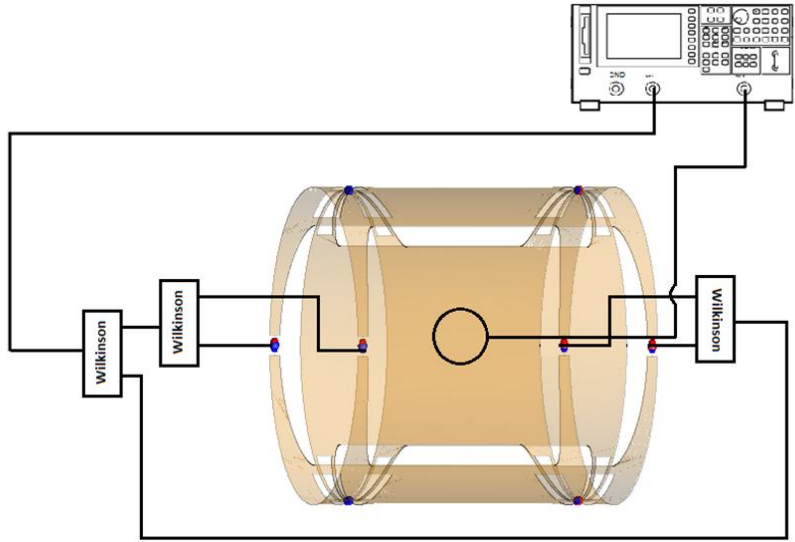
a



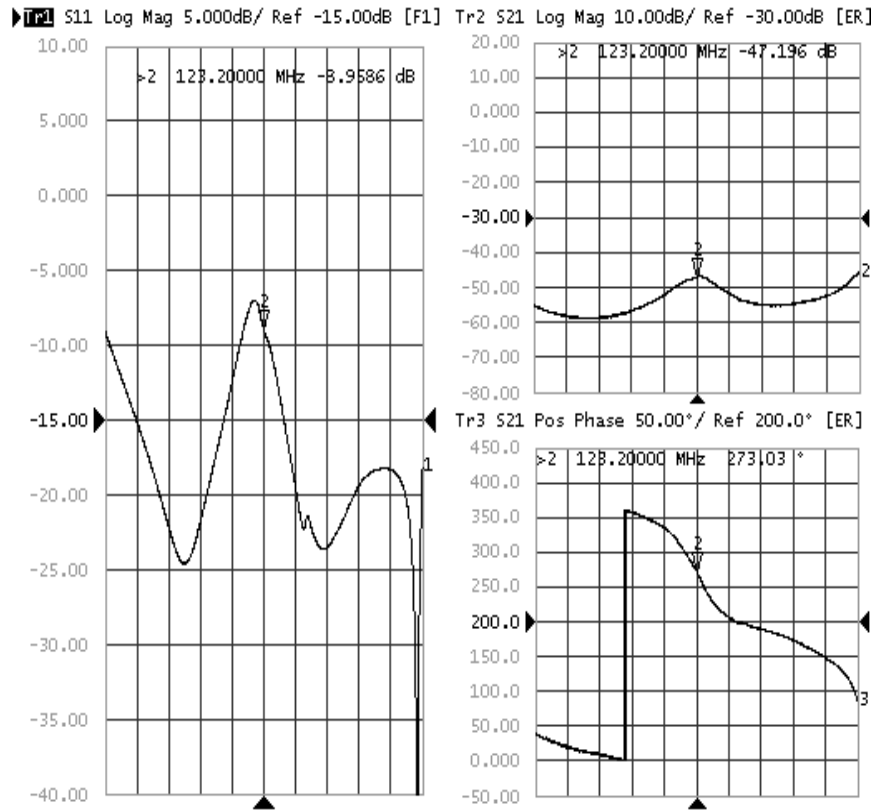
b

Figure 4.13: Bench measurement of the transmit efficiency of inner PPW coil at the coil center

a) Measurement setting-up b) Signal level detected.



a



b

Figure 4.14: Bench measurement of the transmit efficiency of outer PPW coil at the coil center

a) Measurement setting-up b) Signal level detected.

4.5. Receive-only Array Design

Because that the quadrature PPW coils cover a much larger volume, it's inappropriate to use them as receiver again as what has been done for the small size linear PPW coil. Otherwise, the SNR of the obtained image would be extremely low. Therefore, a de-tunable four channel receive-only array was designed and fabricated to increase local SNR and prove the feasibility of using the quadrature PPW coils for homogeneous transmit field generation. Since the transmission line coils were built on a cylindrical tube, to realize an optimal SNR and field coverage, a conformal structure was also employed for the receive array so that it could be closely fit to both PPW coils and scanning subjects. The receive array was located about 1 cm away from the transmit coil and about 2 cm from the human tissue for patient safety. To eliminate the mutual coupling between all the receive elements, two decoupling strategies were employed for the receive array. For the head-to-head two elements, capacitance decoupling was used. The decoupling was realized through adjusting the capacitor values on the shared edge of the two receive elements. For neighboring two elements, decoupling was accomplished by changing the size of the overlap area. All above decoupling steps were performed firstly in numerical simulation to provide a reasonable starting point for later receive array fabrication.

4.5.1. Numerical Simulations

Numerical simulations were performed to determine the capacitors' values for tuning and size of the overlap area for the decoupling. In the real experiments, the receive array would be working in the quadrature PPW coils. Therefore, the matched PPW coils were also involved in all the simulations to mimic the working condition of the receive array and increase the simulation accuracy. A single receive element was firstly tuned to 123.2 MHz (3T) by carefully adjusting the value of the tuning capacitor as shown in Figure 4.15.

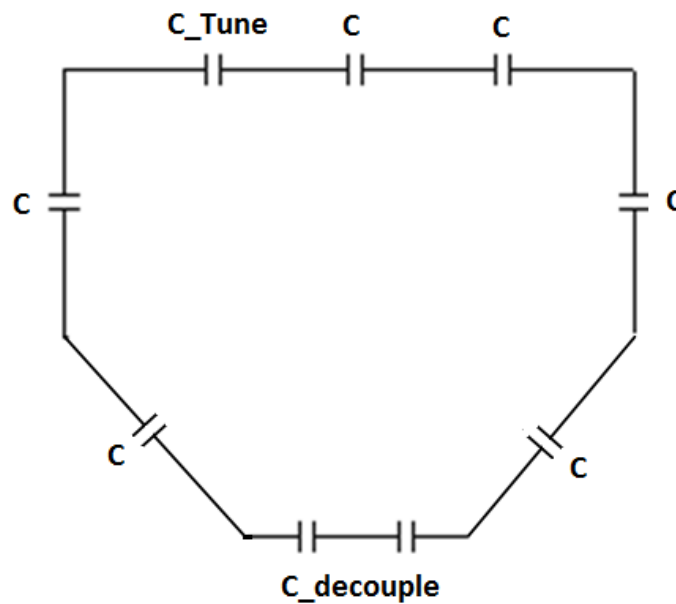


Figure 4.15.: Schematic of the receive element in the 4-ch receive array.

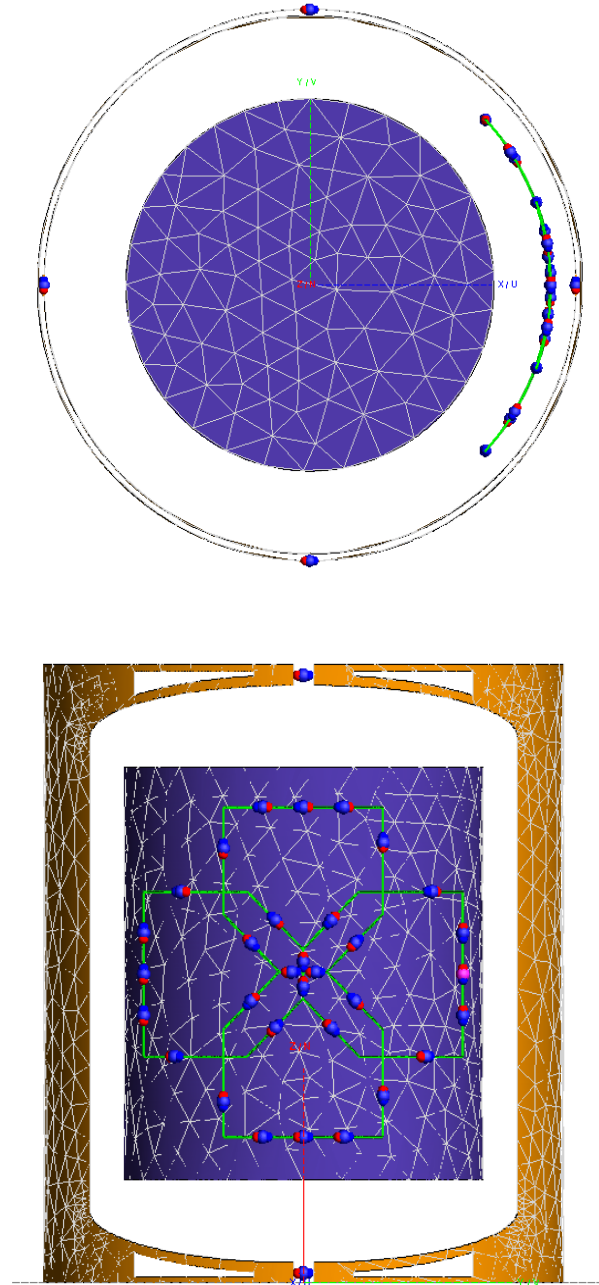


Figure 4.16.: Top and front views of the model of the receiver array positioned in the quadrature PPW coils.

Then the tuned head-to-head coil was added into the simulation. The decoupling capacitors on the shared edge were carefully tuned to achieve capacitive decoupling. However, after changing the values of the decoupling capacitors, the tuning frequencies of these two elements would shift away from 123.2 MHz and it's necessary to re-tune the coil elements by changing the values of the tuning capacitors. After repeating above procedure for several times, the two head-to-head receiving elements were completely decoupled. Same decoupling process was performed for each pair of neighboring elements. The size of the overlapped area was finely adjusted until fully overlap decoupling was accomplished.

To prove the decoupling effect, each of the four receive elements were excited separately in simulation, and the induced current on all other three elements were examined as shown in Figure 4.17. With any one of the receive elements excited, the induced currents on the other three coil elements are controlled to an extremely low level which proves the effectiveness of the decoupling strategies employed.

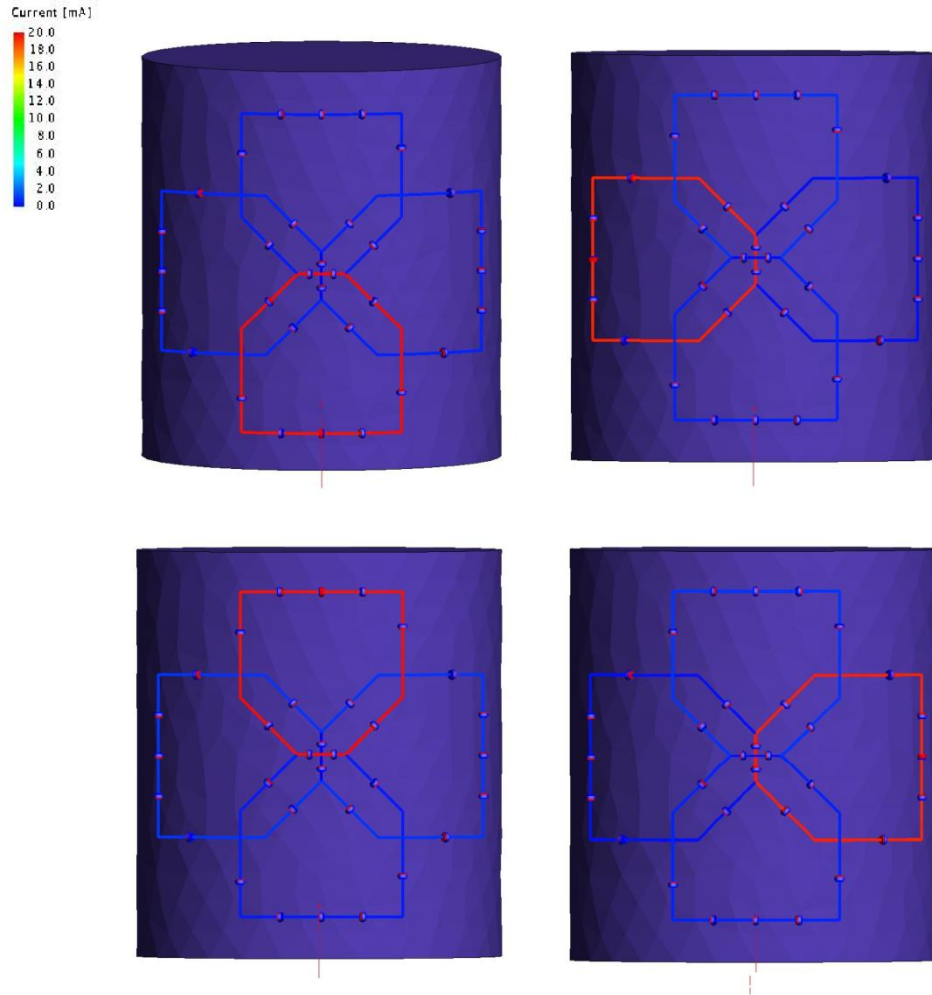


Figure 4.17.: Current distributions on all receive elements with four elements excited separately.

Then the receiving profiles of each receive element at sagittal plane were obtained on a human head phantom filled with dielectric material (permeability= 56 and conductivity = 0.657) and plotted using Matlab as shown in Figure 4.18.

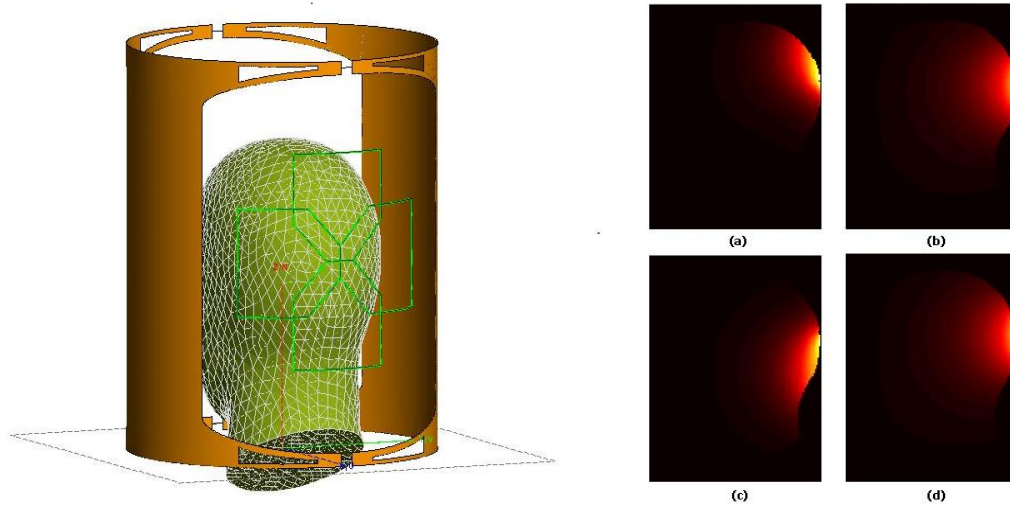


Figure 4.18: Receiving coil profile simulation model (The outer PPW coils is hidden to show the receive array) and simulated profile of four receive elements in sagittal plane.

After numerical simulations, the coil and shield frames were designed for convenience in system interfacing and mechanical robustness during the MR scanning. The coil layout was directly subtracted from the coil frame and slots were left on the frame so that the coil layout which had best simulation results could be precisely transferred to the fabrication. Then the designed model were imported to AutoCAD for further adjustments on dimensions and exported as .stl file for 3D printing. AWG # 16 copper wire was used to build the receive array, and 9 fixed value capacitors (American Technical Ceramics Co., Ltd.) were soldered onto each receive element for tuning it to 123.2MHz. . To detune the receive array during transmitting, a PIN diode (MA4P7470-1072T, Macom, Lowell, MA) was connected in shunt of the matching board of each receive element.

4.5.2. Q-factor Measurement

For receive-only coil, the Q-factor is always used as a gauge of whether it is properly designed. The Q-factor ratio can tell which noise dominates, coil noise or phantom noise. If the coil noise contributes much more, the RF coil needs to be re-designed such as reduce soldering points and use high-Q components (capacitors and inductors) in order to decrease the coil loss. The quality factor Q is defined as the ratio of the peak magnetic energy stored by the coil divided by the average energy dissipated per radian by the coil. Equivalently, it can be seen as the ratio of the reactive impedance divided by the resistive impedance. $Q = \omega_0 L/R$. In bench-testing, Q can be measured as $\omega_0/(2\Delta\omega)$. ω_0 is the frequency at the peak, and $2\Delta\omega$ is the full width at half maximum (FWHM)

To ensure the high receive sensitivity of the receive elements, Q_{Loaded} and Q_{Unloaded} are measured using double-probe for an isolated coil in the receive-array and Q_{Ratio} is calculated using Equation (4.2).

$$Q_{\text{Ratio}} = \frac{Q_{\text{Loaded}}}{Q_{\text{Unloaded}}} = \frac{67.21}{271.69} = 24.74\% \quad (4.2)$$

The calculated Q_{Ratio} is 24.74% which shows that the phantom noise dominates.

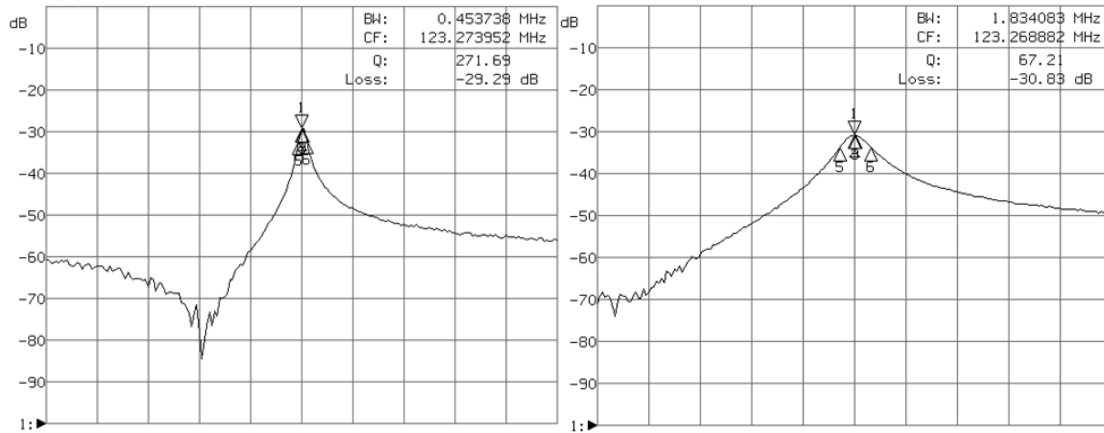


Figure 4.19.: Measured unloaded Q and loaded Q of single isolated receive coil.

4.5.3. Detune Circuit

Due to the large RF power transmitted by the transmit coil, if receive coils are still actively resonating during the RF transmit portion of the pulse sequence, the power from the transmit coil could be coupled into the body through a resonating receiver loop and could potentially deposit large amounts of power in the patient. To maintain patient safety and to protect the sensitive receiver equipment, the receive coils are typically detuned during the transmit phase of the MR pulse sequence. Both passive and active detuning circuits can be used to fulfill this task.

In this study, a PIN diode active detune circuit was used. A PIN diode was shunt connected at the input side of the pi matching network and biased by the Pin diode signal in the scanner system. When the transmit coil is on, the PIN diode will be forward biased and exhibit a short in RF. Through the quarter-wavelength transformation, high impedance was introduced at the input of the coil so that the coupled power in the receive coil can be greatly reduced.

In bench-testing, the matched coil was terminated by 50 ohm using coaxial cable to simulate the working condition in the scanner. A decoupled double probe was placed closely to the RF coil and connected to the network analyzer following the setting-up shown in Figure 4.20.

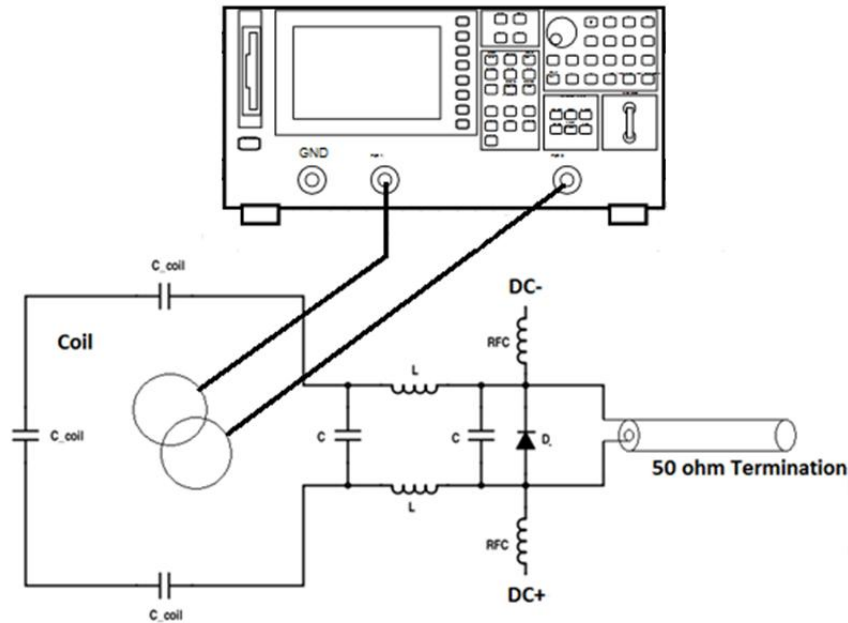


Figure 4.20: Bench measurement setting-up for the detune circuit using decoupled double probe.

The change in S21 level was used to measure the amount of detuning providing by the detuning circuit. Without detuning applied, a resonant peak was obtained at 123.2MHz as shown in Figure 4.21. When DC bias was turned on, a high impedance was inserted into the coil and a reduction ($>20\text{dB}$) in the S21 was observed. In this experiment, the distance between probe and coil was kept constant.

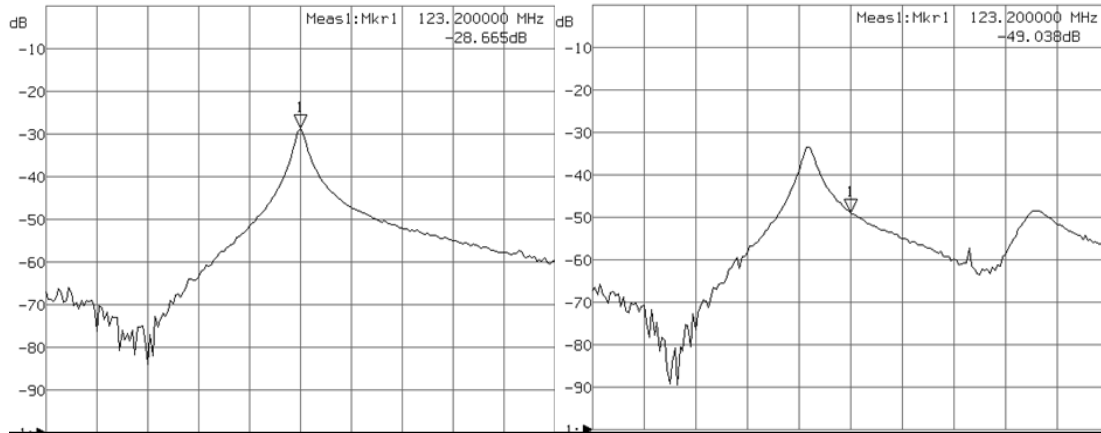


Figure 4.21.: Measured frequency response of single receive element with and without detuning circuit.

Finished the bench measurements of a single receive element and made sure that receive coil quality met the design requirements. All the four receive elements were assembled and the decoupling between all receive elements was performed. The same decoupling procedures used in numerical simulation were followed on bench top and the S-parameters were recorded as following table. Reflection coefficients of all elements were kept below -17dB to minimize signal reflection. The transmission (S21) measured between any of two elements were measured as below -14dB so that the coupling level was well-suppressed.

S-parameters	Coil 1	Coil 2	Coil 3	Coil 4
Coil 1	-19.5	-14.2	-14.1	-15.2
Coil 2	-14.2	-26.5	-17.9	-16.4
Coil 3	-13.9	-18.3	-17.6	-14.8
Coil 4	-14.1	-18.3	-14.6	-18.4

Table 4.1: Measured S-parameter matrix of the four-channel receive array.

It should be noted that, to mimic the working condition of the receive array during scanning, all the bench-top measurements of the receive-only array were all performed within the matched PPW coils as shown in Figure 4.22.

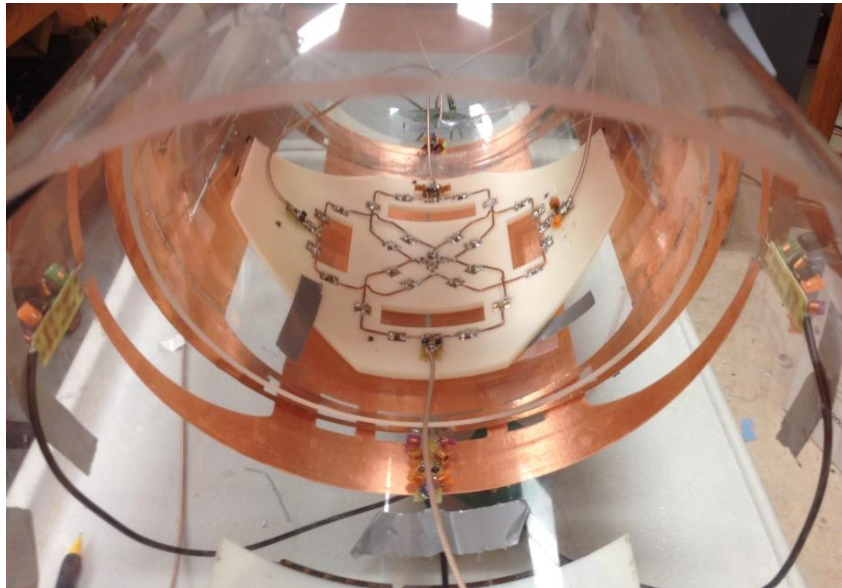


Figure 4.22: Four-channel receive array positioned in the matched quadrature PPW coils.

4.5.4. Common Mode Current Suppression

Coaxial cables are often used to connect the receive coils to the scanner so that the received MR signals could be collected by the system and generate MRI images. However, when coaxial cables are positioned in the strong magnetic field, unwanted common mode current would be generated on the outside surface of the shield of the coaxial cables. For transceiver case, common mode currents flow as a result of unbalanced loop voltages that couple to the cable shield. For receive array coil, the common mode signals are induced directly from the field of the transmission coil onto the cable shield. Especially, when the cable length exceed free-space wavelength at high frequency, cable shield behaves like antennas which radiates power into free space and cause loss in SNR and patient safety concern.

During the receive-only coil array fabrication in this study, several methods were used to address problems caused by the common mode current. First, the coaxial cables were routed with great care to avoid placing the cables along with direction of the strong field of the transmit coil so that the current coupled from the transmit field could be greatly reduced. Secondly, a virtual ground was achieved at the center line of the coil by using symmetric structure for both RF coil and matching circuit. In this manner, equal and opposite voltages can be obtained at the feeding point so that a balanced scheme could be achieved and suppress common mode signal. However, in receive-only case, the balanced matching network is incapable of suppressing the current on outside surface of the cable shield completely and common mode signals may still exist. Therefore, cable traps which chokes common mode currents were applied onto the coaxial cables at every

1/10 wavelength to guarantee the elimination of the unwanted common mode currents. To fabricate a cable trap, the insulation layer of the coaxial cable was removed for a small portion and a fixed value capacitor was connected in parallel with the cable shield. The capacitor's value was carefully tuned so that the parallel LC-tank resonates and inserts a large impedance to the shield currents at the Larmor frequency.

4.6. System Interface

The quadrature PPW transmit coils and its local receive array were tested on a Siemens verio open-bore 3T scanner (Siemens Healthcare, Erlangen, Germany) to prove its feasibility. To connect the PPW coils and receive array to Siemens 3T scanner, two interface boxes were used for quadrature transmit and 4-channel receive. The transmit interface box provides two quadrature output ports (0° and 90°) to which the transmit coils can be connected directly as shown in Figure 4.25. In the four-channel receive only interface box, the DC control signal is combined with RF signal via bias tee to control the receive elements for active detuning as shown in Figure 4.24.

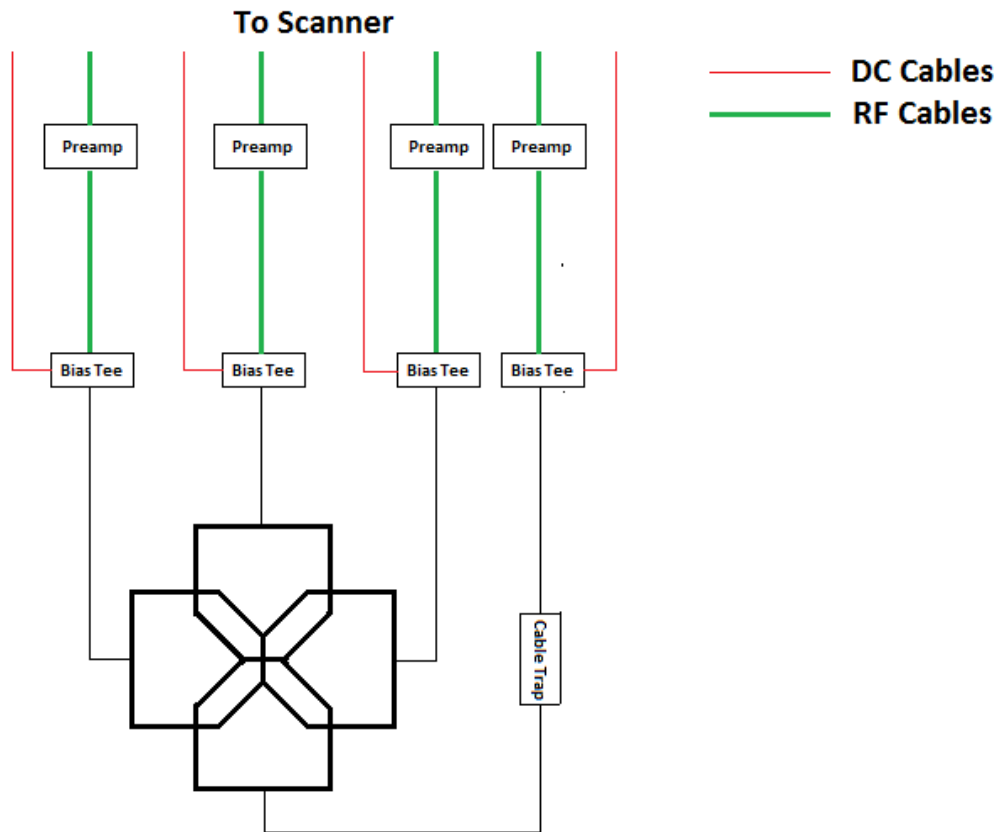


Figure 4.24: Schematic representation of the four-channel receive array connected with system through interface.

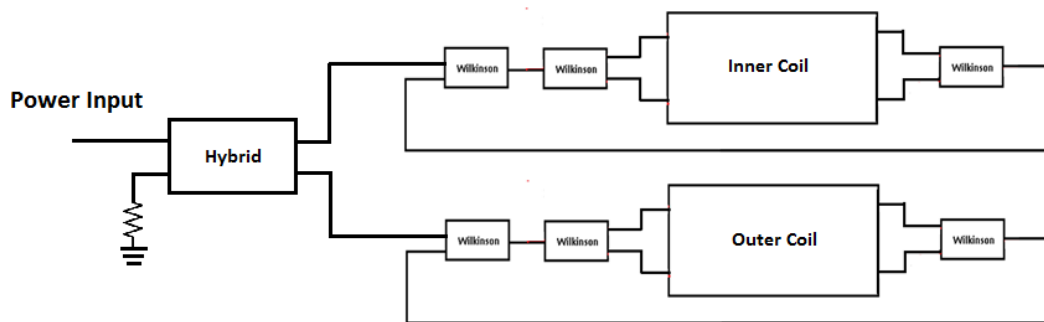


Figure 4.25: Schematic representation of the quadrature PPW coils connected with system through interface.

4.7. MRI Measurements

4.7.1. Transmit Efficiency Improvement using Quadrature Structure

The quadrature PPW coils were tested in 3T scanner for both linear mode and quadrature mode to prove the improvement in transmits efficiency. In all scanning experiments, same head phantom was used to mimic the loading of the human head and the conformal receive array was positioned at the bottom of the head phantom and kept about 2 cm away from the phantom. During the linear transmit mode experiments, the outer PPW coil was disconnected and the inner one was remained in working condition. The two quadrature output ports of the transmit interface box were combined using a hybrid coupler whose working frequency is 123.2MHz and then fed into the inner PPW coil for excitation. The normalized signal intensity at the center area of the head phantom was measured versus RF transmit voltage and recorded. The gradient echo sequence with following parameters was used: FOV=320*320, Resolution=256*256, Voxel size=1.3*1.3*5.5mm, TR=50 ms, TE=3.46 ms, Average =1, Nominal flip angle =10 degree. Then the same GRE sequence and experiment procedure were repeated for the quadrature transmit mode (both inner and outer PPW coils in transmit) and the scanning results were compared with that of the linear transmit. The optimal transmit voltage was found as 78 V and 47V for linear and quadrature structure respectively. An approximate 40 percent improvement in transmit efficiency was observed as shown in Figure 4.26. Figure 4.27 shows the GRE images obtained using both linear and quadrature excitations.

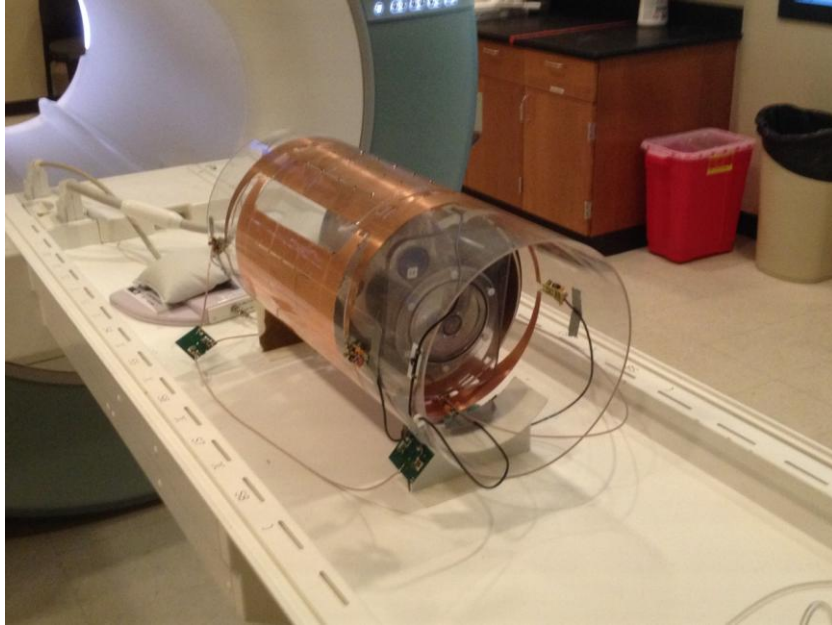


Figure 4.25: Scanning experiments setting-up for transmit efficient measurement on head phantom.

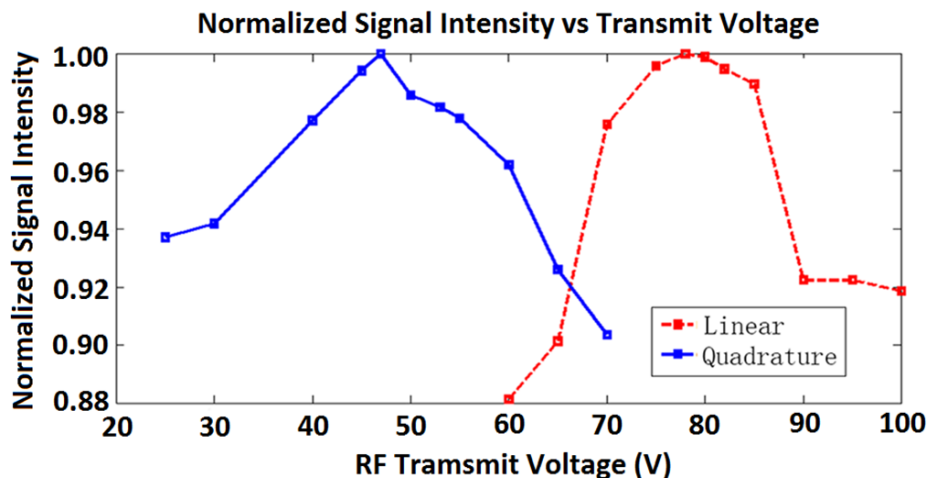
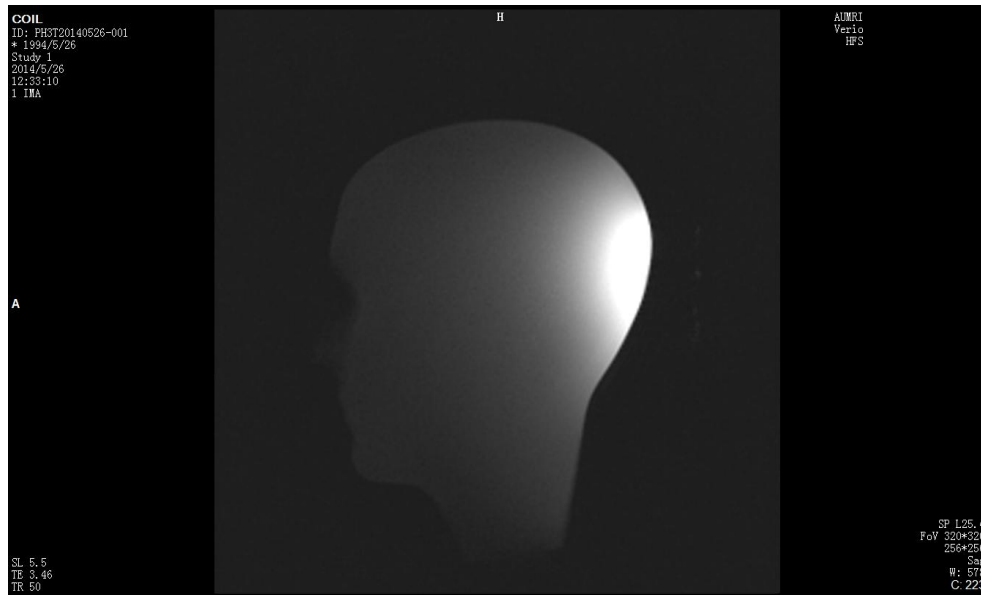
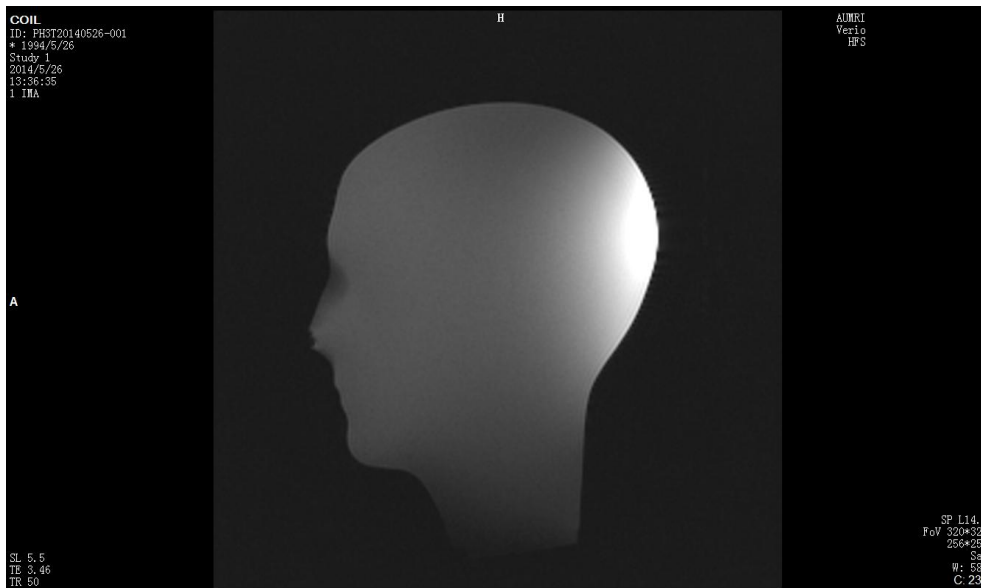


Figure 4.26: Normalized signal intensity versus transmit voltage for linear and quadrature structure.



a



b

Figure 4.27: GRE images of head phantom in sagittal plane using a) Linear excitation. b) Quadrature excitation.

4.7.2. 1H Images

The uncombined images of the four-channel receive array in sagittal plane were obtained using same GRE sequence (Figure 4.28) and compared with the simulated receive coil profile in section 4.5.1. The uncombined images are with high SNR and are consistent with the simulated coil profile which demonstrate the high sensitivity of the fabricated receive array and the effectiveness of the employed decoupling strategies.

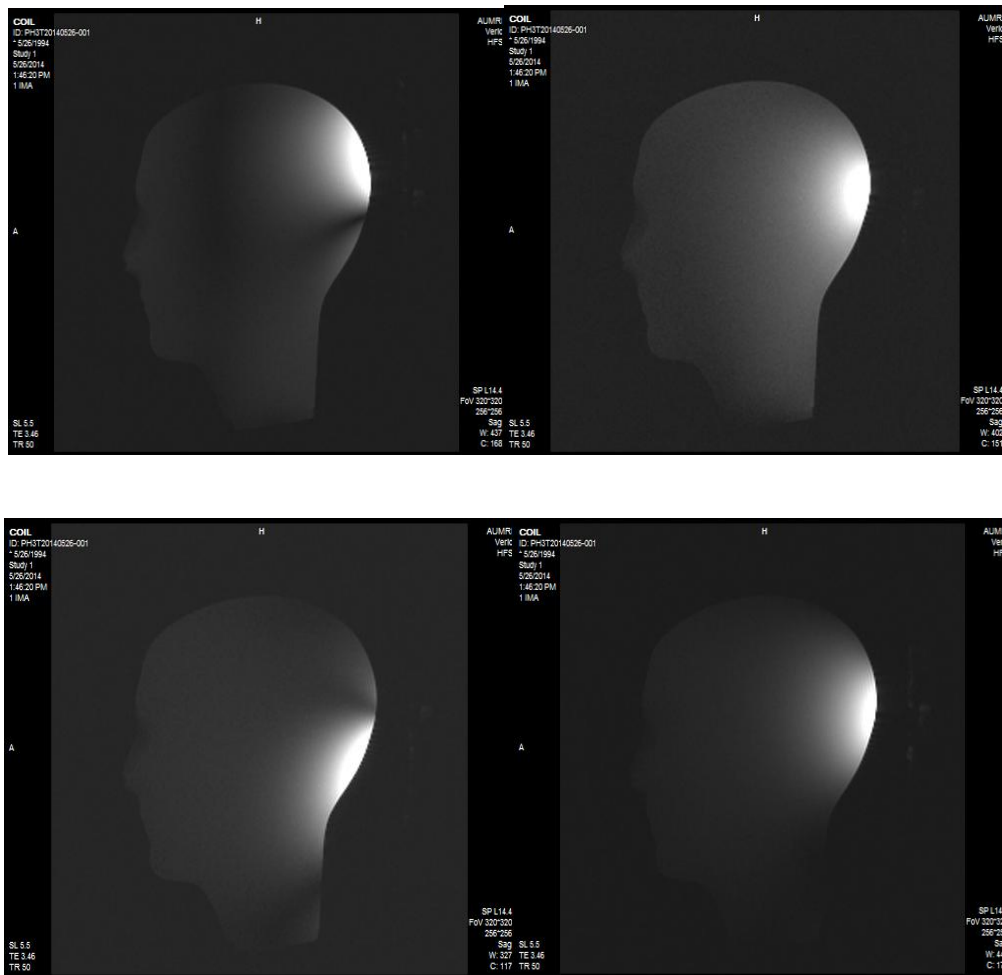


Figure 4.28: Uncombined images of the four-channel receive array obtained using GRE sequence.

Other than phantom testing, scanning experiment was also performed on human leg. The images were taken using spin echo sequence with following parameters: FOV=200*200, Resolution=256*256, Voxel size=0.8*0.8*3 mm, TR=50 ms, TE=3.78 ms, Average=1, RF Voltage=100 V and nominal flip angle =10 degree on calf muscle of a healthy volunteer. The spin echo images of the calf muscle of sagittal and transversal plan are shown in Figure 4.30. The brighter area in the images are related to the profile of the receive array.

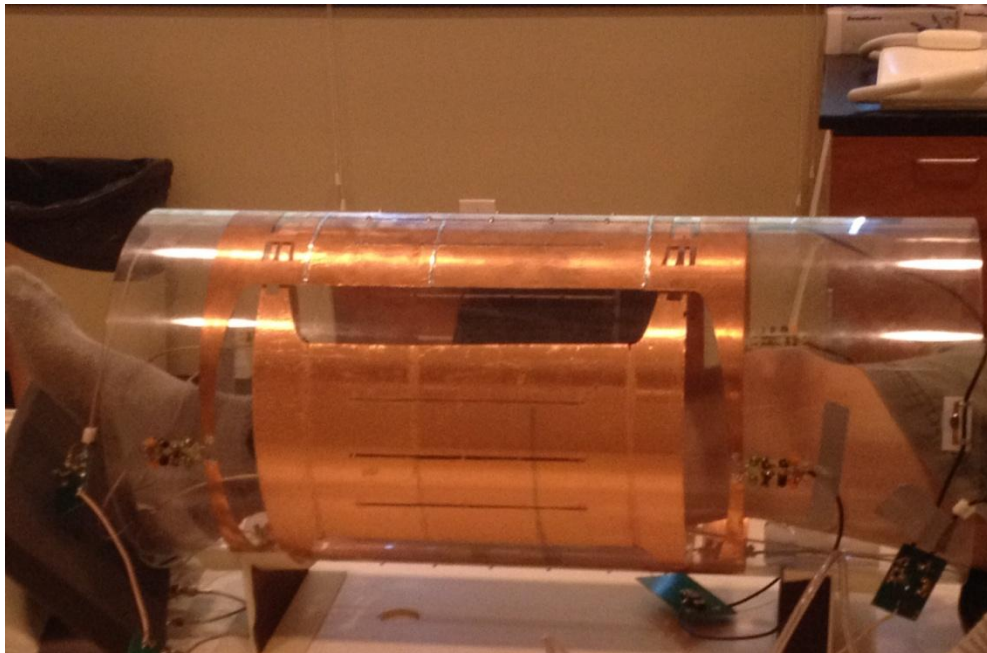
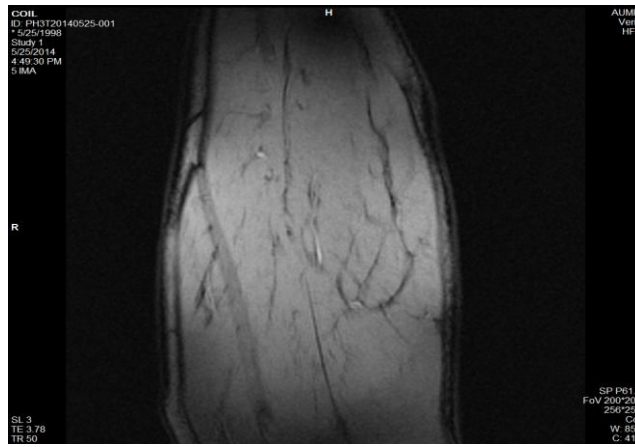
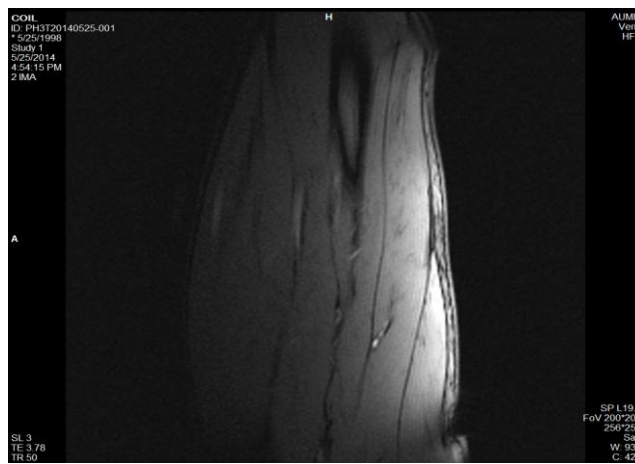


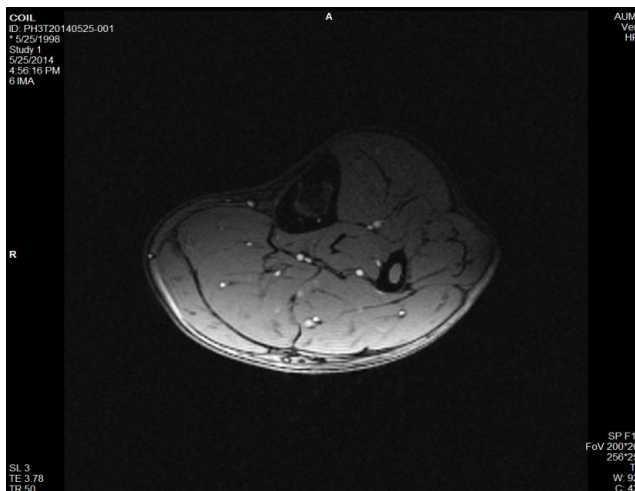
Figure 4.29: Scanning experiments setting-up for human leg imaging.



a



b



c

Figure 4.30: The spin echo images of the calf muscle. a).Coronal plane b). Sagittal plane and c). Transversal plane.

4.8. Conclusion

In this chapter, the feasibility of using quadrature PPW coils for large volume transmission in MRI was investigated. The transmit efficiency of the quadrature transmit excitation was compared with that of the linear excitation and an approximate 40% gain in transmit efficiency was obtained. The performance of the 4-channel receive array was tested both on bench top and through scanning experiments. High SNR images were obtained from head phantom and human leg. The uncombined images of all four receive elements were compared with the simulated receive profile and demonstrate the effectiveness of the decoupling methods employed.

5. Future recommendations

In Chapter 2, the designed and fabricated front-end circuits are used for research purpose. With -3dB total insertion loss, half of the RF power will be dissipated on the front-end circuits. To achieve optimization on circuits' performance, high quality inductors can be used in future applications so that the insertion loss of the passive front-end circuits could be further reduced. For the preamplifier, RF shield can be added to minimize the negative impact of the strong magnetic field.

In Chapter 3, for the purpose of proof-of-concept, the linear PPW coil is used for acquiring phosphorous spectroscopy signal. To enhance the SNR of the ^{31}P signal, a separate receive-only array is preferred.

In Chapter 4, a four-channel receive-only array is used to boost the local SNR of the ^1H images. Due to the dimensions of the receive array, the coverage area is limited. To achieve high SNR in the whole volume, a receive-only array with more channels which covers a larger area can be employed.

Bibliography

- [1]. Vaughn JT, Griffiths JR. RF coils for MRI. Chichester, UK: John Wiley & Sons; 2012.
- [2]. Westbrook C, et al. MRI in Practice, 4th Edition. Wiley-Blackwell; 2011
- [3]. Jin, Jianming. Electromagnetic Analysis and Design in Magnetic Resonance Imaging. Boca Raton, FL: CRC Press LLC; 1989.
- [4]. Hayes CE, Edelstein WA, Schenck JF, Mueller OM, Eash M. An efficient, highly homogeneous radiofrequency coil for whole-body NMR imaging at 1.5 T. *J Magn Reson* 1985;63:622–628.
- [5]. Vaughan, J T, Adriany G, Garwood M, Yacoub E, Duong T, DelaBarre L, Andersen P, and Ugurbil K, Detunable transverse electromagnetic (TEM) volume coil for high-field NMR. *Magn Reson Med* 2002;47:990–1000.
- [6]. Stutzman WL, Thiele GA. Antenna theory and design, 3rd edition. New York: John Wiley & Sons; 2012.
- [7]. Muftuler LT, Gulsen G, Sezen KD, Nalcioglu O. Automatic tuned MRI RF coil for multinuclear imaging of small animals at 3T. *J Magn Reson* 2002;155:39–44.
- [8]. P_erez de Alejo R, Garrido C, Villa P, Rodriguez I, Vaquero JJ, Ruiz-Cabello J, Cortijo M. Automatic tuning and matching of a small multifrequency saddle coil at 4.7 T. *Magn Reson Med* 2004;51:869–873.
- [9]. Wang S, Dodd S, Duyn JH. Full-wave evaluations of loading factors of small animal RF receive coils. *Intl Soc Mag Reson Med* 2007;15:3246.
- [10]. Sohn SM, Gopinath A, Vaughan JT. Electrically auto-tuned RF coil design. *Intl Soc Mag Reson Med* 2011;19:3836.
- [11]. Brunner DO, De Zanche N, Frohlich J, Paska J, Pruessmann KP. Travelling-wave nuclear magnetic resonance. *Nature* 2009;457:994–998.

- [12]. Webb AG, Collins CM, Versluis MJ, Kan HE, Smith NB. MRI and localized proton spectroscopy in human leg muscle at 7 Tesla using longitudinal traveling waves. *Magn Reson Med* 2010;63:297–302.
- [13]. Andreychenko A, Bluemink JJ, Raaijmakers AJE, Lagendijk JJW, Luijten PR, and van der Berg CAT, Improved RF performance of travelling wave MR with a high permittivity dielectric lining of the bore, *Magn Reson Med*, 2013;70:885–894.
- [14]. Zhang B, Sodickson DK, Lattanzi R, Duan, Q, Stoeckel B, Wiggins GC. Whole body traveling wave magnetic resonance imaging at high field strength: homogeneity, efficiency, and energy deposition as compared with traditional excitation mechanisms. *Magn Reson Med* 2012;67:1183–1193.
- [15]. Tang JA, Wiggins GC, Sodickson DK, Jerschow A. Cutoff-free traveling wave NMR. *Concepts Magn Reson Part A Bridg Educ Res* 2011;38:253–267.
- [16]. Zhang X, Wang C, Vigneron D, Nelson S. Studies on MR Reception Efficiency and SNR of Non-resonance RF Method (NORM). In *Proceedings of the 17th Annual Meeting of ISMRM, Honolulu, Hawaii, USA, 2009*. p. 104.
- [17]. Pan Y, Zhang X. Non-resonance 16-element transceiver array for human head imaging at 7T. In *Proceedings of the 16th Annual Meeting of ISMRM, Toronto, Canada, 2008*. p. 435.
- [18]. Bruce E, Beck AC, Lowry LR. Horizontal Rhombic Antennas. In *Proceedings of the Institute of Radio Engineers, Volume 23, 1935*. p 135–158.
- [19]. Vazquez F, Martin R, Marrufo O, Rodriguez AO. Travelling wave magnetic resonance imaging at 3 T. *J Appl Phys* 2013;114:064906.
- [20]. Pozar DM. *Microwave engineering*, 2nd edition. New York: John Wiley & Sons; 1998.
- [21]. Balanis CA. *Advanced engineering electromagnetics*, 2nd edition. New York: John Wiley & Sons; 2012.
- [22]. Gedney SD. A study of the parallel-plate EMP simulator and the simulator-obstacle interaction. *USACERL Technical Report M-91/11*. Springfield, VA: US Army Corps of Engineers, Construction Engineering Research Laboratory; 1990.

- [23]. Davis WA, Agarwal K. Radio frequency circuit design. New York: John Wiley & Sons; 2001.
- [24]. Dib N, Khodier M. Design and optimization of multi-band Wilkinson power divider. *International Journal of RF and Microwave Computer-Aided Engineering* 2008;18:14–20.
- [25]. Christ A, Kainz W, Hahn EG, et al. The virtual family—development of surface-based anatomical models of two adults and two children for dosimetric simulations. *Phys Med Biol* 2010;55:N23–N38.
- [26]. Roemer PB, Edelstein WA, Hayes CE, Souza SP, Mueller OM. The NMR phased array. *Magn Reson Med* 1990;16: 192–225.
- [27]. Gabriel C. Compilation of the dielectric properties of body tissues at RF and microwave frequencies. Technical Report AL/OE-TR-1996–0037. San Antonio, TX: Brooks Air Force Base; 1996.
- [28]. Schiffman B. A new class of broadband microwave 90-degree phase shifters. *IRE Trans Microw Theory Tech* 1958;4:232–237.
- [29]. Zheng, SY, Chan WS, Man KF. Broadband phase shifter using loaded transmission line, *IEEE Microwave and Wireless Components Letters* 2010;9:498–500.
- [30]. Carter PS, inventor; Radio Corporation of America, assignee. Feedback systems for traveling wave antennas. US Patent 2,290,314. July 21, 1942.
- [31]. Yeo DTB, Wang Z, Loew W, Vogel MW, Hancu I. Local specific absorption rate in high-pass birdcage and transverse electromagnetic body coils for multiple human body models in clinical landmark positions at 3T. *J Magn Reson Imaging* 2011;33:1209–1217.
- [32]. Collins CM, Smith MB. Calculations of B1 distribution, SNR, and SAR for a surface coil adjacent to an anatomically-accurate human body model. *Mag Reson Med* 2001;45:692–699.
- [33]. Bonetto, F., Anoardo, E. and Polello, M. (2006), Saddle coils for uniform static magnetic field generation in NMR experiments. *Concepts Magn. Reson.*, 29B: 9–19.

- [34]. Ackerman, J. J. H. 2012. An Historical Introduction to Surface Coils: The Early Days. *eMagRes.* .
- [35]. J.T. Vaughan, C.J. Snyder, L.J. DelaBarre, et al. Whole-body imaging at 7 T: preliminary results. *Magn Reson Med*, 61 (1) (2009), pp. 244–248.
- [36]. C.J. Hardy, H.E. Cline, R.O. Giaquinto, T. Niendorf, A.K. Grant, D.K. Sodickson. 32-element receiver-coil array for cardiac imaging. *Magn Reson Med*, 55 (5) (2006), pp. 1142–1149.
- [37]. P.A. Bottomley, C.H.L. Olivieri, R. Giaquinto. What is the optimum phased array coil design for cardiac and torso magnetic resonance? *Magn Reson Med*, 37 (4) (1997), pp. 591–599.
- [38]. P.F. Van de Moortele, C. Akgun, G. Adriany, et al. B1 destructive interferences and spatial phase patterns at 7 T with a head transceiver array coil. *Magn Reson Med*, 54 (6) (2005), pp. 1503–1518.
- [39]. Snyder CJ, DelaBarre L, Metzger GJ et al (2009) Initial results of cardiac imaging at 7 Tesla. *Magn Reson Med* 61:517-524.
- [40]. Frauenrath, T, Hezel, F, Heinrichs, U (2009) Feasibility of cardiac gating free of interference with electro-magnetic fields at 1.5 Tesla, 3.0 Tesla and 7.0 Tesla using an MR-stethoscope. *Invest Radiol* 44: pp. 539-547.
- [41]. Elderen, SG, Versluis, MJ, Webb, AG (2009) Initial results on in vivo human coronary MR angiography at 7T. *Magn Reson Med* 62: pp. 1379-1384.
- [42]. Dieringer, MA, Renz, W, Lindel, T (2011) Design and application of a four-channel transmit/receive surface coil for functional cardiac imaging at 7T. *J Magn Reson* 33: pp. 736-741
- [43]. Gräßl A, Winter L, Thalhammer C, et al (2011) Design, evaluation and application of an eight channel transmit/receive coil array for cardiac MRI at 7.0T. *Eur J Radiol*. doi:10.1016/j.ejrad.2011.08.002
- [44]. S. Wang, H. Lu, C.J. Reddy, A Four-Element Clover Transceiver Array for 3 Tesla Cardiac MRI, *Microwave Journal*, Vol.55, No.12, Dec. 2012.
- [45]. Dieringer, M. A., Renz, W., Lindel, T., Seifert, F., Frauenrath, T., von Knobelsdorff-Brenkenhoff, F., Waiczies, H., Hoffmann, W., Rieger, J., Pfeiffer, H., Ittermann, B., Schulz-Menger, J. and Niendorf, T. (2011), Design and

- application of a four-channel transmit/receive surface coil for functional cardiac imaging at 7T. *J. Magn. Reson. Imaging*, 33: 736–741. doi: 10.1002/jmri.22451
- [46]. D. Hoult and C.N. Chen, *Biomedical Magnetic Resonance Technology*, Taylor & Francis: Oxford, UK, 1989
- [47]. Liao, Samuel Y. *Microwave Circuit Analysis and Amplifier Design*. Englewood Cliffs, NJ: Prentice-Hall, Inc: 1987.
- [48]. Gonzalez, Guillermo. *Microwave Transistor Amplifiers: Analysis and Design*. Englewood Cliffs, NJ: Prentice-Hall, Inc: 1984.
- [49]. Bowick, Chris. *RF Circuit Designs*. Howard W. Sams & Co. Inc., a publishing subsidiary of ITT.
- [50]. Reykowski, Arne. Wright, Steven M. Porter, Jay R. “Design of Matching Networks for Low Noise Preamplifiers”, *Magnetic Resonance in Medicine* 1995; 33:848-852.
- [51]. Lee R F, Giaquinto R O, Hardy C J, “Coupling and Decoupling Theory and Its Application to the MRI Phased Array”, *Magnetic Resonance in Medicine* 2002; 48:203-213.
- [52]. T. Toyooka, K. Nagayama, J. Suzuki, and T. Sugimoto, Noninvasive assessment of cardiomyopathy development with simultaneous measurement of topical H-1 and P-31 magnetic resonance spectroscopy. *Circulation* 86 (1992) 295-301.
- [53]. M.D. Schnall, V.H. Subramanian, J.S. Leigh, and B. Chance, A new double-tuned probe for concurrent H-1 and P-31 NMR. *Journal of Magnetic Resonance* 65 (1985) 122-129.
- [54]. D.I. Hoult, and B. Tomanek, Use of mutually inductive coupling in probe design. *Concepts in Magnetic Resonance* 15 (2002) 262-285.
- [55]. Robert E. Collin. *Foundation for Microwave Engineering*, 2nd Edition, Wiley-IEEE Press, 2001
- [56]. C. Monzon, A small dual-frequency transformer in two sections, *IEEE Trans Microwave Theory Tech* 51(2003), 1157–1161.
- [57]. Feng, C., G. Zhao, X. liu, and F. Zhang, "A novel dualfrequency unequal Wilkinson power divider," *Microwave and Optical Technology Letters*, Vol. 50, No. 6, 1695-1699, June 2008

- [58]. Wu, Y., Y. Liu, and S. Li, "A new dual-frequency Wilkinson power divider," *Journal of Electromagnetics Waves and Applications*, Vol. 23, 483-492, 2009.
- [59]. Dib, N. and M. Khodier, "Design and optimization of multiband Wilkinson power divider," *International Journal of RF and Microwave Computer-Aided Engineering*, Vol. 18, No. 1, 14-20, January 2008.
- [60]. Khodier, M., N. Dib, and J. Ababneh, "Design of multiband multi-section transmission line transformer using particle swarm optimization," *Electrical Engineering Journal (Archiv fur Elektrotechnik)*, Vol. 90, No. 4, 293-300, April 2008.
- [61]. Wiggins GC, Polimeni JR, Potthast A, Schmitt M, Alagappan V, Wald LL. 96-Channel receive-only head coil for 3 Tesla: design optimization and evaluation. *Magn Reson Med*. 2009; 62:754–762.
- [62]. Gareis D, Wichmann T, Lanz V, Melkus G, Horn M, Jakob PM. Mouse MRI using phased-array coils. *NMR Biomed*. 2007; 20:326–334
- [63]. Zhang X, Webb A. Design of a four-coil surface array for in vivo magnetic resonance microscopy at 600 MHz. *Concepts in Magn Reson Part B (Magn Reson Engineering)*. 2005; 24B:6–14.
- [64]. Wang, J-X.; Tian, N.; Robb, FJ.; Chen, AP.; Friesen-Waldner, L.; Rutt, BK.; McKenzie, CA. An 8-channel coil array for small animal ¹³C MR imaging. *Proceedings of the 18th Annual Meeting of ISMRM; Stockholm, Sweden*. 2010. p. 1489
- [65]. Keil B, Wiggins GC, Triantafyllou C, et al. A 20-Channel Receive-Only Mouse Array Coil for a 3T Clinical MRI System. *Magnetic resonance in medicine : official journal of the Society of Magnetic Resonance in Medicine / Society of Magnetic Resonance in Medicine*. 2011;66(2):582-593. doi:10.1002/mrm.22791.
- [66]. Kellman P, McVeigh ER. Image Reconstruction in SNR Units: A General Method for SNR Measurement. *Magnetic resonance in medicine : official journal of the Society of Magnetic Resonance in Medicine / Society of Magnetic Resonance in Medicine*. 2005;54(6):1439-1447. doi:10.1002/mrm.20713.
- [67]. Henkelman RM. Measurement of signal intensities in the presence of noise in MR images. *Med Phys* 1985;12:232–233.

- [68]. Constantinides CD, Atalar E, McVeigh ER. Signal-to-noise measurements in magnitude images from NMR phased arrays. *Magn Reson Med* 1997;38:852–857.
- [69]. Sijbers J, Den Dekker AJ, Van Audekerke J, Verhoye M, Van Dyck D. Estimation of the noise in magnitude MR images. *Magn Reson Imaging* 1998;16:87–90.
- [70]. Sonam Tobgay, “Novel Concepts for RF Surface Coils with Integrated Receivers,” MS Thesis, Worcester Polytechnic Institute, 2004
- [71]. Wright, Steven M. “ Phased Array Coils in MRS”. Department of Electrical Engineering, Texas A&M University.
- [72]. Hoult, D. I. and Bhakar, B. (1997), NMR signal reception: Virtual photons and coherent spontaneous emission. *Concepts Magn. Reson.*, 9: 277–297.
- [73]. Assessment of the sensitivity of small NMR coils with a single-loop probe, E. Durand, J. C. Ginefri, L. Darrasse, *Proc. Intl. Sot. Mag. Reson. Med.* 8 (2000),646
- [74]. Quick measurement of NMR - coil sensitivity with a dual - loop probe, Darrasse, Luc and Kassab, Ghazi, *Review of Scientific Instruments*, 64, 1841-1844 (1993).
- [75]. Lu, H, Sun, X, Salibi, N, Stoeckel, B, Denney Jr, TS, Beyers, R, Wang, S, “A Four-Channel 1H/31P Dual-Tuned Transceiver Array for 7 Tesla Cardiac Spectroscopy” International Society for Magnetic Resonance in Medicine, Salt Lake City, UT, 2013.Abstract 4308.
- [76]. Wang, S, Lu, H, Sun, X, Shao, Y, Salibi, N, Denney Jr, TS, “ 7 Tesla 1H/31P Dual-Tuned Transceiver Array for Cardiac Spectroscopy, ISMRM Workshop on Ultra High Field MRI: What is in Full Bloom & What is Sprouting?, Noordwijk aan Zee, The Netherlands, March 2013.
- [77]. Keil B, Blau JN, Biber S, et al. A 64-channel 3T array coil for accelerated brain MRI. *Magnetic resonance in medicine : official journal of the Society of Magnetic Resonance in Medicine / Society of Magnetic Resonance in Medicine.* 2013;70(1):248-258.
- [78]. Wiggins, G. C., Polimeni, J. R., Potthast, A., Schmitt, M., Alagappan, V. and Wald, L. L. (2009), 96-Channel receive-only head coil for 3 Tesla: Design optimization and evaluation. *Magn Reson Med*, 62: 754–762.

- [79]. Wang, C. and Shen, G. X. (2006), B1 field, SAR, and SNR comparisons for birdcage, TEM, and microstrip coils at 7T. *J. Magn. Reson. Imaging*, 24: 439–443.
- [80]. Avdievich NI, Hetherington HP. 4 T Actively-Detuneable Double-Tuned ¹H/³¹P Head Volume Coil and Four-Channel ³¹P Phased Array for Human Brain Spectroscopy. *Journal of magnetic resonance* (San Diego, Calif: 1997). 2007;186(2):341-346.
- [81]. Lee, R. F., Giaquinto, R., Constantinides, C., Souza, S., Weiss, R. G. and Bottomley, P. A. (2000), A broadband phased-array system for direct phosphorus and sodium metabolic MRI on a clinical scanner. *Magn Reson Med*, 43: 269–277.
- [82]. Wright, S. M. and Wald, L. L. (1997), Theory and application of array coils in MR spectroscopy. *NMR Biomed.*, 10: 394–410.
- [83]. Zhao, W., Cohen-Adad, J., Polimeni, J. R., Keil, B., Guerin, B., Setsompop, K., Serano, P., Mareyam, A., Hoecht, P. and Wald, L. L. (2014), Nineteen-channel receive array and four-channel transmit array coil for cervical spinal cord imaging at 7T. *Magn Reson Med*, 72: 291–300.
- [84]. Lu, H., Shang, S. and Wang, S. (2014), Parallel-plate waveguide for volume radio frequency transmission in MRI. *Magn Reson Med*.